

**A HETEROGENEOUS INTEGRATED PHOTONIC PLATFORM  
FOR HIGH SENSITIVITY SENSORS**

A Dissertation  
Presented to  
The Academic Faculty

by

Abeer Alsaggaf

In Partial Fulfillment  
of the Requirements for the Degree  
Doctor of Philosophy in the  
School of Electrical and Computer Engineering

Georgia Institute of Technology  
December 2025

**COPYRIGHT © 2025 BY ABEER ALSAGGAF**

**A HETEROGENEOUS INTEGRATED PHOTONIC PLATFORM  
FOR HIGH SENSITIVITY SENSORS**

Approved by:

Dr. Ali Adibi, Advisor  
School of Electrical and Computer  
Engineering  
*Georgia Institute of Technology*

Dr. Andrew Peterson  
School of Electrical and Computer  
Engineering  
*Georgia Institute of Technology*

Dr. Stephen Ralph  
School of Electrical and Computer  
Engineering  
*Georgia Institute of Technology*

Dr. Rick Trebino  
School of Physics  
*Georgia Institute of Technology*

Dr. Benjamin Klein  
School of Electrical and Computer  
Engineering  
*Kennesaw State University*

Date Approved: October 3, 2025

*To My Loved Ones*

*To Georgia Tech*

## ACKNOWLEDGMENTS

I acknowledge Professor Ali Adibi for serving as my Ph.D. advisor and for overseeing the formal requirements of my doctoral program. His supervision provided the structural framework within which this research was conducted, including administrative oversight and access to the laboratory resources necessary to complete this work.

I am also grateful to my Ph.D. committee members, Professor Ben Klein and Professor Stephen Ralph, for their guidance and feedback. It is especially meaningful to me that Professor Klein, who signed my acceptance letter to Georgia Tech back in February 2018, is now serving as a member of my Ph.D. committee in 2025. I would also like to acknowledge Professor Andrew Peterson and Professor Rick Trebino for serving on my final defense committee and for providing their time and valuable input into my work.

I would like to express my sincere appreciation to Dr. Daniela Staiculescu and Tasha Torrence for their steady support and guidance throughout my time in the ECE program. I am also truly grateful to Yvonne Coleman and Mitsuko Ito for their consistent assistance and encouragement, which contributed greatly to a positive and supportive experience.

I am especially thankful to Dr. Ashkan Zandi for his generous support and consistent guidance, particularly in the fabrication work and in advocating for me throughout this process. His help made a meaningful difference in my experience and progress. Alongside Ashkan, I had the privilege of working with Vishal Dhurgude from

the very beginning of this work, and their collaboration, discussions, and friendship have played a vital role in my journey.

I am also grateful to Abhishek Jain and Jiu Chang for their help with grating coupler simulations, Mohammad Tavakol for assistance with COMSOL simulations, and Seyed Enjaviarsanjan for his help with verifications. I would like to acknowledge Hamed Abiri and Mahmoodreza Marzban for their support and input as well.

My sincere appreciation goes to the cleanroom staff and the materials characterization facility staff at Georgia Tech for maintaining the laboratories, providing training, and offering essential technical assistance that made my experiments possible.

I also want to thank my colleagues and peers, Kirsten Masselink, Tyler Brown, Rakesh Vangapandu, Abhirupa Saha, and especially Xi Wu, whose previous work on silicon nitride chemical and biosensing devices was an important foundation that greatly benefited my own research.

Finally, I want to thank my family for their love, support, and the role they have played in my life throughout this journey. I also wish to express my heartfelt thanks to my future husband and my American family, for their love, patience, and steadfast support, which have been a source of strength and motivation throughout this journey. I would also like to thank the friends I met in Atlanta, along with the fellow Saudi students and roommates who shared this chapter of life with me; the experiences we went through together and their support made a meaningful difference in my journey.

# TABLE OF CONTENTS

<b>ACKNOWLEDGMENTS</b>	<b>iv</b>
<b>LIST OF TABLES</b>	<b>viii</b>
<b>LIST OF FIGURES</b>	<b>ix</b>
<b>LIST OF SYMBOLS AND ABBREVIATIONS</b>	<b>xii</b>
<b>SUMMARY</b>	<b>xv</b>
<b>CHAPTER 1. Introduction and Background</b>	<b>1</b>
<b>1.1 Integrated Photonic Sensors</b>	<b>1</b>
1.1.1 Label-free Sensing	2
1.1.2 Advantages of Integrated Sensor Microcavities	3
<b>1.2 Whispering Gallery Mode Microcavity-Based Integrated Sensors</b>	<b>4</b>
1.2.1 Features of WGM based Sensors	5
<b>1.3 Sensing mechanism</b>	<b>6</b>
<b>1.4 Sensitivity</b>	<b>7</b>
<b>1.5 Limit of Detection</b>	<b>9</b>
<b>1.6 Analyte Refractive Index</b>	<b>10</b>
<b>1.7 Performance Measure of Sensitivity/FWHM</b>	<b>12</b>
<b>1.8 Factors Affecting Sensitivity</b>	<b>13</b>
1.8.1 Qualify Factor	13
1.8.2 Mode Volume	15
1.8.3 Mode Overlap and Strength of field at Interaction Point	16
<b>CHAPTER 2. Design and Simulation</b>	<b>18</b>
<b>2.1 Integrated WGM Micro-Resonator Design</b>	<b>18</b>
2.1.1 Planar Disk	20
2.1.2 Vertical Slot (V-slot) Disk	22
2.1.3 Horizontal Slot (H-slot) Disk	24
2.1.4 Comparing Vertical and Horizontal Slot Designs	26
<b>2.2 Simulation of Designs Using COMSOL</b>	<b>28</b>
2.2.1 Optimized Design of H-Slot Disk at Wavelength 780 nm	28
2.2.2 Comparing TE and TM-like Polarizations of Optimized Design at 780nm	32
2.2.3 Comparing Slot and No Slot of Optimized Design at 780nm	33
2.2.4 Suspension of Optimized Design	33
2.2.5 Optimized Design of Planar Disk at Wavelength 780 nm	34
2.2.6 <i>Sensitivity Comparison Between Different Designs</i>	37
2.2.7 Optimized Design of H-Slot Disk at Wavelength 1300 nm	39
2.2.8 Asymmetrical H-Slot Disk Design at Wavelength 1300 nm	40
<b>CHAPTER 3. Nanofabrication of Device</b>	<b>42</b>
<b>3.1 Material Growth and Deposition</b>	<b>42</b>

3.1.1	Thermal Wet Oxidation	43
3.1.2	Low Pressure Chemical Vapor Deposition (LPCVD)	45
3.1.3	Atomic Layer Deposition (ALD)	48
<b>3.2</b>	<b>Metrology Tools for Fabrication Characterization</b>	<b>49</b>
3.2.1	Ellipsometer	50
3.2.2	Reflectometer	51
3.2.3	Profilometer	51
3.2.4	Scanning Electron Microscope	52
3.2.5	Optical Microscope	53
<b>3.3</b>	<b>Device Fabrication</b>	<b>54</b>
<b>3.4</b>	<b>Sample Preparation</b>	<b>56</b>
3.4.1	Wafer Cleaving	57
3.4.2	Sample Cleaning	57
<b>3.5</b>	<b>First Patterning</b>	<b>57</b>
3.5.1	Negative Resist Spin Coating	58
3.5.2	Exposure Using Electron Beam Lithography	60
3.5.3	Development	61
<b>3.6</b>	<b>Dry Anisotropic Etching</b>	<b>63</b>
3.6.1	Inductively Coupled Plasma Etching	63
3.6.2	Resist Removal	66
<b>3.7</b>	<b>Second Patterning and Alignment</b>	<b>67</b>
3.7.1	Positive Resist Spin Coating	67
3.7.2	Alignment and EBL Exposure	68
3.7.3	PMMA Development	69
<b>3.8</b>	<b>Undercutting of Horizontal Slot</b>	<b>70</b>
3.8.1	Slot Undercutting by Wet Etching With BOE	70
3.8.2	Resist Removal	70
<b>CHAPTER 4.</b>	<b>Charecterization of Device</b>	<b>73</b>
<b>4.1</b>	<b>Qualify Factor Analysis</b>	<b>73</b>
4.1.1	Qualify Factor Before Annealing	73
4.1.2	Qualify Factor After Annealing	74
4.1.3	Quality Factor with Water Cladding	75
<b>4.2</b>	<b>Bulk Chemical Sensing Results</b>	<b>77</b>
<b>4.3</b>	<b>Bio-molecular Layer Sensing Results</b>	<b>78</b>
4.3.1	Troponin Detection and Its Significance in Photonic Sensing	78
4.3.2	Surface Functionalization Procedure	79
4.3.3	Surface Sensitivity Measurement Using Troponin	82
<b>CHAPTER 5.</b>	<b>Conclusion and Future Work</b>	<b>84</b>
<b>5.1</b>	<b>Summary of Technical Contributions</b>	<b>84</b>
<b>5.2</b>	<b>Future Work</b>	<b>87</b>
<b>REFERENCES</b>		<b>89</b>

## LIST OF TABLES

Table 1	– H-Slot Design Material Properties and Dimensions.	29
Table 2	– Planar Disk Design Material Properties and Dimensions.	35
Table 3	– Fox16 spin coating around 750 nm.	59
Table 4	– Spin Coat Discharge (from Dischem).	60
Table 5	– 950 PMMA A6 Positive Resist target thickness 1000 nm.	68

## LIST OF FIGURES

Figure 1	– Silicon nitride WGM micro-disk sensor on top of a silicon oxide substrate. The analyte particles are present in the cladding area. The mode is confined in the disk and evanescent tail of the mode protrudes into the cladding.	6
Figure 2	– (A) The wavelength of the mode shifts to a new wavelength because of an analyte’s refractive index change. (B) Sensitivity (nm/RIU) is determined by finding the slope of the trendline produced by $\Delta\lambda$ vs. $\Delta n_s$ data plot.	8
Figure 3	– Refractive Index of NaCl solution at room temperature for various concentrations [48], [53].	11
Figure 4	– (A) Spectral response of a sensor with higher quality factor but the same spectral shift of 1nm. (B) Spectral response of a sensor with lower quality factor but the same spectral shift of 1nm.	12
Figure 5	– Resonance Peak of a WGM disk resonator at $\lambda_{res}$ and FWHM measurement.	14
Figure 6	– (A) Schematic showing the design of a planar disk of silicon nitride on top of a silicon oxide substrate surrounded by air cladding. (B) Mode profile of the TM-like mode at the periphery of the silicon nitride disk.	20
Figure 7	– (A) Schematic showing the design of a vertical slot disk of silicon nitride on top of a silicon oxide substrate surrounded by air cladding. (B) Mode profile of the TM-like mode at the periphery of the silicon nitride disk.	22
Figure 8	– (A) Schematic showing the design of a horizontal slot disk of silicon nitride supported by a silicon oxide slot layer, on top of a silicon oxide substrate surrounded by air cladding. (B) Mode profile of the TM-like mode at the periphery of the disk.	25
Figure 9	– (A) Intended fabrication result of a horizontal slot design. (B) Intended fabrication result of a horizontal slot design.	27
Figure 10	– Optimization of an H-slot disk design for wavelength 780nm.	29
Figure 11	– Horizontal slot micro-disk design with a thin pedestal of 30 nm.	30
Figure 12	– Simulated mode profile of horizontal slot disk at 780nm wavelength TM-like polarization.	31
Figure 13	– H-Slot Designs Using COMSOL 2D Axisymmetric Simulation.	32

Figure 14	– Design without H-Slot Using COMSOL 2D Axisymmetric Simulation.	33
Figure 15	– Suspended Design Using COMSOL 2D Axisymmetric Simulation.	34
Figure 16	– The optimization of the silicon nitride planar disk design.	35
Figure 17	– Schematic showing the design of a silicon nitride planar disk on top of a silicon oxide layer.	36
Figure 18	– Planar Disk Design Using COMSOL 2D Axisymmetric Simulation.	36
Figure 19	– Sensitivity Comparison of Different Designs.	38
Figure 20	– H-Slot Disk Design for wavelength 1300 nm.	40
Figure 21	– The difference between the symmetrical and asymmetrical designs of the H-slot Disk at wavelength 1300 nm.	41
Figure 22	– Material stack used for device fabrication: a silicon substrate with a wet thermally grown SiO <sub>2</sub> layer, followed by two LPCVD Si <sub>3</sub> N <sub>4</sub> layers separated by an ALD-deposited SiO <sub>2</sub> layer.	43
Figure 23	– Five wafers entering Tystar Tube 2 in the Marcus Cleanroom for 2.5 μm silicon oxide growth via wet thermal oxidation.	44
Figure 24	– (A) Woollam Ellipsometer results of 2.5 μm target thickness thermal wet oxidation of silicon oxide. (B) Showing a 1.458 refractive index.	45
Figure 25	– Five target wafers placed in the center of the boat, with three dummy wafers on each side, loaded into Tystar Furnace Tube 4 in the Pettit Cleanroom. Maintaining a consistent number of wafers and positions is crucial to ensure uniform silicon nitride deposition.	46
Figure 26	– (A) Woollam Ellipsometer results of 220 nm target thickness LPCVD silicon nitride. (B) Showing a 2.02 refractive index.	47
Figure 27	– (A) To prevent contamination from ALD precursors during deposition, the polished side of the wafer is positioned facing downward, while the unpolished side faces upward. Thin metallic washers are used to slightly elevate the wafer from the plate, ensuring proper placement. This method is effective because ALD thin-film deposition is conformal. (B) Side view of the wafer positioned downward and elevated by washers.	48
Figure 28	– (A) Woollam Ellipsometer results of 240 nm target thickness ALD silicon oxide. (B) Showing a 1.44 refractive index.	49
Figure 29	– Horizontal Slot Micro-disk and Waveguide Nanofabrication Process Flow.	55

Figure 30	– Material stack used for device fabrication.	56
Figure 31	– Spin coaters with the bowl lined with aluminum foil, a small chuck loaded, and the recipe set for operation.	58
Figure 32	– Optical microscope image of the device after first layer patterning.	62
Figure 33	– Plasma during dry etching using the Plasma Therm ICP in the Pettit Microelectronics Building.	64
Figure 34	– (A) Optical microscope image of the second patterning step, showing PMMA covering the sample except for a circular opening around the disk. (B) Alignment mark after being scanned by the EBL machine.	69
Figure 35	– Scanning electron microscope (SEM) images showing the waveguide and undercut disk, representing the final device features. The slot depth is 3 $\mu\text{m}$ , waveguide width is 1 $\mu\text{m}$ . No gold layer was evaporated on the sample to enhance SEM imaging, resulting in slight charging effects.	71
Figure 36	– (A) Transmission spectrum of the device before annealing in air, showing mode peaks separated by FSR of 3.8 nm. (B) Resonance peak with Lorentzian fitting for the highest quality factor before annealing in air.	74
Figure 37	– (A) Transmission spectrum of the device after annealing, showing the same FSR of 3.8 nm and higher quality factors. (B) Resonance peak with Lorentzian fitting for the highest quality factor after annealing.	75
Figure 38	– Resonance peak with Lorentzian fitting corresponding to the highest quality factor for the device measured with water cladding.	76
Figure 39	– Single azimuthal mode resonance peaks showing a redshift with increasing NaCl solution concentration.	77
Figure 40	– Water droplet on a chip following step one surface cleaning. The low contact angle ( $\sim 10^\circ$ ) provides clear evidence of successful surface hydroxylation and high hydrophilicity.	80
Figure 41	– Water droplet on a chip after the second step (APTES silanization). The increased contact angle ( $\sim 60^\circ$ ) confirms successful formation of a hydrophobic amine-functionalized surface.	81
Figure 42	– Shifts in resonance frequency due to different concentrations of Troponin.	83

## LIST OF SYMBOLS AND ABBREVIATIONS

2D	Two Dimensional
ALD	Atomic Layer Deposition
AMI	Acetone, Methanol, and Isopropanol
APTES	(3-Aminopropyl)triethoxysilane
BML	Biomolecular Layer
BOE	Buffered Oxide Etchant
BOX	Buried Oxide
CHF <sub>3</sub>	Trifluoromethane
CMOS	Complementary Metal Oxide Semiconductor
CMP	Chemical Mechanical Polishing
dB	Decibel
DI Water	Deionized Water
EBL	Electron Beam Lithography
ETA	Ethanolamine
EWFD	Electromagnetic Waves, Frequency Domain
FDE	Finite-Difference Eigenmode
FDTD	Finite-Difference Time-Domain
FOx	Flowable Oxide
FSR	Free Spectral Range
FWHM	Full Width at Half Maximum
g	Gram
H <sub>2</sub> O <sub>2</sub>	Hydrogen Peroxide
H <sub>2</sub> SO <sub>4</sub>	Sulfuric Acid
ICP	Inductively Coupled Plasma

IR	Infrared
ISFET	Ion-Sensitive Field Effect Transistor
L	Liter
LOC	Lab-on-Chip
LOD	Limit of Detection
LPCVD	Low-Pressure Chemical Vapor Deposition
mL	Milliliter
n	Refractive Index
NaCl	Sodium Chloride
nm	Nanometer
N <sub>2</sub>	Nitrogen
n <sub>eff</sub>	Effective Refractive Index
PBS	Phosphate-Buffered Saline
PMMA	Poly(methyl methacrylate)
Q	Quality Factor
Q <sub>L</sub>	Loaded Quality Factor
Q <sub>o</sub>	Intrinsic Quality Factor
Q <sub>rad</sub>	Radiation Scattering Loss
Q <sub>mat</sub>	Material Absorption
Q <sub>ss</sub>	Surface Scattering Loss
RIU	Refractive Index Unit
S	Sensitivity
Si	Silicon
SiO <sub>2</sub>	Silicon Dioxide
Si <sub>3</sub> N <sub>4</sub>	Silicon Nitride
TE	Transverse Electric

TIR	Total Internal Reflection
TM	Transverse Magnetic
TMAH	Tetramethylammonium Hydroxide
w/v	Weight per Volume
WGM	Whispering Gallery Mode
$\mu\text{g}$	Microgram
$\mu\text{m}$	Micrometer
$\Delta n_s$	Refractive Index Shift
$\Delta\lambda$	Wavelength Shift
$\eta$	Fraction of Optical Intensity in the Analyte
$\lambda$	Wavelength
$\lambda_{\text{res}}$	Resonance Wavelength
NH <sub>2</sub>	Amine Group
CHO	Aldehyde Group
UV	Ultraviolet
OH	Hydroxyl Group
cTnI	Cardiac Troponin I
PPE	Personal Protective Equipment
EDS	Energy-Dispersive X-ray Spectroscopy

## SUMMARY

Integrated photonic sensors have gained tremendous interest as compact and highly sensitive platforms for chemical and biological detection. Their compatibility with large-scale fabrication and potential for system-level integration make them ideal for applications ranging from environmental monitoring to clinical diagnostics. Despite these advantages, conventional whispering gallery mode (WGM) resonators often face fundamental trade-offs: designs that maximize sensitivity by increasing light-analyte interaction typically suffer from reduced optical quality factors, while devices optimized for high optical performance provide limited analyte access. Bridging this gap remains a key challenge in the development of practical, high-performance sensing systems.

This dissertation addresses this challenge by introducing a horizontal slot micro-disk resonator architecture that enables strong confinement of light within a nanoscale low-index region directly exposed to the analyte. Through rigorous simulations, a comprehensive nanofabrication process, and systematic characterization, the work demonstrates how this design achieves both high sensitivity and ultra-high optical quality factors. The fabrication sequence, combining multilayer deposition, high-resolution lithography, and precision etching, was optimized to produce reproducible devices with minimal scattering loss. The optical characterization confirmed excellent performance in air and in aqueous environments, validating the robustness of the slot geometry for realistic sensing conditions.

The sensing capabilities of the device were demonstrated through both bulk refractive index detection and biomolecular surface functionalization. Chemical sensing

experiments using salt solutions revealed clear, concentration-dependent resonance shifts, confirming strong bulk sensitivity and low detection limits. Biosensing studies focused on Troponin I, a key cardiac biomarker, and established that the horizontal slot design provides a high degree of evanescent field overlap with surface-adsorbed molecular layers. Together, these results establish the slot micro-disk resonator as a powerful candidate for label-free chemical and biological detection.

Beyond the experimental demonstrations, this dissertation highlights the broader implications of horizontal slot architectures for integrated photonics. Their ability to combine sensitivity, precision, and CMOS-compatible fabrication makes them well-suited for future lab-on-chip devices and point-of-care platforms. Looking forward, horizontal slot resonators have the potential to advance the development of portable, real-time, and highly reliable sensors that address pressing needs in healthcare, environmental monitoring, and beyond.

# **CHAPTER 1. INTRODUCTION AND BACKGROUND**

In the rapidly evolving landscape of technology, sensors play a pivotal role as the sensory organs of electronic systems, translating real-world physical phenomena into measurable data. These devices are integral to various applications across industries, ranging from consumer electronics to healthcare, automotive, industrial automation, and environmental monitoring. At their core, sensors are designed to capture, quantify, and convey information about the surrounding environment, enabling machines and systems to respond intelligently to changes in their surroundings. Since sensors act as conduits, bridging the gap between the analog world and digital processing units and thereby facilitating the automation and optimization of processes, it is imperative that they are highly sensitive, reliable, and robust. This is precisely what integrated photonic sensors provide.

## **1.1 Integrated Photonic Sensors**

Integrated photonic sensors offer a compelling set of advantages over other types of sensors [1]. Their ability to combine miniaturization, enhanced sensitivity, multiplexing capabilities, high-speed performance, and immunity to electromagnetic interference positions them as a promising and versatile solution in diverse fields, pushing the boundaries of what sensing technology can achieve.

In 2002, Krioukov et al. [2] documented a groundbreaking achievement with the introduction of a microcavity-based integrated sensor. This sensor module was fabricated from a silicon nitride micro-disk positioned on top of a silicon oxide base, while the

waveguide, also fabricated from silicon nitride, was situated lower in the material stack than the disk. Notably, the recorded peak quality factor reached 4,900, although this value leans towards the lower end of the spectrum. To introduce diversity in cladding materials, the researchers utilized water ( $n = 1.3330$ ) and alcohol ( $n = 1.3614$ ), resulting in a wavelength shift of 0.65 nm. Consequently, the integrated sensor demonstrated a sensitivity of approximately 23 nm/RIU, marking a commendable initiation in this research trajectory. This accomplishment has paved the way for subsequent works characterized by higher quality factors and enhanced sensitivities [3-12].

### *1.1.1 Label-free Sensing*

A desired feature of photonic integrated sensors is the capability of performing label-free sensing in which the use of additional labels, tags, or markers to detect and identify specific biological molecules or interactions is not required [13]. In traditional sensing methods, researchers often attach fluorescent or radioactive labels to the molecules of interest to make them easily detectable. However, label-free techniques eliminate the need for such tags, allowing for direct detection of the intrinsic properties of the target molecules.

In label-free biosensing, the detection is based on changes in physical or chemical properties of the molecules themselves, without the introduction of external labels that may alter the behavior of the molecules being studied [14]. This approach has several advantages, including real-time monitoring, reduced interference, and the ability to study dynamic biological interactions in a more natural environment [15].

### *1.1.2 Advantages of Integrated Sensor Microcavities*

Photonic sensors exhibit a diverse array of geometries, with some amenable to seamless integration on a chip, while others present more intricate challenges, rendering fabrication on a silicon substrate using CMOS-compatible techniques unfeasible. Sensor configurations such as micro-disks, micro-rings, and micro-racetracks can be successfully fabricated on a silicon substrate, incorporating various materials like silicon dioxide, silicon nitride, or silicon carbide. This is achieved through a meticulously executed cleanroom nanofabrication process [10-11]. The micro-sensor's geometry along with the input/output waveguide and grating designs are precisely defined on the material stack through a sequence involving resist spin coating, electron beam lithography, and the use of development chemicals. Subsequently, the pattern undergoes anisotropic etching to reveal well-defined sidewalls. In the case of advanced structures, such as horizontal slot micro-disks [16], an additional step of undercutting is necessitated through an isotropic wet etching procedure [17-18]. The inherent benefits of these integrated structures lie in their mechanical stability and unwavering reliability. The coupling region connecting the micro-cavity and the waveguide remains consistently unaltered, ensuring the preservation of the entire design geometry. Additionally, the integrated sensor module can be systematically crafted as a comprehensive lab-on-chip system, encompassing not only the micro-cavity and waveguide but also incorporating essential components like the laser source, photodetector module and other electronic components [19-20].

Contrastingly, certain structures, like micro-bubbles or micro-spheres, despite exhibiting ultra-high-quality factors surpassing those of integrated structures [21], encounter limitations in chip-based fabrication. Instead, they manifest themselves as free-

standing structures. For instance, the creation of a silica microbubble involves the precise application of heat to a segment of a silica micro-capillary, accompanied by the introduction of an air bubble through a syringe. Subsequently, a silica bubble is formed and placed in a package with a dedicated tapered fiber, enveloping the optical coupling region with a low-refractive-index polymer. However, a notable drawback lies in the fragility of this bubble and the susceptibility of the optical coupling gap to external perturbations such as air flow or mechanical vibration, potentially compromising its operational stability. Another limitation is the inability to integrate this module on a single microchip, as both the laser source and photodetector cannot be concurrently fabricated on the same chip [22].

## **1.2 Whispering Gallery Mode Microcavity-Based Integrated Sensors**

A special class of integrated photonic sensors are the ones based on a whispering gallery mode (WGM) microcavity. The term "whispering gallery modes" originated from the phenomenon observed in 1910 by Rayleigh [23] in circular or spherical structures, where sound waves traveled around the curved walls of a circular gallery with minimum loss, allowing a whisper to be heard clearly on the opposite side. In the context of optical waves and photonic microcavities, whispering gallery modes refer to the circulating optical waves that are confined within the periphery of a curved or spherical structure, such as a micro-disk or microsphere [24, 31]. These modes are solutions to the wave equation for light confined in a circular or spherical geometry. Due to the total internal reflection at the curved surface, the light waves can be trapped and circulate within the structure for many roundtrips, creating constructive interference which leads to resonance

at a specific wavelength. This resonance is highly sensitive to changes in the surrounding environment, making WGMs valuable for applications in sensing [25, 30].

The sensor functions by detecting the analyte's presence near the mode energy. When the analyte is present, it causes a change in the effective refractive index of the resonator, resulting in a shift in its resonant wavelength. The sensed information is interpreted based on the magnitude of this wavelength shift [26].

### *1.2.1 Features of WGM based Sensors*

Whispering Gallery Mode (WGM) microcavity-based optical sensors offer notable advantages over conventional photonic sensors [27]. The circular closed-loop structures, exemplified by micro-disks and micro-rings, enable a reduction in device size and footprint. This is due to the light's continuous roundtrips within the same confined volume. The smaller dimensions not only allow for the use of minimal amounts of expensive or hard-to-obtain analytes but also lead to cost reduction. Moreover, the light within the microcavity undergoes numerous roundtrips in the same mode volume, resulting in millions of interactions with the target analyte. This repeated interaction significantly boosts sensor sensitivity. In contrast to mechanical cantilever-based sensors, photonic WGM sensors exhibit excellent compatibility with aqueous analytes and environments. While excelling in sensitivity in air and vacuum, mechanical cantilevers experience damping in water, limiting their effectiveness in such conditions [13].

The Quality Factor (Q-factor) and mode volume emerge as crucial parameters during the resonator's design in sensor development, aiming to achieve optimal sensitivity. The overarching objective is to increase the Q-factor and decrease the mode

volume, fostering strong light-matter interactions within the cavity. This approach ensures the highest sensitivity in the sensor.

### 1.3 Sensing mechanism

Photonic sensors operate by detecting changes in the refractive index of the surrounding medium, which typically refers to the cladding region. These changes in the refractive index directly influence the resonant wavelength of the optical mode confined within the sensor's cavity. The resulting shift in the resonant wavelength serves as the basis for the sensing signal, providing a measurable response to changes in the environment.

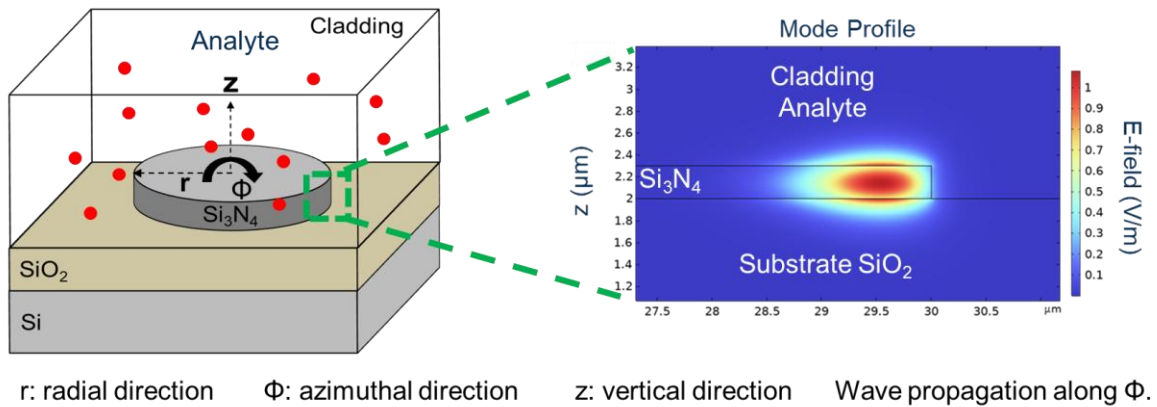


**Figure 1 – Silicon nitride WGM micro-disk sensor on top of a silicon oxide substrate. The analyte particles are present in the cladding area. The mode is confined in the disk and evanescent tail of the mode protrudes into the cladding.**

When a target analyte, such as a sodium chloride (NaCl) solution, is introduced into the region surrounding the sensor, it modifies the effective refractive index of the resonator. This alteration disrupts the resonance condition of the optical cavity, causing a shift in the resonant mode to a new wavelength. The magnitude of this wavelength shift

reflects the degree of refractive index change induced by the analyte, forming a direct link between the analyte's properties and the sensor's output.

When This mechanism allows the sensor to extract meaningful information about the analyte by precisely measuring the wavelength shift. Even minor changes in the analyte's refractive index produce detectable shifts, enabling the sensor to act as a highly sensitive and accurate tool for analyzing the surrounding medium. By converting this wavelength shift into an optical or electrical signal, the sensor provides a quantifiable output that can be used to assess the analyte's properties, such as concentration or composition. The ability to measure refractive index changes with such precision highlights the versatility and importance of photonic sensors. Consequently, they find use in diverse fields such as chemical analysis, biomedical diagnostics, and environmental monitoring, where they provide reliable and efficient solutions for detecting and analyzing target analytes with minimal disturbance to the analyte or surrounding environment.

#### 1.4 Sensitivity

The magnitude of the shift in resonance peak wavelength ( $\Delta\lambda_{res}$ ) divided by the change in refractive index of the cladding medium ( $\Delta n_s$ ) is the sensitivity of the sensor as shown in Equation 1 [49].

$$S = \frac{\Delta\lambda_{res}}{\Delta n_s} \quad (1)$$

- $S$  Sensitivity (nm/RIU).
- $\Delta\lambda_{res}$  Resonance peak shift (nm).
- $\Delta n_s$  Cladding refractive index change (RIU).

Several wavelength shifts are measured for several corresponding known changes in the analyte's refractive index. The sensitivity is determined by finding the slope of the trendline generated as shown in Figure 2(B) [49].

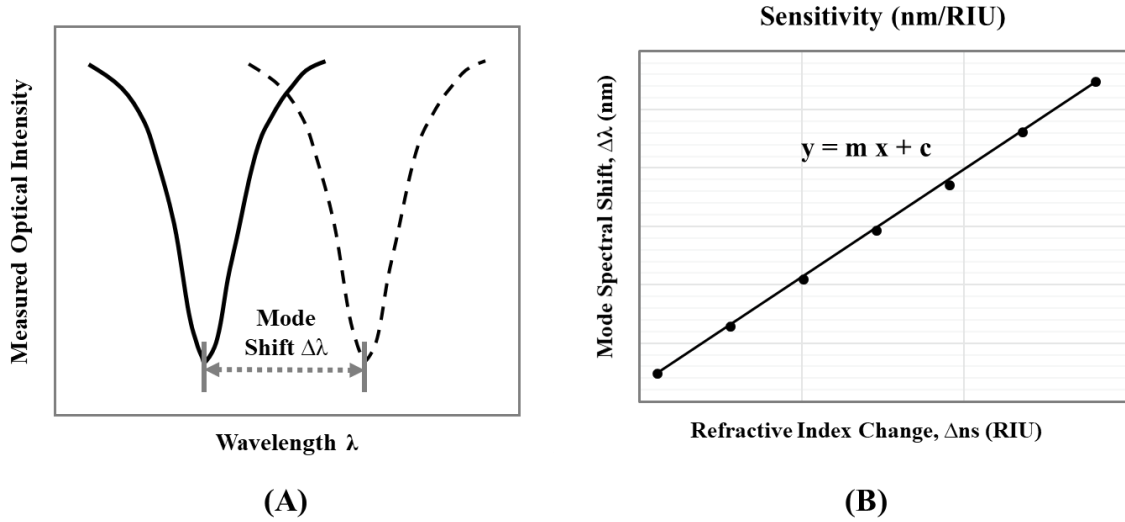


**Figure 2 – (A) The wavelength of the mode shifts to a new wavelength because of an analyte's refractive index change. (B) Sensitivity (nm/RIU) is determined by finding the slope of the trendline produced by  $\Delta\lambda$  vs.  $\Delta n_s$  data plot.**

The fraction of the optical mode interacting or probing the analyte influences the sensitivity as shown in Equation 2[49].

$$\Delta\lambda_{res} = \eta \Delta n_s \frac{\lambda_{res}}{n_{eff}} \quad (2)$$

- $\eta$  Fraction of optical intensity that probes the analyte.
- $\lambda_{res}$  Resonance wavelength (nm).
- $n_{eff}$  Effective refractive index experienced by the resonant mode.

A design that enables greater interaction or higher mode-overlap between the resonant mode and the analyte will exhibit higher sensitivity. An example of such a design is the horizontal slot micro-disk. In this design, the mode is confined within a low-refractive-index region sandwiched between two high-refractive-index regions. As a

result, the mode resides in a gap that can be filled with an analyte, allowing a large portion of the mode to interact with the target analyte, thereby significantly increasing sensitivity. This portion of the mode also constitutes the core, which possesses higher field intensity.

On the other hand, a design that allows only a small percentage of the mode to interact with the target analyte will exhibit relatively lower sensitivity. In the case of a conventional planar disk or ring resonator-based sensor design, the weak evanescent tail is the portion of the confined optical mode that overlaps with and interacts with the analyte. This tail does not possess the highest energy density. For such a design, only a small part of the mode overlaps with the analyte, while the most intense part of the mode remains confined within the inaccessible solid material of the structure. In contrast, a design such as the horizontal slot micro-disk allows a large portion of the mode to interact with the analyte.

## 1.5 Limit of Detection

The Limit of Detection (LOD) is an essential parameter for evaluating the sensitivity of optical sensors. It defines the minimum detectable amount of analyte or substance that can be reliably distinguished from the background noise or blank sample. The LOD is given by the equation:

$$LOD = \frac{3\sigma}{S} \quad (3)$$

*LOD* Limit of Detection (RIU or mM).

$\sigma$  Standard deviation of resonance wavelength (baseline noise), calculated from at least 5–10 repeated measurements (nm).

*S* Sensitivity (nm/RIU or nm/mM).

In this equation, ( $\sigma$ ) represents the standard deviation of the sensor's output when no analyte is present, which essentially quantifies the noise in the system. This noise can arise from various sources such as thermal noise, shot noise, and dark current, all of which contribute to the variability in the sensor's signal. The unit of  $\sigma$  depends on the sensor's output, typically being measured in nanometers (nm) for optical sensors that detect resonance wavelength shifts, or in unitless terms if the sensor measures a fraction of optical intensity.

The ( $S$ ) term represents the sensitivity of the sensor, previously explained in section 1.4. The sensitivity indicates how much the sensor's output will change in response to a small variation in the analyte's properties, such as refractive index or concentration. The units of sensitivity depend on the nature of the measurement: for refractive index sensors, it is typically expressed as nm/RIU (nanometers per refractive index unit), while for concentration-based sensors, sensitivity may be given as nm/M or nm/mM, indicating the change in resonance wavelength per unit concentration.

Together, the equation helps to determine the smallest detectable change in the analyte's refractive index or concentration that can be reliably identified by the sensor. The LOD thus provides a critical benchmark for assessing the performance and precision of optical sensing systems, whether they detect changes in refractive index or molecular concentration.

## **1.6 Analyte Refractive Index**

As mentioned above, the resonant wavelength shifts due to changes in the refractive index of the analyte material present in the cladding region, where the optical

mode extends. To demonstrate the operation of the designed integrated photonic sensor, aqueous solutions of sodium chloride (NaCl) are used as the analyte. The refractive index of a NaCl solution varies as a function of its concentration. Each solution concentration is expressed as a percentage weight by volume (% w/v), starting from 0% (which corresponds to deionized water with no NaCl content). For example, a 3% w/v NaCl solution in a 10 mL total volume consists of 3 g of NaCl dissolved in enough water to make 10 mL of final solution. Each concentration level has a corresponding refractive index value.

As shown in Figure 3, the refractive index increases approximately linearly with increasing NaCl concentration. These values are used to generate the sensor's sensitivity curve, as shown in Figure 2(B), by plotting resonance wavelength shift versus refractive index.

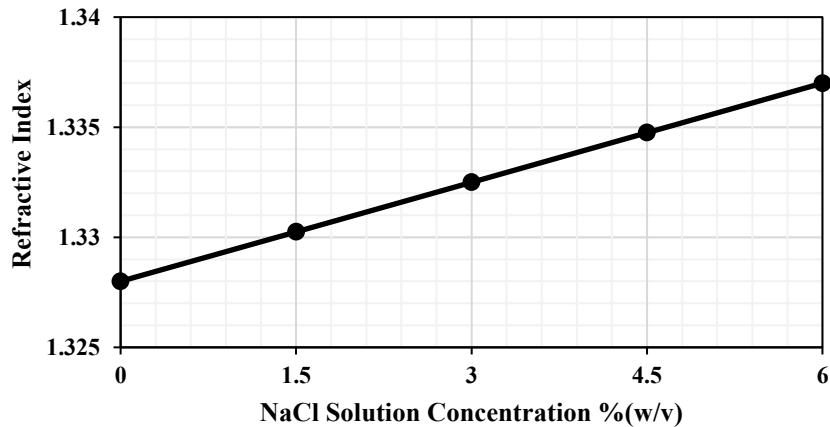


**Figure 3 – Refractive Index of NaCl solution at room temperature for various concentrations [48], [53].**

The data presented in Figure 3 were extracted from the graph published by Li et al. [48], which reports the refractive index of NaCl solutions over the wavelength range

of 300 to 2500 nm at room temperature. Additional data from reference [53] were also used.

### 1.7 Performance Measure of Sensitivity/FWHM

To provide a deeper understanding of the integrated photonic sensor's performance, Wu et al. [20] proposed a novel metric: the ratio of sensitivity to full width at half maximum (FWHM). This measure captures the sensor's detection capabilities by balancing its ability to distinguish subtle changes in input signals (sensitivity) with its spectral resolution (FWHM), offering a comprehensive and quantitative way to evaluate and compare the device's overall efficiency and precision in sensing applications.

$$\frac{S}{FWHM} \quad (4)$$

$S$  Sensitivity (nm/RIU)

$FWHM$  Full width Half Maximum (nm)

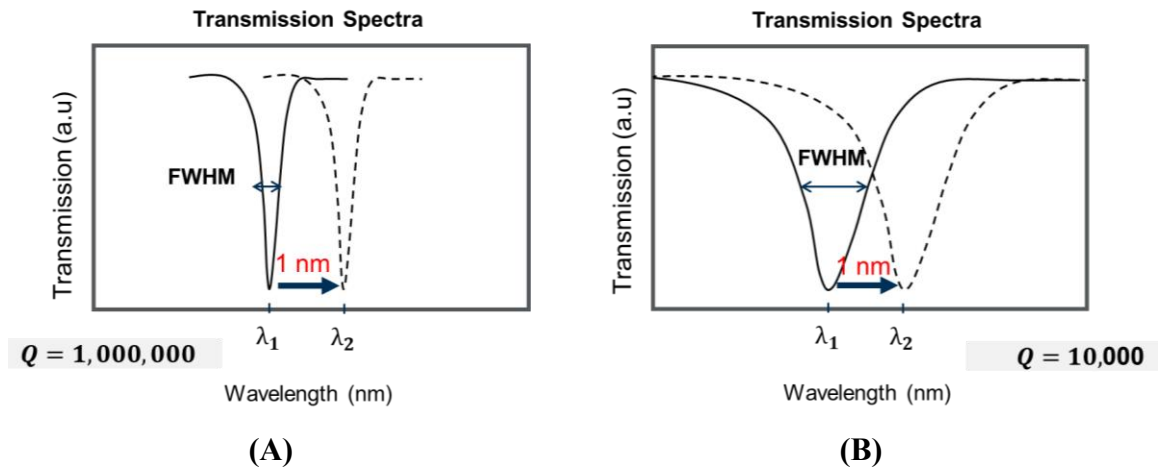


**Figure 4 – (A) Spectral response of a sensor with higher quality factor but the same spectral shift of 1nm. (B) Spectral response of a sensor with lower quality factor but the same spectral shift of 1nm.**

Figure 4, panels (A) and (B) both illustrate a spectral shift of 1 nm in response to a change in the analyte's refractive index. However, the two differ in the sharpness or width of their resonance peaks, resulting in distinct quality factors. The narrower peak corresponds to a higher quality factor, as defined in Equation 6 while the broader peak exhibits a lower quality factor.

## 1.8 Factors Affecting Sensitivity

### 1.8.1 Quality Factor

The quality factor (Q-factor) of a microcavity is a key indicator of its ability to temporally confine light. It is defined as the ratio of the stored energy to the energy lost per cycle and directly relates to the photon lifetime within the cavity. A higher Q-factor corresponds to a longer photon lifetime, allowing light to circulate within the cavity for extended periods. This prolonged confinement increases the interaction time between the optical mode and the analyte, enhancing the sensitivity of the sensor.

$$Q \propto \tau_o \quad (5)$$

$Q$  Quality Factor

$\tau_o$  Photon lifetime

In high-Q microcavities, the extended photon lifetime results in sharper resonance peaks, which improve the precision of refractive index measurements. Small changes in the analyte's properties, such as refractive index or absorption, induce detectable shifts in the resonance wavelength. The sharper the resonance, the easier it is to resolve these shifts, making high-Q cavities particularly effective for detecting subtle changes in the analyte.

$$Q_L = \frac{\lambda_{res}}{\Delta\lambda_{FWHM}} \quad (6)$$

- $Q_L$  Quality Factor  
 $\lambda_{res}$  Resonance Wavelength (nm)  
 $\Delta\lambda_{FWHM}$  Line width of the resonant mode (nm) or FWHM (nm)

However, achieving a high Q-factor is challenging due to various loss mechanisms. Scattering from surface imperfections, sidewall roughness, and contamination can significantly degrade the Q-factor by introducing unwanted energy loss. Radiative losses, bending losses due to the curvature of the cavity, and material absorption further limit the Q-factor. These losses must be minimized through careful fabrication and material selection to maintain the sensor's performance.

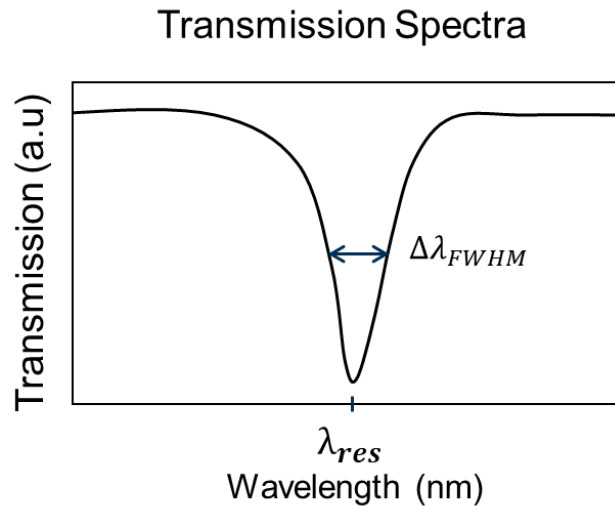


**Figure 5 – Resonance Peak of a WGM disk resonator at  $\lambda_{res}$  and FWHM measurement.**

In addition to improving sensitivity, a high Q-factor enhances the sensor's signal-to-noise ratio (SNR). With more light confined in the cavity for longer durations, the strength of the signal increases relative to the noise, allowing the detection of weaker perturbations caused by the analyte. This makes high-Q sensors particularly valuable for

applications requiring extreme precision, such as in biochemical sensing or trace gas detection.

In summary, the Q-factor plays a pivotal role in determining the sensitivity of microcavity-based sensors. A higher Q-factor enables longer photon lifetimes, sharper resonances, and increased interaction times, all of which contribute to enhanced sensitivity. However, achieving and maintaining a high Q-factor requires mitigating loss mechanisms, emphasizing the importance of high-quality fabrication and material optimization in sensor design.

### *1.8.2 Mode Volume*

Mode volume is a critical parameter in photonic cavities that characterizes the spatial confinement of the optical mode within the cavity. It plays a fundamental role in determining the energy density of the mode and, consequently, the sensitivity of photonic sensors. Mathematically, mode volume is inversely proportional to the energy density of the optical field within the cavity. A smaller mode volume results in a higher energy density, which leads to significant field enhancement at the cavity's core.

This high energy density, associated with a small mode volume, enhances the interaction between the optical mode and the analyte. When the optical field is strongly confined, even small changes in the refractive index or other properties of the analyte lead to pronounced perturbations in the optical mode. This increased interaction strength directly translates to higher sensitivity, making mode volume optimization a key design goal in photonic sensors.

The Purcell factor further quantifies the enhancement of spontaneous emission or light-matter interaction within the cavity. It is directly proportional to the Q-factor of the cavity and inversely proportional to the mode volume. Thus, a smaller mode volume not only enhances the field strength but also amplifies the Purcell factor, boosting light-matter interactions. This amplification is crucial for sensing applications, where maximizing interaction with the analyte is essential for detecting subtle changes.

In summary, reducing the mode volume enhances energy density and field strength, leading to stronger interactions between the optical mode and the analyte. Coupled with the amplification effects of the Purcell factor, this increased interaction significantly boosts sensitivity, making mode volume a pivotal factor in the design and optimization of photonic sensors.

### *1.8.3 Mode Overlap and Strength of field at Interaction Point*

The sensitivity of photonic sensors is strongly influenced by both the spatial overlap between the optical mode and the analyte region, and the field intensity within that region. As previously mentioned in Equation 2, the fraction of the mode that probes the analyte contributes directly to the resonance shift. However, the effectiveness of this interaction also depends on the strength of the optical field where the overlap occurs.

When the high-intensity core of the mode overlaps with the analyte, even small changes in refractive index can induce significant resonance shifts. In contrast, if only the weaker evanescent tail extends into the analyte region, the resulting perturbation is minimal due to the lower field strength.

Designs that place the analyte in contact with both a large fraction of the mode and its strongest field region offer enhanced sensitivity. For example, the horizontal slot micro-disk confines the mode in a low-index slot accessible to the analyte, allowing the high-intensity region of the mode to directly interact with it.

This configuration not only increases the resonance shift but also improves the signal-to-noise ratio, enabling detection of small changes in analyte properties. Such performance is particularly valuable in applications requiring high precision, such as trace-level detection or monitoring subtle concentration changes.

In summary, high sensitivity is achieved by maximizing both the mode overlap and the field intensity at the analyte interface—ensuring that the most responsive part of the optical mode contributes meaningfully to the sensing process.

## CHAPTER 2. DESIGN AND SIMULATION

This chapter presents the design of the horizontal slot disk-based sensor device, with simulations performed using COMSOL's 2D Axisymmetric Electromagnetic Waves Frequency Domain (ewfd) module to analyze the mode profiles and sensitivity of each design. The optimal horizontal slot disk design is compared to a planar disk and a vertical slot design. Additionally, an asymmetrical H-slot design is introduced.

### 2.1 Integrated WGM Micro-Resonator Design

The planar, or single-layer, disk micro-resonator represents a foundational design in photonic sensing applications due to its simplicity and ease of fabrication. However, while this design has proven effective in many contexts, its inherent limitations in sensitivity have spurred the development of more advanced structures. Among these innovations is the introduction of a slot in the resonator, which can be oriented either horizontally or vertically. This modification fundamentally changes how the optical mode interacts with the analyte and significantly enhances the performance of the device.

In the slot-resonator design, the slot serves as a direct access point for the analyte, allowing it to interact more closely with the optical mode. Unlike the planar disk, where the optical mode is confined within the material core and only the evanescent tail extends into the cladding to interact with the analyte, the slot structure enables perturbation of both the core and the evanescent tail. This direct interaction with the core—where the optical field intensity is highest—dramatically boosts the sensitivity of the device. In this configuration, the mode is primarily confined within the slot itself, while its evanescent

tails extend outward into the surrounding material. This dual interaction mechanism ensures a stronger and more localized response to changes in the refractive index of the analyte, which is critical for high-sensitivity applications.

The slot design also introduces unique optical properties that further enhance its sensing capabilities. By concentrating the optical field within the slot, the structure increases the overlap between the mode and the analyte, allowing even small perturbations to be detected with high precision. Additionally, the geometry of the slot can be tailored to specific applications, such as detecting certain biomolecules, gases, or chemicals, by optimizing the slot width, depth, and orientation. This flexibility enables the slot-resonator to address a wide range of sensing challenges with greater efficiency compared to the conventional planar disk.

In contrast, the planar design, while reliable and robust, only allows the analyte to interact with the evanescent tail of the mode. This limitation arises because the core of the mode remains confined within the solid material, leaving only the decaying field to interact with the external environment. As a result, the planar disk exhibits lower sensitivity, particularly in scenarios where detecting subtle changes in the analyte is crucial.

The slot resonator's ability to bridge the gap between the core and the external analyte represents a significant advancement in micro-resonator technology. By enhancing the interaction between the optical mode and the analyte, slot designs open new possibilities for applications requiring ultra-high sensitivity, such as biomedical diagnostics, environmental monitoring, and chemical detection. As research in this area

continues, further innovations in slot geometry and material engineering are likely to expand the utility and performance of these devices even further.

### 2.1.1 Planar Disk

The conventional planar disk design is a well-established structure in the field of integrated photonics and sensing technologies. It typically consists of a single planar layer, the disk, situated on a substrate with a cladding layer surrounding the structure. In this design, the analyte of interest—whether in liquid or gaseous form—is introduced within the cladding, allowing interaction with the optical field. Figure 6(A) illustrates the design implemented in this study, where the substrate is composed of silicon oxide, while the disk itself is fabricated from silicon nitride.

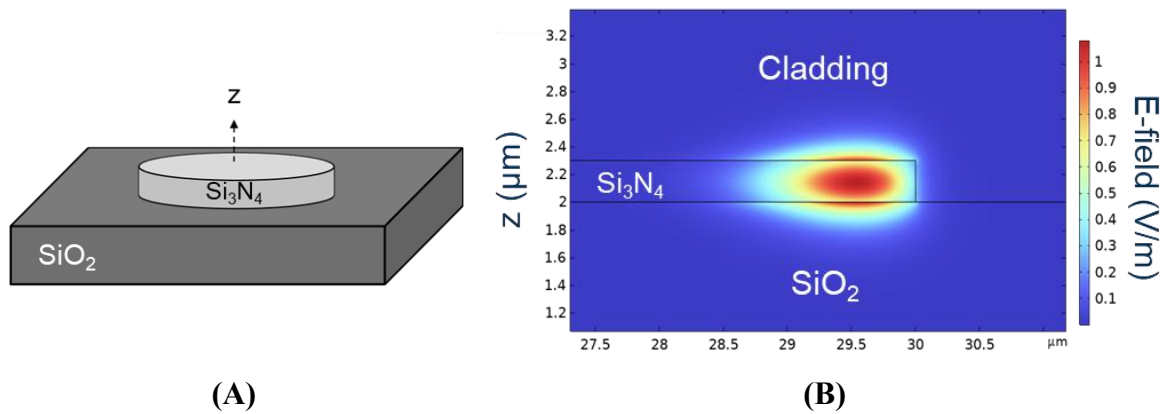


**Figure 6 – (A) Schematic showing the design of a planar disk of silicon nitride on top of a silicon oxide substrate surrounded by air cladding. (B) Mode profile of the TM-like mode at the periphery of the silicon nitride disk.**

The optical mode in this configuration is primarily confined within the silicon nitride material, which serves as the guiding medium. This confinement is critical as the highest field intensity is concentrated within the core, enabling efficient optical guidance, as depicted in Figure 6(B). However, due to the nature of the mode profile, only the

evanescent tail of the mode extends beyond the core, penetrating downward into the silicon oxide substrate and upward into the surrounding cladding layer. This characteristic makes the planar disk design inherently suited for evanescent sensing, where the interaction between the mode and the analyte occurs through the evanescent field.

While the evanescent field enables analyte detection, a limitation of this design arises from the mode's intensity distribution. The perturbation caused by the analyte takes place in the region where the field intensity has significantly decayed. As a result, the sensing performance is inherently limited by the relatively weak interaction between the analyte and the optical mode at the cladding interface. This weak interaction directly impacts the sensitivity of the sensor, as the regions of the evanescent tail do not possess the high field intensity found within the core. Consequently, while this design allows for effective sensing, its sensitivity does not reach the maximum potential achievable with alternative designs that offer stronger mode-analyte interactions.

To address these limitations, researchers have explored various strategies to enhance the mode-analyte interaction, such as modifying the geometry of the disk, introducing high-refractive-index materials in the cladding, or incorporating novel sensing modalities. These approaches aim to increase the overlap between the evanescent field and the analyte, thereby improving the overall sensitivity and performance of the sensor. Understanding and optimizing the interplay between the optical mode and the analyte remains critical in advancing the functionality and applicability of planar disk-based sensors.

### 2.1.2 Vertical Slot (V-slot) Disk

The vertical slot design offers a transformative approach to photonic sensing by directly integrating the analyte into the region of highest optical field intensity. This structure is created by etching a vertical slot into the material of a planar disk, as illustrated in Figure 7(A). The introduction of this slot redefines the mode confinement, localizing the core of the optical mode—where the field intensity is at its maximum—within the slot as shown in Figure 7(B). This ensures that the analyte, which fills the slot or resides in the surrounding cladding, interacts directly with the most intense portion of the optical field.

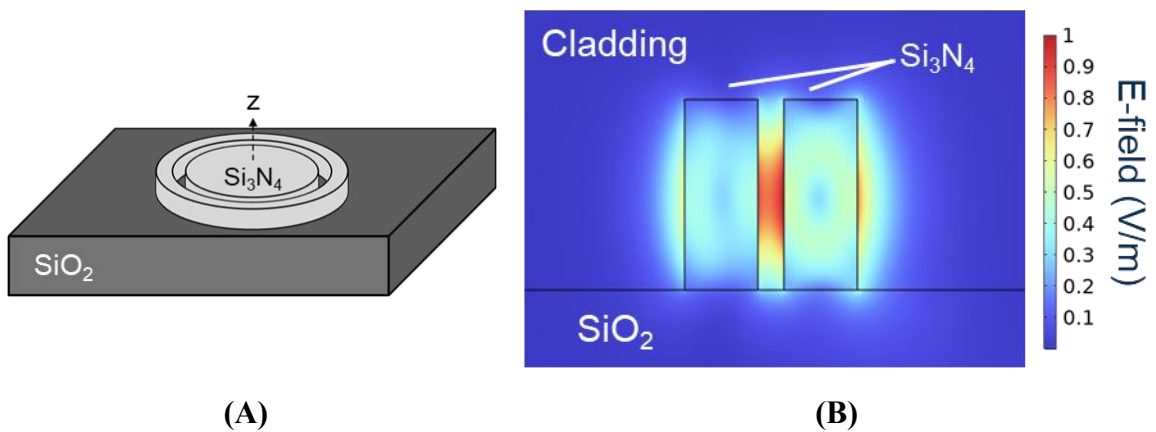


**Figure 7 – (A) Schematic showing the design of a vertical slot disk of silicon nitride on top of a silicon oxide substrate surrounded by air cladding. (B) Mode profile of the TM-like mode at the periphery of the silicon nitride disk.**

In this configuration, the slot acts as the primary interaction region, significantly enhancing the sensor's ability to detect changes in the analyte's properties. The core of the mode, confined in the slot, provides a highly sensitive detection region, as the analyte engages directly with the area of peak intensity. Meanwhile, the evanescent tail of the mode extends from the periphery of the disk into the surrounding cladding, enabling

additional interaction with the analyte outside the slot. This dual interaction mechanism—through both the core and the evanescent tail—offers comprehensive sensing capabilities, capturing subtle changes in the analyte's refractive index with high precision.

The vertical slot design's ability to combine core-level interaction with evanescent field sensing represents a significant advancement in photonic sensing technology. Traditional planar disk designs limit the analyte's interaction to the evanescent tail, which inherently has lower field intensity due to its decaying nature. In contrast, the vertical slot design increases the overlap with the mode and places the analyte directly in the region of highest optical field intensity, thereby enhancing sensor sensitivity.

Additionally, this design enables sensing in both liquid and gaseous analytes, as the slot provides an open pathway for the analyte to permeate the region of mode confinement. The evanescent tail further complements this by extending the sensing region into the cladding, making the vertical slot design versatile and highly effective in various sensing scenarios.

In summary, the vertical slot design revolutionizes photonic sensing by enabling direct interaction between the analyte and the core of the optical mode while simultaneously utilizing the evanescent tail. This dual-sensing capability allows for highly sensitive and accurate detection, offering a significant improvement over conventional planar designs and broadening the range of potential applications in high-performance sensing technologies.

### 2.1.3 *Horizontal Slot (H-slot) Disk*

Traditionally, photonic sensors have relied on the evanescent tail of the optical mode for sensing purposes [10-11]. In such designs, the core of the mode—where the field intensity is highest—remains confined within the material of the resonator, typically isolated from direct interaction with the analyte. This confinement means that the analyte interacts only with a small fraction of the optical mode's energy, specifically the evanescent part that extends outside the core. However, this portion of the mode is characterized by its lowest energy density and field intensity, as it represents the decaying region of the optical field. Consequently, the overlap between the mode and the analyte is limited, reducing the overall sensitivity of the sensor [16-18]. These inherent limitations have motivated the development of innovative solutions aimed at improving mode-analyte interaction.

One such advancement is the implementation of a horizontal slot structure, which fundamentally transforms the interaction dynamics. This design involves a micro-disk resonator with a horizontal slot, where a low refractive index region such as silicon dioxide ( $n = 1.45$ ) or even air ( $n = 1$ ) is introduced between two high refractive index materials, such as silicon nitride ( $n = 2$ ). This configuration forces the optical mode to be confined within the slot region, aligning the area of highest field intensity directly with the analyte. Unlike traditional evanescent sensing approaches, where the analyte interacts with the weakest part of the mode, the horizontal slot design allows the analyte to engage directly with the mode's core, where the energy density is at its peak. This intimate interaction leads to a significant enhancement in the sensitivity of the sensor.

The horizontal slot design leverages the unique properties of Whispering Gallery Modes (WGM), further amplifying its performance. In WGM-based horizontal slot sensors [32-33], the circular geometry of the micro-disk facilitates multiple interactions between the optical mode and the analyte as the mode circulates within the resonator. This repeated interaction within the slot region compounds the sensitivity gains, allowing even minute changes in the refractive index of the analyte to be detected with exceptional precision. This capability sets WGM-based horizontal slot sensors apart from conventional slot waveguide structures, which lack the same level of repeated mode-analyte engagement.

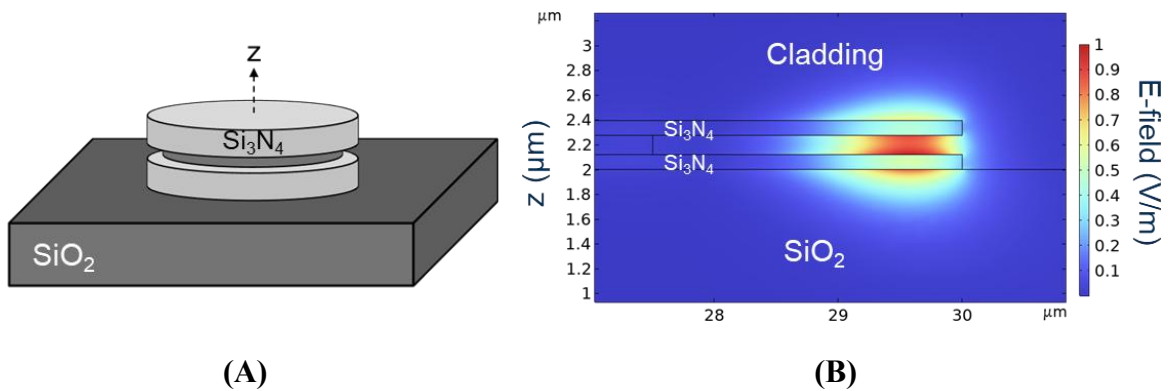


**Figure 8 – (A) Schematic showing the design of a horizontal slot disk of silicon nitride supported by a silicon oxide slot layer, on top of a silicon oxide substrate surrounded by air cladding. (B) Mode profile of the TM-like mode at the periphery of the disk.**

Additionally, the horizontal slot design introduces remarkable flexibility in terms of material and structural optimization. By carefully selecting the refractive indices of the slot and surrounding materials, as well as tailoring the dimensions of the slot, the interaction strength and spectral response can be fine-tuned for specific sensing applications. This adaptability makes horizontal slot sensors highly versatile, with

potential applications ranging from biochemical detection and environmental monitoring to industrial process control.

In summary, the horizontal slot structure represents a transformative approach to photonic sensing, addressing the limitations of traditional evanescent field sensors by enabling core-level interaction between the mode and the analyte. Through its ability to confine the optical mode within the slot and facilitate repeated interactions via WGM, this design achieves unprecedented sensitivity, paving the way for next generation sensing technologies.

#### *2.1.4 Comparing Vertical and Horizontal Slot Designs*

When comparing vertical and horizontal slot designs for the same slot dimensions (e.g.,  $2\ \mu\text{m} \times 100\ \text{nm}$ ) and a silicon nitride thickness of 180 nm, as shown in Figure 9, the differences in fabrication methods and resulting performance become evident, especially in the case of high aspect ratio slots (20:1), which are tall/narrow or deep/narrow structures often challenging to fabricate using standard etching or deposition processes.

The vertical slot design offers strong optical confinement, with the mode primarily concentrated within the etched slot. This configuration ensures robust interaction with the analyte, maximizing sensitivity through both core and evanescent tail engagement. However, the fabrication process for vertical slots presents significant challenges. Achieving the required high-aspect-ratio trench through dry etching is inherently complex and prone to imperfections. The process often introduces sidewall roughness along the boundaries of the slot, leading to substantial scattering losses. These



appealing for applications requiring consistent performance and high sensitivity. While the vertical slot design excels in optical confinement due to its geometry, the challenges associated with its fabrication and the resulting lower Q-factor often outweigh its benefits. The horizontal slot, on the other hand, provides a balanced approach, offering excellent mode confinement and analyte interaction while maintaining superior fabrication quality and a higher Q-factor. This combination of precision and performance makes the horizontal slot design a more practical and effective solution for most photonic sensing applications.

In summary, the horizontal slot design outperforms the vertical slot in terms of fabrication ease, surface smoothness, and Q-factor, making it the preferred choice for sensing devices where reliability and sensitivity are paramount. The ability to achieve precise slot dimensions and smooth interfaces with minimal scattering losses ensures that the horizontal slot design delivers exceptional performance, paving the way for advanced sensing technologies.

## **2.2 Simulation of Designs Using COMSOL**

### *2.2.1 Optimized Design of H-Slot Disk at Wavelength 780 nm*

The horizontal slot design was meticulously optimized for operation at a wavelength of 780 nm, achieving impressive performance metrics. The peak theoretical sensitivity, measured at approximately 235 nm/RIU, was obtained with a configuration featuring double nitride layers, each 120 nm thick, and a silicon oxide slot layer of 155 nm. Figure 10 illustrates the results of this optimization, highlighting the design's potential for enhanced sensing applications.

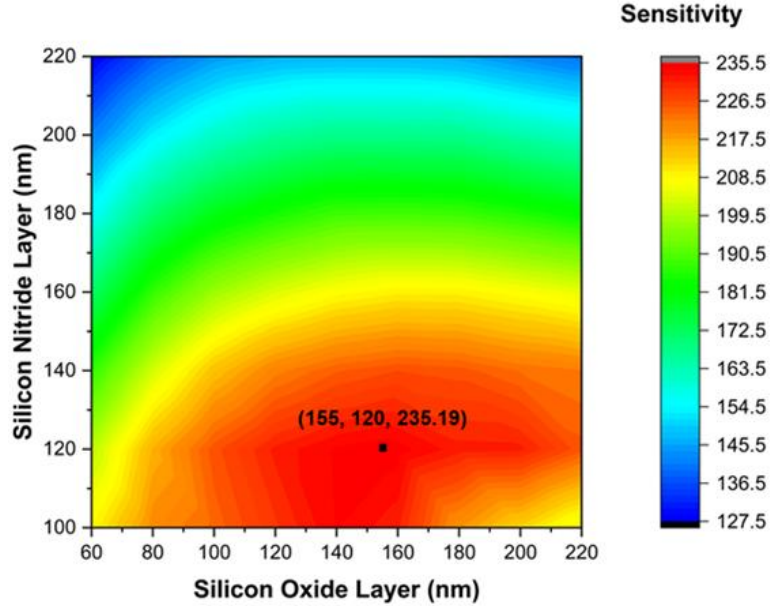


**Figure 10 – Optimization of an H-slot disk design for wavelength 780nm.**

The horizontal slot disk design is simulated in 2D Axisymmetric COMSOL Electromagnetic Waves, Frequency Domain (ewfd) interface as well. The material stack consists of two silicon nitride layers of thickness 120 nm sandwiching a layer of silicon dioxide. These three layers sit on a BOX silicon dioxide layer of thickness 2.5  $\mu\text{m}$  on a silicon substrate. The sandwiched silicon dioxide layer has a thickness of 155 nm. Also, this layer is wet etched from the periphery of the disk inwards with a depth of 2-3  $\mu\text{m}$ .

**Table 1 – H-Slot Design Material Properties and Dimensions.**

Material	Refractive Index	Thickness (nm)
Water Cladding	1.328	NA
Si <sub>3</sub> N <sub>4</sub> (upper disk)	2	120
SiO <sub>2</sub> (slot)	1.45	155
Si <sub>3</sub> N <sub>4</sub> (lower disk)	2	120
SiO <sub>2</sub> (BOX)	1.45	2500
Si (substrate)	4-inch silicon wafer	

The radius of the disk is 30  $\mu\text{m}$ , and the mode lies in the first 1  $\mu\text{m}$  from the periphery of the disk making this undercut depth suitable. Table 1 details the specification of the materials used in this design.

Figure 11 illustrates the structure of the horizontal slot disk resonator, consisting of two silicon nitride layers enclosing a silicon oxide layer. This silicon oxide layer is later undercut using wet etching to form a 2.5  $\mu\text{m}$  horizontal slot, designed to optimize the device's optical and sensing performance.

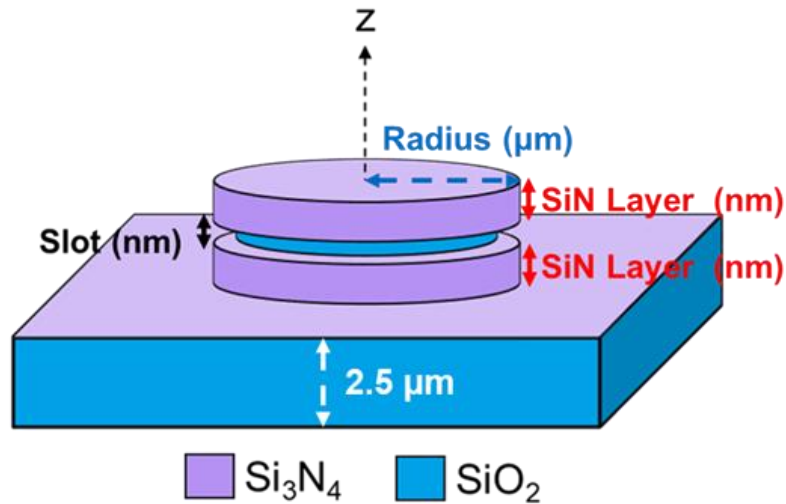


**Figure 11 – Horizontal slot micro-disk design with a thin pedestal of 30 nm.**

With this design, the liquid analyte can surround the top layer of the disk (cladding) where the evanescent tail of the mode exists as well as fill the undercut silicon dioxide layer where the core of the mode exists. The simulated micro-disk has a radius of 30  $\mu\text{m}$  and a pedestal of 30 nm from the bottom silicon nitride layer is kept for undercutting purposes as shown in Figure 12.

The horizontal slot design revolutionizes the interaction between the mode and the analyte by granting direct access to the mode's high-intensity core, which is typically

confined within the material of the disk at the periphery. Instead of relying solely on the evanescent tail of the mode protruding into the cladding—leaving the core underutilized—this design brings the core of the mode into direct contact with the analyte. The mode is now confined within the accessible slot region, which has a lower refractive index of 1.328 (liquid analyte), sandwiched between two silicon nitride layers with a refractive index of 2.

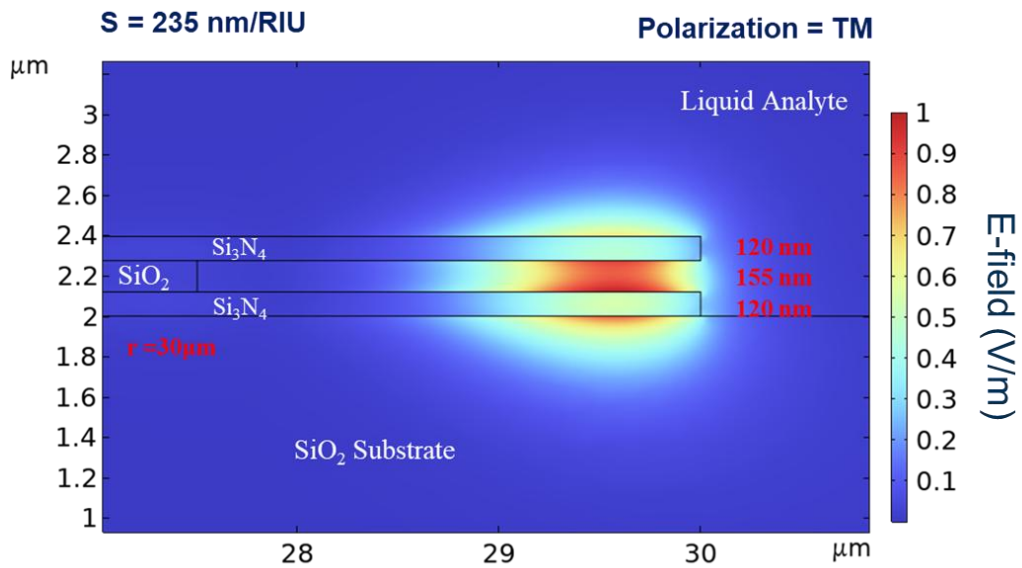


**Figure 12 – Simulated mode profile of horizontal slot disk at 780nm wavelength TM-like polarization.**

This configuration enables significant overlap and interaction between the analyte and the mode's most favorable, high-intensity part, greatly enhancing the sensor's sensitivity. Furthermore, the evanescent tail extends upward into the analyte region, creating an additional overlapping area that strengthens the interaction. As a result, the theoretical sensitivity of this design is calculated to be an impressive 235 nm/RIU, highlighting its effectiveness in optimizing sensing performance.

### 2.2.2 Comparing TE and TM-like Polarizations of Optimized Design at 780nm

The horizontal slot structure utilizes the quasi-TM mode as shown in Figure 13(A) not the quasi-TE mode shown in Figure 13(B). The reason being is that the quasi-TM mode's peak field intensity lies in the horizontal slot area and decays outwards leaving a small evanescent tail protruding to the cladding. The quasi-TE mode has the peaks of its field intensity in the lower and upper silicon nitride regions and only a part of the mode which has a medium field intensity lies in the horizontal slot where it should interact with the analyte. In this case, there is also the evanescent tail protruding to the cladding region where the analyte is present.

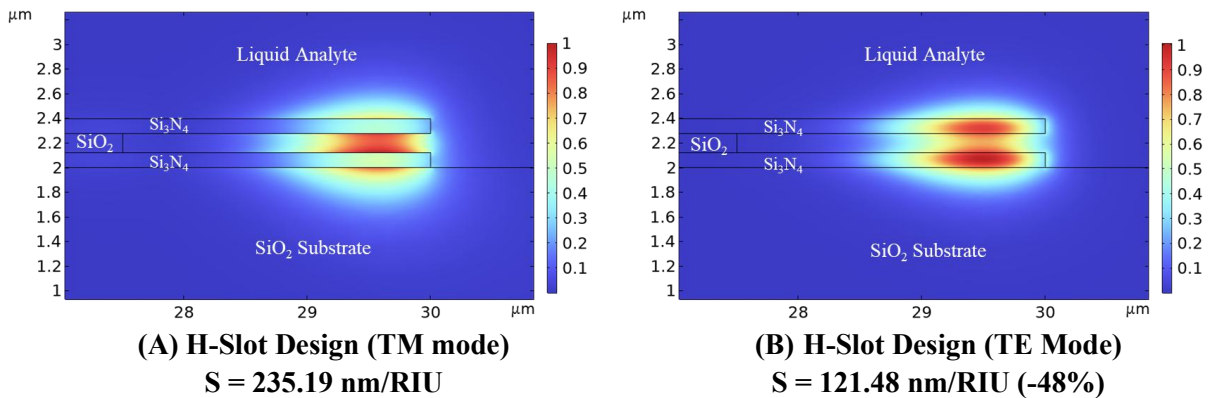


**Figure 13 – H-Slot Designs Using COMSOL 2D Axisymmetric Simulation.**

The horizontal slot design with quasi-TM mode shows the highest sensitivity among all options. It not only allows access to the interior of the mode, but it also supports some evanescent tail sensing. Considering the theoretical sensitivities calculated for the horizontal slot (undercut) disk resonator, the quasi-TM mode shows the best sensitivity of 235 nm/RIU, and the quasi-TE mode show a 48% decrease in sensitivity compared to the quasi-TM mode sensitivity.

### 2.2.3 Comparing Slot and No Slot of Optimized Design at 780nm

To show the significance of the horizontal slot sensing, the slot was removed (not wet etched) and the structure was simulated, and the theoretical sensitivity was calculated.

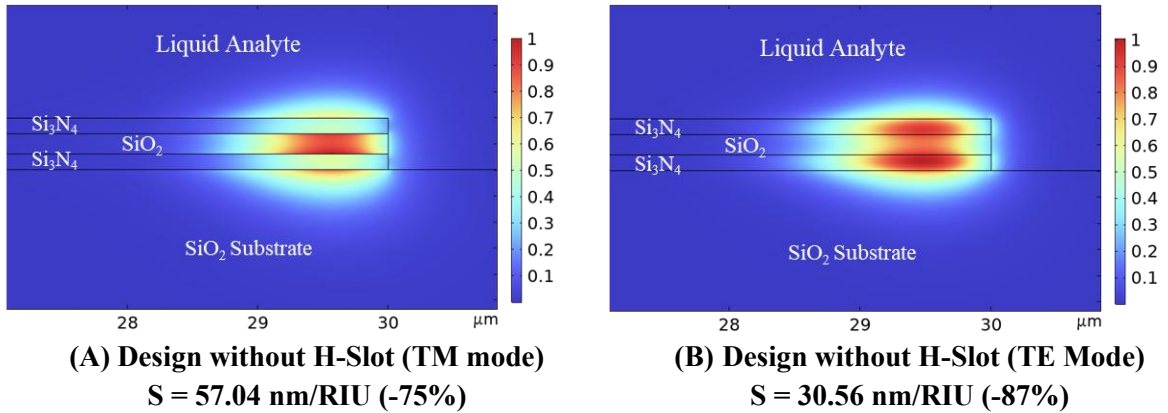


**Figure 14 – Design without H-Slot Using COMSOL 2D Axisymmetric Simulation.**

As shown in Figure 14, the mode profile shape is not affected drastically by that. But now, there is no access to the interior (core) of the mode as with the slot design. The only way the optical mode can interact with the analyte is through its evanescent tail. This decreases the sensitivity dramatically compared to the slot structure by 75%. Moreover, as we have seen with the previous design, the quasi-TE mode shows a decreased sensitivity compared to the quasi-TM mode by almost 87%.

### 2.2.4 Suspension of Optimized Design

To show the effect of suspending the H-slot structure, in the simulation, a portion of the silicon oxide under the periphery of the disk was removed as shown in Figure 15. The suspension of the structure showed that it allows the liquid analyte access to an additional part of the mode, not supported by the unsuspended structure. It allows the top

evanescent mode and the core mode in the slot as the previous design in Figure 13 showed as well as the bottom evanescent of the mode. This structure was the highest in sensitivity increasing the original optimized theoretical sensitivity to 392.78 nm/RIU which is an increase of 67%. This is because the liquid analyte now can access and interact with more parts of the confined mode. As mentioned before, all high sensitivities are obtained using the TM polarization. The TE polarization shows a reduction in the sensitivity by 28% from the optimized original design as shown in Figure 15(B).

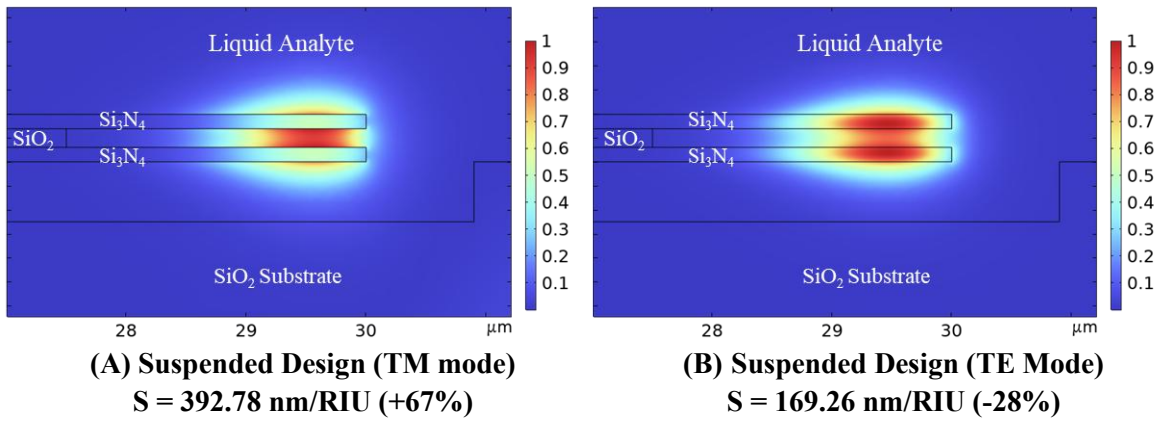


**Figure 15 – Suspended Design Using COMSOL 2D Axisymmetric Simulation.**

### 2.2.5 Optimized Design of Planar Disk at Wavelength 780 nm

The planar disk design was simulated using the 2D axisymmetric interface of COMSOL's Electromagnetic Waves, Frequency Domain (EWFD) module, which solves for time-harmonic electromagnetic field distributions. The optimization of the silicon nitride planar disk, positioned on a silicon oxide substrate, is presented in Figure 16. The highest theoretical sensitivity was determined to be approximately 136 nm/RIU, achieved with a silicon nitride layer thickness of 145 nm forming the disk.

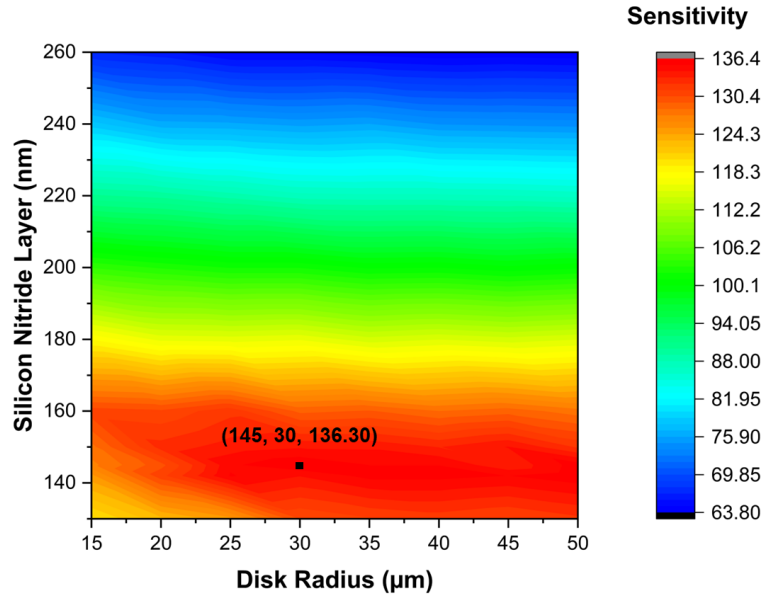


**Figure 16 – The optimization of the silicon nitride planar disk design.**

It is fabricated out of a 145 nm thick layer of silicon nitride, and it sits on a 2.5 μm silicon dioxide BOX layer on top of a silicon substrate. The cladding material is air or a liquid analyte such as water, sodium chloride solution, or a biological sample. Table 2 shows more details about the materials, refractive indices, and measurements of the design.

**Table 2 – Planar Disk Design Material Properties and Dimensions.**

Material	Refractive Index	Thickness (nm)
Water Cladding	1.328	NA
Si <sub>3</sub> N <sub>4</sub> (lower disk)	2	145
SiO <sub>2</sub> (BOX)	1.45	2500
Si (substrate)	4-inch silicon wafer	

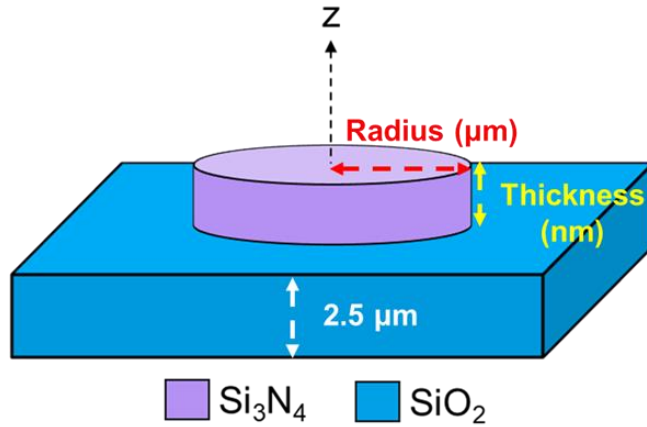


**Figure 17 – Schematic showing the design of a silicon nitride planar disk on top of a silicon oxide layer.**

The planar disk resonator design used in integrated photonic sensors stylizes the evanescent tail of the confined optical mode in material to perform the sensing mechanism. The two disadvantages of using evanescent mode sensing are: first, this part makes only a small portion of the mode, so the remaining parts of the mode are not utilized in the sensing process (less mode overlap with analyte) reducing sensor sensitivity. The second disadvantage is that this part of the mode doesn't possess the highest field amplitude (intensity), since it is the tail of the mode where it is decaying, it possesses the lowest field (amplitude) intensity.

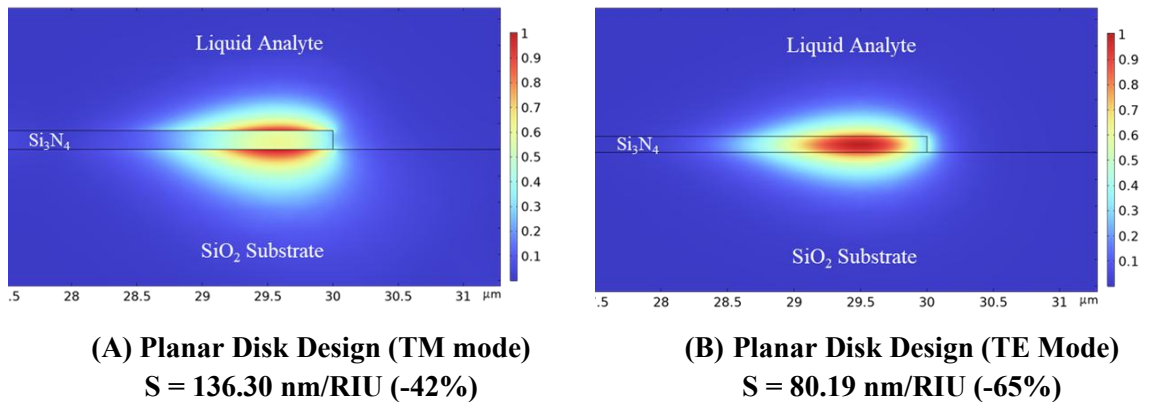


**Figure 18 – Planar Disk Design Using COMSOL 2D Axisymmetric Simulation.**

Figure 18(A) and (B) shows that the core (interior) of the optical mode is confined in the disk material, and only the evanescent tail of the mode protrudes to the top cladding where the air or analytes solution will be placed. In this case, only a small part of the mode which is not the highest in field intensity is interacting with the analyte in the cladding reducing the sensitivity of the sensor significantly.

The choice of optical mode polarization also has a significant effect on the sensitivity of the sensor. The quasi-transverse magnetic polarization (TM) shows a larger, more intense evanescent tail protruding in the surrounding region (cladding) where the analyte is placed as shown in Figure 18(A). The quasi-TE mode shows a 65% decrease in sensitivity compared to the H-Slot optimized design sensitivity, while the quasi-TM mode shows a decrease by 42%. This is a huge reduction in sensitivity making the quasi-TM mode favourable for conventional planar micro-ring based evanescent mode sensing.

#### *2.2.6 Sensitivity Comparison Between Different Designs*

As mentioned in previous subsections, high sensitivity was observed with the horizontal slot structure and the highest sensitivity is obtained by suspending the H-slot disk design. The reason for that is because the structure provided the most mode overlap with the analyte and utilized the high field interior of the mode rather than depending on the evanescent tail of the mode only. The unsuspended H-slot design utilizes this core of the mode and the top evanescent part of the mode with a sensitivity of 235 nm/RIU. The suspended version of this design adds another part of mode that can be interrogated by the analyte which is the bottom evanescent tail of the mode and that is because the material under the disk layers in the BOX material is removed via wet etching. This design produced the highest sensitivity at 392.78 nm/RIU which is a 67% increase than

the optimized H-Slot unsuspended design. It is always observed that the TE polarization of any design will reduce the sensitivity as shown in Figure 19, so the TM polarization is always preferred.

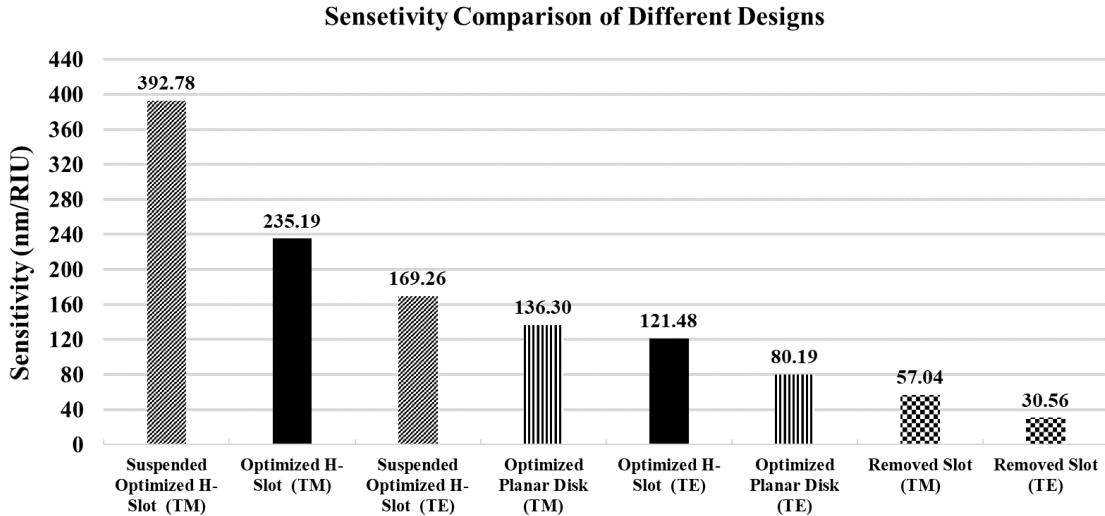


**Figure 19 – Sensitivity Comparison of Different Designs.**

Although the suspended version of the horizontal slot design provides the highest mode overlap and strongest field confinement in the analyte region, it is very challenging to fabricate when integration with input/output waveguides and grating couplers is required. To enable undercutting of the disk region and form the horizontal slot, a small pedestal of silicon nitride must be left on top of the silicon oxide BOX layer during dry etching process. This pedestal is essential for protecting the BOX oxide and allowing selective removal of the sandwiched oxide layer between the two silicon nitride layers using BOE. However, the process of wet etching under the disk in the BOX layer to suspend the structure introduces limitations when aiming for full photonic integration.

If on-chip waveguide integration is desired, the suspended version is not a practical option. The BOE undercutting process would also remove the waveguide, which is much narrower (typically 1  $\mu\text{m}$  in width) compared to the disk (e.g., 60  $\mu\text{m}$  in diameter). This makes the waveguide highly susceptible to etching damage and difficult to preserve during suspension. However, if integrated waveguides are not required and discrete optical fiber coupling is acceptable, the suspended version remains feasible. In such cases, light can be coupled into and out of the disk using tapered fibers positioned nearby. While the suspended design enables excellent optical performance, it comes with significant fabrication complexity and limited compatibility with integrated photonic platforms.

#### *2.2.7 Optimized Design of H-Slot Disk at Wavelength 1300 nm*

Increasing the operating wavelength from 780 nm to 1300 nm led to significant changes in the optical mode profile and a substantial enhancement in sensitivity. Simulations showed that the mode not only exhibited a larger evanescent tail but also a significantly expanded core, resulting in a greater interaction volume between the mode and the analyte. This increased overlap facilitated stronger interactions with the analyte, directly contributing to improved sensing performance. To accommodate the longer wavelength, the design parameters, including the thickness of the layers, were optimized, ensuring efficient mode confinement and maximum interaction with the analyte. These changes culminated in a remarkable increase in sensitivity, rising by 67% from 235 nm/RIU at 780 nm to 392 nm/RIU at 1300 nm. The results highlight the synergistic effects of the expanded mode core and enhanced evanescent field in maximizing the sensor's detection capabilities.

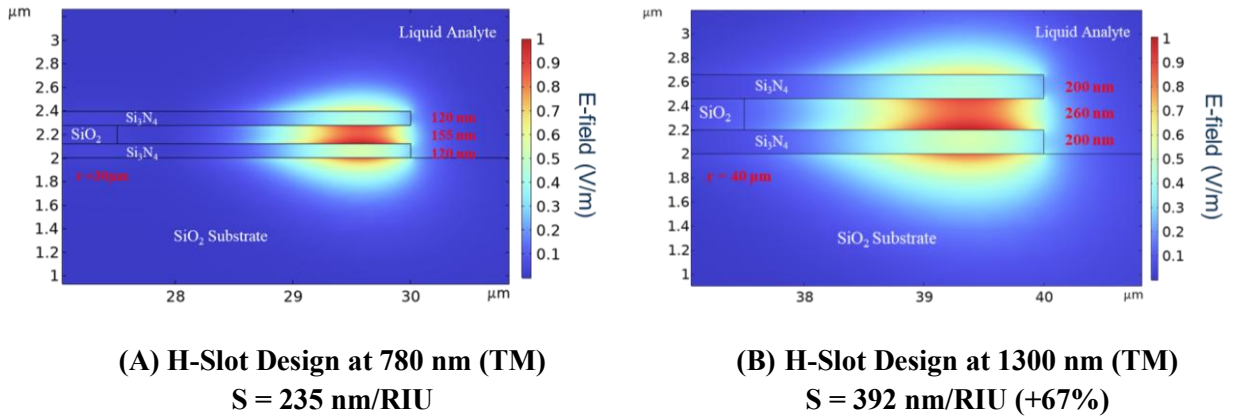


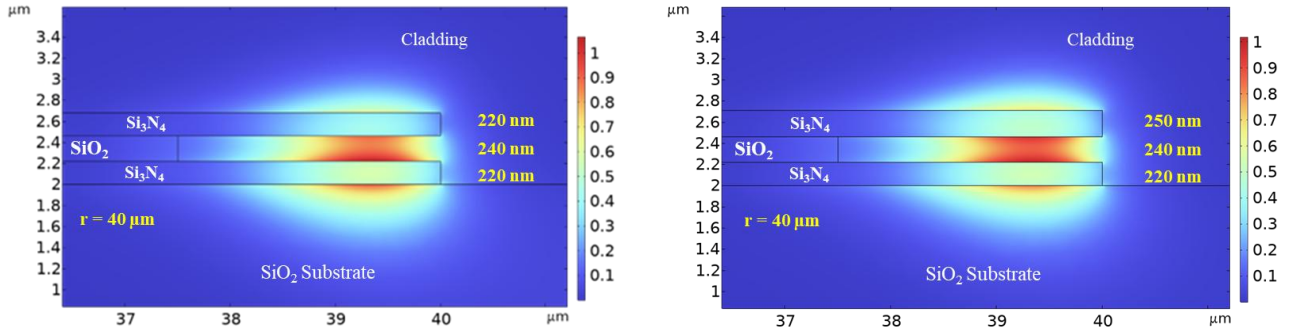
**Figure 20 – H-Slot Disk Design for wavelength 1300 nm.**

The observed increase in sensitivity at 1300 nm can be further explained by the relationship between the spectral shift  $\Delta\lambda$  and the operating wavelength  $\lambda$  as described in Equation 2. As the wavelength increases, the mode expands, leading to a larger overlap region  $\eta$  between the analyte and the optical field, further amplifying the spectral shift. This enhanced overlap, combined with the longer operating wavelength, results in a significantly larger  $\Delta\lambda$ , which translates to the observed higher sensitivity. Thus, the choice of a longer wavelength not only benefits from the proportional relationship between  $\Delta\lambda$  and  $\lambda$  but also exploits the structural adjustments that maximize  $\eta$  for improved sensing performance.

### 2.2.8 Asymmetrical H-Slot Disk Design at Wavelength 1300 nm

When the top silicon nitride layer becomes thicker than the bottom layer, as shown in Figure 21(B), the optical mode shifts upward, positioning itself closer to the center of the horizontal slot. With a fixed wavelength of 1300 nm, a disk size kept constant, a bottom silicon nitride layer thickness of 220 nm, and a slot thickness of 240 nm, increasing the top silicon nitride layer thickness from 220 nm to 250 nm drives this

upward shift. As the mode moves toward the middle of the slot, its evanescent tail extends further into the cladding region, enhancing the overlap with the analyte and increasing the interaction volume.



**(A) Symmetrical design of 220 nm for both silicon nitride layers and 240 nm for silicon oxide layer, for a cladding of 1.328 at 1300 nm wavelength. Sensitivity 383 nm/RIU**

**(B) Asymmetrical design of 220 nm for bottom silicon nitride layers and 250 for top silicon nitride layer, 240 nm for silicon oxide layer, for a cladding of 1.328 at 1300 nm wavelength. Sensitivity 400 nm/RIU**

**Figure 21 – The difference between the symmetrical and asymmetrical designs of the H-slot Disk at wavelength 1300 nm.**

This improved positioning results in a significant boost in sensitivity, as the mode's core—the region of highest field intensity—interacts more effectively with the analyte. Meanwhile, the BOX oxide layer exerts a downward pull on the mode, slightly offsetting it toward the substrate as shown in Figure 21(A). However, when the top nitride layer is sufficiently thicker than the bottom, it counterbalances the BOX oxide's influence, ensuring the mode resides centrally within the slot. This optimized configuration maximizes the mode-analyte interaction, leveraging both the expanded interaction volume and the enhanced evanescent overlap to achieve superior sensing performance.

## CHAPTER 3. NANOFABRICATION OF DEVICE

In this chapter, the fabrication process of the horizontal slot micro-disk sensor is detailed, highlighting key steps such as sample preparation, electron beam lithography (EBL) patterning, etching, and slot undercutting. The growth of the constituent layers is described with a focus on achieving material uniformity, precise thickness control, and high film quality. Metrology tools are employed throughout to characterize each step, ensuring the fabrication aligns with design specifications for reliable device performance. The fabrication processes and material characterization were performed in the Inorganic Cleanroom at the Marcus Nanotechnology Building and the Pettit Microelectronics Cleanroom on the Georgia Tech campus.

### 3.1 Material Growth and Deposition

The material stack used to fabricate the device is grown/deposited on a 4-inch (100 mm) silicon wafer supplied by WaferPro. The wafer is classified as prime grade and is P-type, doped with boron (B), with a (1-0-0) crystallographic orientation. It has a resistivity ranging from 1 to 5  $\Omega\cdot\text{cm}$  and a thickness of  $525 \pm 25 \mu\text{m}$ . The wafer features a polished, single-side surface (SSP) and includes two SEMI-standard flats for alignment. This high-quality substrate provides the necessary foundation for subsequent layer growth and precise device fabrication.

As shown in Figure 22, the material stack begins with a silicon dioxide ( $\text{SiO}_2$ ) layer, approximately  $2.5 \mu\text{m}$  thick, grown using wet thermal oxidation. This layer, referred to as the buffer oxide layer (BOX), provides isolation and mechanical support.



**Figure 22 – Material stack used for device fabrication: a silicon substrate with a wet thermally grown SiO<sub>2</sub> layer, followed by two LPCVD Si<sub>3</sub>N<sub>4</sub> layers separated by an ALD-deposited SiO<sub>2</sub> layer.**

On top of the BOX layer, are two silicon nitride (Si<sub>3</sub>N<sub>4</sub>) layers, each approximately 220 nm thick, are deposited using low-pressure chemical vapor deposition (LPCVD). Separating these nitride layers is a silicon dioxide (SiO<sub>2</sub>) layer, approximately 240 nm thick, deposited using atomic layer deposition (ALD). This carefully engineered material stack provides the necessary structure for the fabrication of the horizontal slot micro-disk sensor.

### *3.1.1 Thermal Wet Oxidation*

The BOX silicon oxide layer was grown on a four-inch silicon wafer using the Mini Tystar 4600 Tube 2 in the Marcus cleanroom. This system facilitates both dry and wet oxidation at temperatures ranging from 700–1100°C. Wet oxidation steam is generated via the pyrogenic process, combining H<sub>2</sub> and O<sub>2</sub>.

The system can process batches of up to 25 four-inch silicon wafers simultaneously, achieving oxide uniformity within 1%. For this process, the oxide layer

was grown using wet oxidation with the WETOX.002 recipe, operated at 1100°C for 13 hours and 15 minutes, targeting an oxide thickness of approximately 2.5  $\mu\text{m}$ .

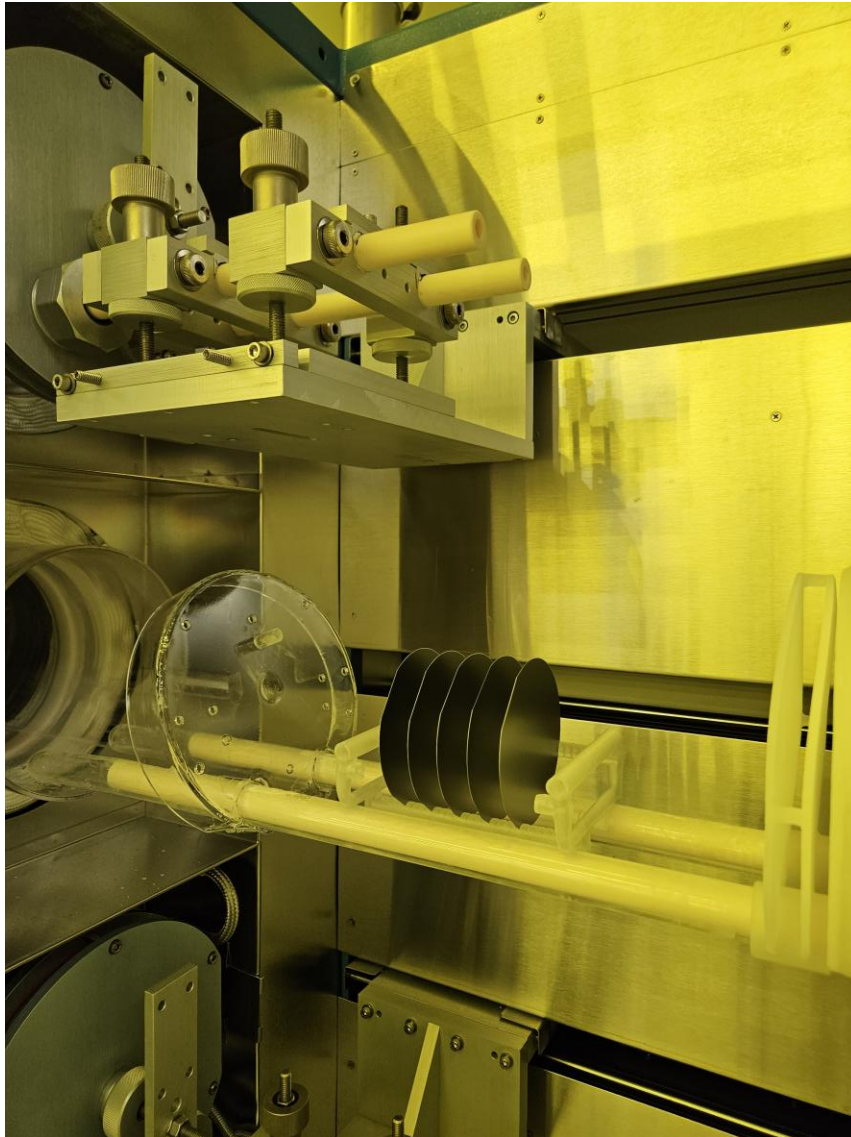


**Figure 23 – Five wafers entering Tystar Tube 2 in the Marcus Cleanroom for 2.5  $\mu\text{m}$  silicon oxide growth via wet thermal oxidation.**

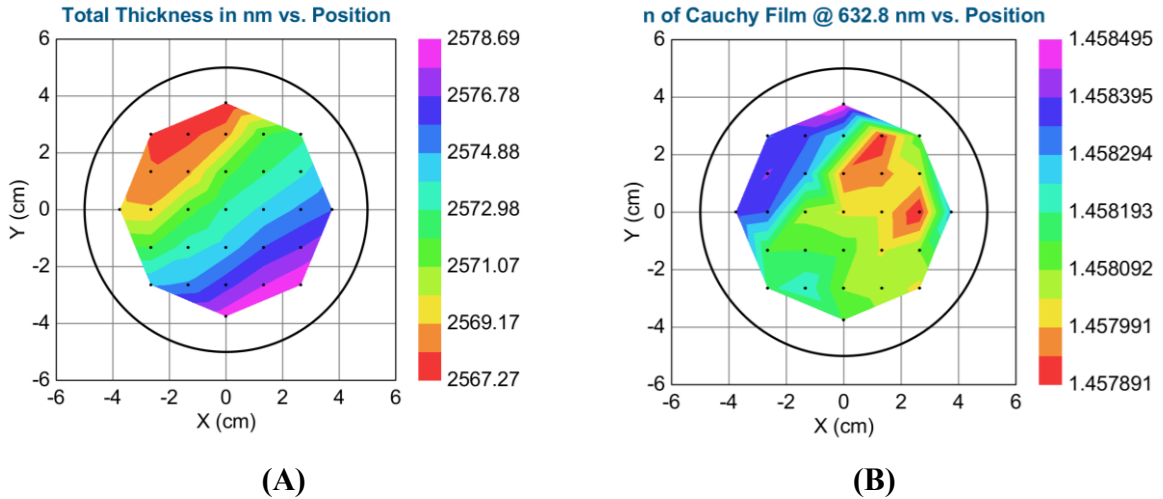


**Figure 24 – (A) Woollam Ellipsometer results of 2.5  $\mu\text{m}$  target thickness thermal wet oxidation of silicon oxide. (B) Showing a 1.458 refractive index.**

The results of this process were analyzed using the Woollam M2000 Ellipsometer. Figure 24(A) illustrates the thickness distribution across the four-inch wafer, with a measured thickness of around 2.57  $\mu\text{m}$ , which met the requirements of the process. Additionally, Figure 24(B) presents the refractive index distribution, averaging 1.458, consistent with the expected refractive index for silicon oxide grown through wet oxidation.

### 3.1.2 Low Pressure Chemical Vapor Deposition (LPCVD)

Low-pressure chemical vapor deposition (LPCVD) is a widely used method for depositing thin films, such as silicon nitride, silicon dioxide, and polysilicon, on semiconductor wafers. The process is conducted at sub-atmospheric pressures, typically ranging from 10 to 1000 millitorr, enabling excellent uniformity, high-quality films, and precise control over thickness and composition.

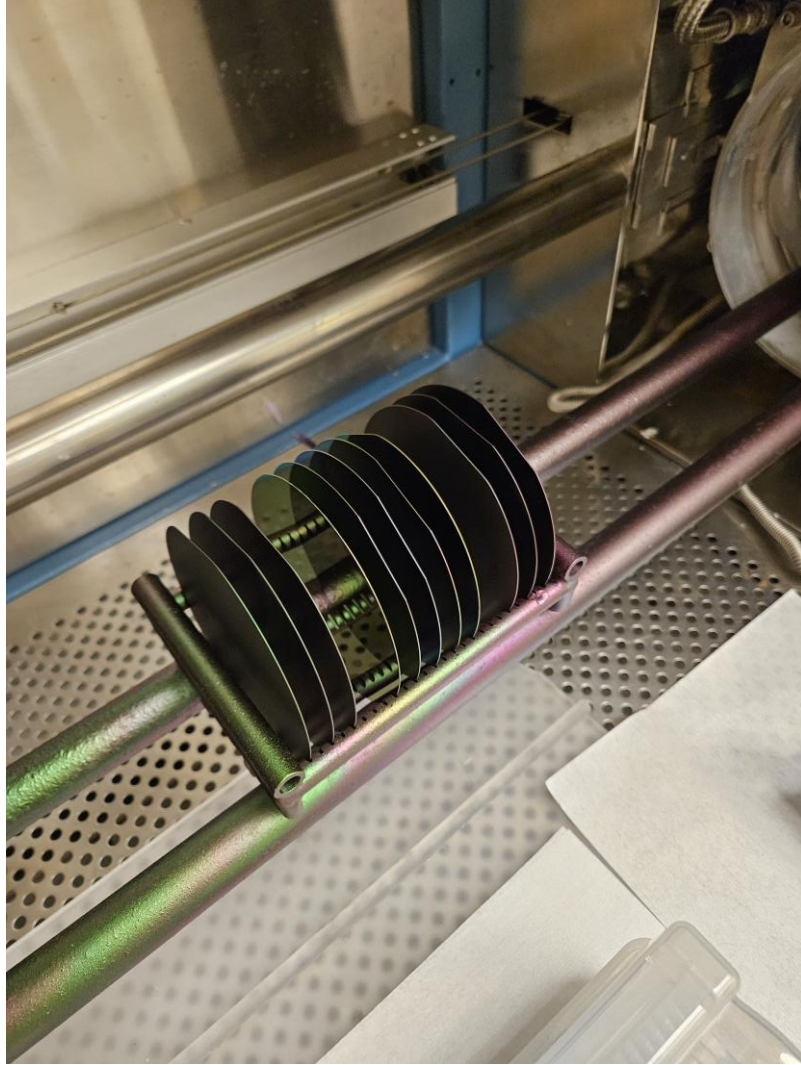


**Figure 25 – Five target wafers placed in the center of the boat, with three dummy wafers on each side, loaded into Tystar Furnace Tube 4 in the Pettit Cleanroom. Maintaining a consistent number of wafers and positions is crucial to ensure uniform silicon nitride deposition.**

The Tystar furnace in the Pettit cleanroom was used for silicon nitride depositions in this process. The LPCVD method relies on the chemical reaction of precursor gases, dichlorosilane ( $\text{SiH}_2\text{Cl}_2$ ) and ammonia ( $\text{NH}_3$ ), at elevated temperatures ranging from  $700^\circ\text{C}$  to  $900^\circ\text{C}$ , resulting in the formation of conformal silicon nitride ( $\text{Si}_3\text{N}_4$ ) films on the substrate.

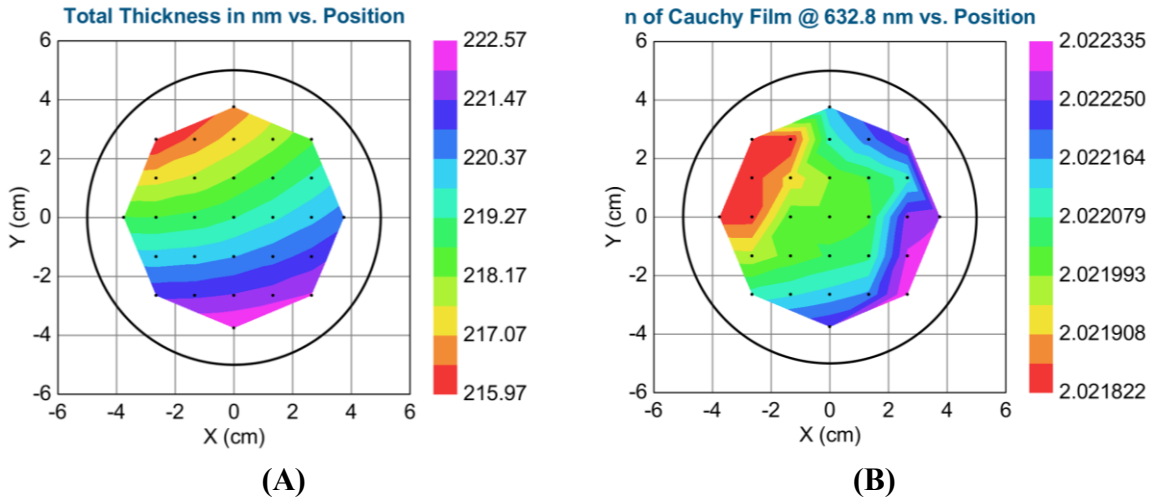


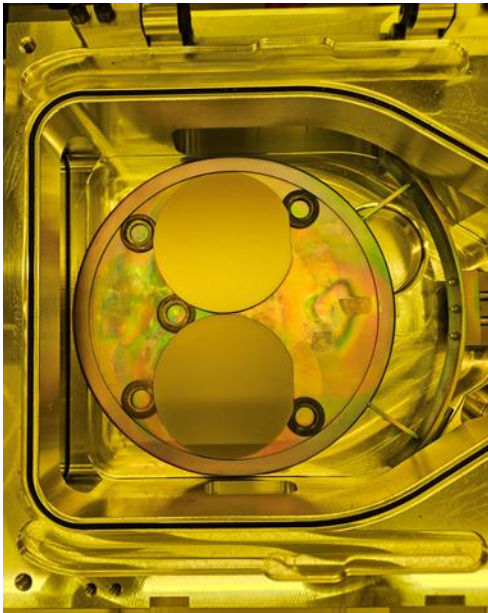
**Figure 26 – (A) Woollam Ellipsometer results of 220 nm target thickness LPCVD silicon nitride. (B) Showing a 2.02 refractive index.**

For this specific process, the target was a silicon nitride thickness of 220 nm. The deposition was carried out using the recipe Nitridev.004 with the following parameters: 770°C temperature, 88 millitorr pressure, NH<sub>3</sub> flow at 75 sccm, DCS flow at 25 sccm, and a deposition time of 98 minutes. In Figure 26, part (A) presents the thickness distribution across the four-inch wafer, while part (B) shows a typical refractive index of 2.02.

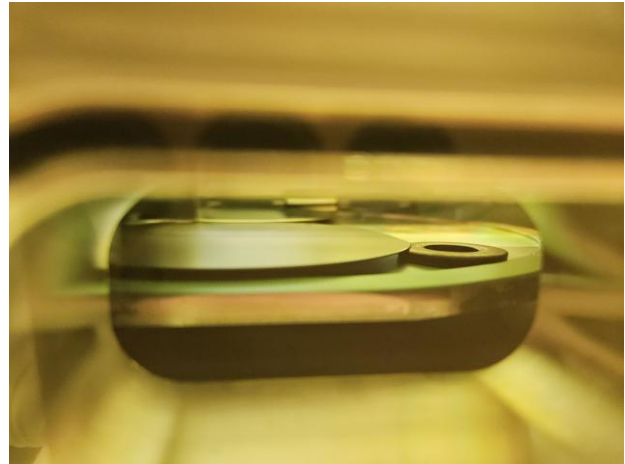
To ensure consistent results, the same number of wafers was loaded on the boat for each run. In this setup, five wafers were placed in the middle section of the boat, with three wafers loaded on each side of the 25-wafer boat. The middle wafer of the five was the primary target sample, serving as the reference for evaluating thickness and uniformity. This controlled arrangement was essential for achieving consistent and reliable deposition outcomes.

### 3.1.3 Atomic Layer Deposition (ALD)

Atomic layer deposition (ALD) is a highly precise and controllable thin-film deposition technique widely used in semiconductor manufacturing, nanotechnology, and materials research. ALD operates through sequential, self-limiting chemical reactions, where precursor gases are introduced one at a time to form a single atomic layer per cycle. This layer-by-layer approach allows for exceptional thickness control, uniformity over complex substrates, and high-quality films with minimal defects. ALD is particularly advantageous for depositing materials in applications requiring atomic-scale precision, such as gate oxides, diffusion barriers, and dielectric coatings.



(A)



(B)

**Figure 27 – (A) To prevent contamination from ALD precursors during deposition, the polished side of the wafer is positioned facing downward, while the unpolished side faces upward. Thin metallic washers are used to slightly elevate the wafer from the plate, ensuring proper placement. This method is effective because ALD thin-film deposition is conformal. (B) Side view of the wafer positioned downward and elevated by washers.**

For this process, ALD was used to deposit silicon oxide with a target thickness of 240 nm. The deposition was carried out using the Fiji F202 system located in the Marcus inorganic cleanroom. This tool utilizes advanced ALD technology to achieve highly conformal films with excellent thickness uniformity. The silicon oxide film was grown through alternating exposures of silicon-containing and oxygen-containing precursor gases, ensuring precise control of the film's composition and properties.

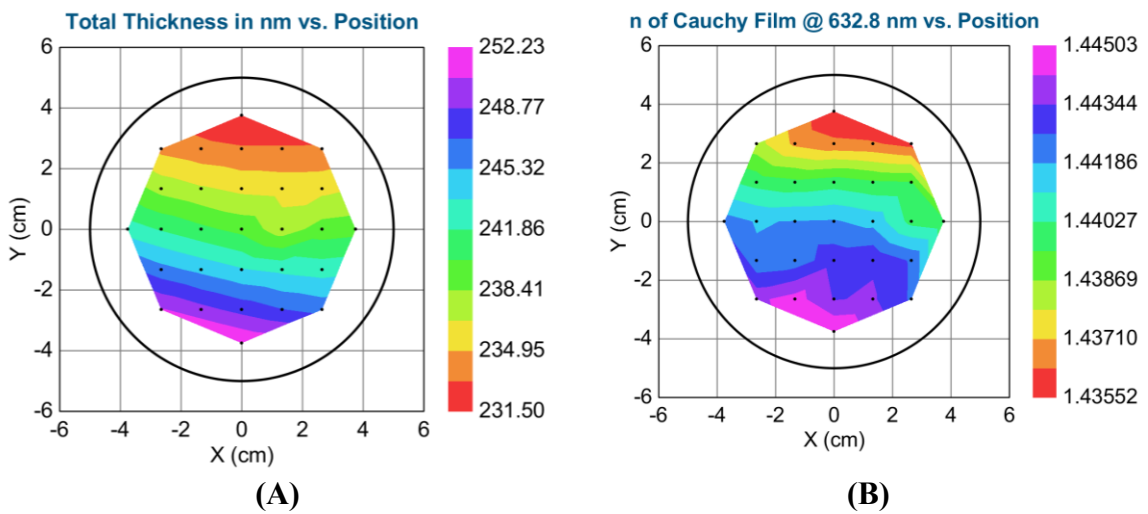


**Figure 28 – (A) Woollam Ellipsometer results of 240 nm target thickness ALD silicon oxide. (B) Showing a 1.44 refractive index.**

The Fiji F202 system, with its precise control and stable deposition environment, enabled the consistent growth of the silicon oxide layer, achieving the target thickness of 240 nm with a deviation of  $\pm 10$  nm, as shown in Figure 28(A). The resulting film exhibited a refractive index of 1.44 as shown in Figure 28(B).

### 3.2 Metrology Tools for Fabrication Characterization

In this fabrication process, various tools were essential for characterizing thin film thickness and refractive index, etch depth, resist profile and thickness, as well as device

profiles and images. These tools employed optical, mechanical, or electron-based techniques, each contributing to the precise evaluation of critical parameters. Their use was vital in ensuring the accuracy and success of subsequent fabrication steps.

### *3.2.1 Ellipsometer*

The Woollam M2000 Ellipsometer, found in the Marcus cleanroom at Georgia Tech, is an advanced spectroscopic ellipsometer designed for versatile and precise thin film characterization. It features a wide spectral range, fast data acquisition, and cutting-edge Rotating Compensator Ellipsometry (RCE) technology combined with high-speed CCD detection. This setup enables the system to collect a full spectrum of hundreds of wavelengths in just a fraction of a second, making it an exceptional tool for in-situ monitoring, process control, large-area uniformity mapping, and general-purpose thin film analysis.

In this study, the M2000 was utilized to determine the thickness and refractive index of the various layers in the material stack. Its ability to map large areas provided detailed thickness and refractive index distributions, ensuring uniformity and accuracy in the analysis. This comprehensive characterization was crucial in evaluating the integrity and consistency of the deposited films, offering critical insights into the overall performance and quality of the material stack. The combination of speed, accuracy, and versatility made the Woollam M2000 an indispensable tool for this work.

### 3.2.2 *Reflectometer*

The NanoSpec system is a non-contact film thickness measurement tool that utilizes spectroscopic reflectometry to analyze transparent and semi-transparent thin films and film stacks. By measuring the reflectance of light at various wavelengths, the NanoSpec accurately determines film thickness, making it a valuable tool for a wide range of materials and applications.

The NanoSpec 3000, available in both the Marcus and Pettit cleanrooms at Georgia Tech, is a compact, user-friendly tabletop platform designed for precise and reliable film thickness measurements. Its modern small-spot spectroscopic reflectometer enables localized thickness analysis, even on small features, while maintaining excellent accuracy and repeatability.

This system plays a crucial role in thin film characterization, providing detailed thickness data essential for process monitoring and quality assurance. By enabling quick and precise measurements, the NanoSpec ensures that thin films and film stacks meet desired specifications, ultimately supporting the accuracy and success of subsequent fabrication steps.

### 3.2.3 *Profilometer*

The KLA-Tencor P-15 Profiler, located in the Marcus cleanroom at Georgia Tech, is a highly sensitive surface measurement tool designed for characterizing surface step height and wafer stress. With the capability to measure step heights up to 327  $\mu\text{m}$

and accommodate samples up to 6 inches in size, the P-15 profiler is an essential tool for evaluating surface topography in microfabrication processes.

Using contact-based stylus profilometry, the P-15 provides precise measurements of surface features, including step heights, roughness, and stress-induced wafer curvature. This data is critical for ensuring the quality and accuracy of various fabrication steps, particularly in processes requiring high-resolution surface control.

By offering reliable and repeatable surface analysis, the KLA-Tencor P-15 profiler supports process optimization, defect identification, and overall fabrication success, making it a key asset for advanced micro- and nanofabrication workflows.

#### *3.2.4 Scanning Electron Microscope*

The Hitachi S-4700 Field Emission Scanning Electron Microscope (FE-SEM), located in the Marcus cleanroom at Georgia Tech, is a high-resolution imaging tool designed for advanced material characterization. Utilizing cold field emission technology, the S-4700 provides exceptional clarity and detail, making it ideal for analyzing thin films, semiconductor materials, and nanostructures.

The S-4700 is frequently used for capturing high-resolution images from both top-view and side-view cross-sections. This capability allows for detailed examination of surface morphology, layer thickness, and interfaces in material stacks, ensuring precise analysis of fabricated structures. In addition, the system can be paired with energy-dispersive X-ray spectroscopy (EDS) to provide elemental composition data, enabling in-depth material analysis alongside high-resolution imaging.

By combining nanoscale imaging with elemental analysis, the Hitachi S-4700 FE-SEM is an invaluable tool for ensuring the quality and consistency of materials in microfabrication and research processes. Its ability to deliver detailed visualizations and compositional insights makes it essential for optimizing thin film and semiconductor materials.

### 3.2.5 *Optical Microscope*

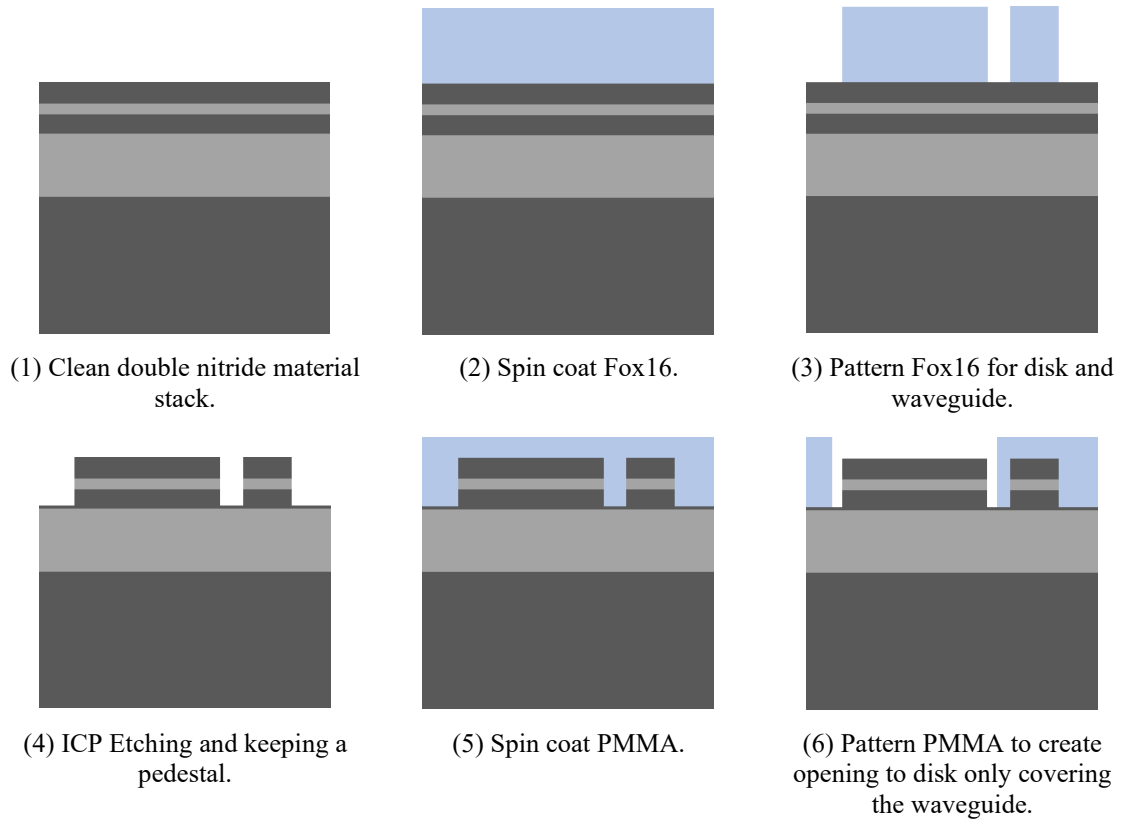
The Microscope M1 and M2 (Olympus MX61), located in the Marcus cleanroom at Georgia Tech, is a high-performance optical microscope designed for precise material inspection and analysis. With the support of the Stream Essentials imaging software, it offers advanced imaging capabilities and exceptional resolution for a variety of applications.

This microscope provides brightfield, darkfield, and optical path settings, ensuring optimal contrast and exposure for different types of substrates. It features a wide range of objective lenses, including 5x, 10x, 20x, 50x, and 100x magnifications, enabling detailed visualization at multiple scales. The stage is equipped with both coarse and fine adjustment mechanisms, allowing for precise sample positioning using a clutch handle.

Beyond imaging, the microscope supports powerful image acquisition, processing, and measurement functionalities. Its features include specialized image processing, statistical analysis, annotation tools, and report generation, making it a comprehensive tool for microfabrication and thin film characterization. With its versatility and precision, the Olympus MX61 plays a key role in ensuring the accuracy and reliability of material analysis and device inspection.

### 3.3 Device Fabrication

The first step in the fabrication process of the disk and waveguide of the sensor is the cleaning of the material stack. The cleaning is performed using Acetone, Methanol, and Isopropanol (AMI) and deionized (DI) water rinse or Piranha cleaning. The second step is patterning. The negative resist (Fox16) is spin coated with a thickness of around 750 nm as shown in Figure 29(2). Next, the Fox16 is exposed using electron beam lithography (EBL) and then developed using tetramethyl-ammonium hydroxide (TMAH) to define the disk and waveguide areas as shown in Figure 29(3). After that, the material stack undergoes an anisotropic dry etching process using ICP thermal etching. The etching process creates the disk and waveguide regions as shown in Figure 29(4).





(7) Wet etch 2 to 3  $\mu\text{m}$  of  $\text{SiO}_2$  to create the H-slot.



(8) Remove PMMA to reveal final device structure.

**Figure 29 – Horizontal Slot Micro-disk and Waveguide Nanofabrication Process Flow.**

The material stack is etched around 650 nm down to the lower silicon nitride layer leaving a thin pedestal of 30-70 nm on top of the silicon oxide BOX layer for a purpose crucial to the undercutting process. This pedestal of thin silicon nitride will protect the silicon oxide BOX layer under it from getting etched during the wet etching process of the thin sandwiched silicon oxide layer, especially the region under the waveguide. Next is the second patterning process and alignment. Positive resist polymethyl methacrylate (PMMA) is spin coated on the resultant structure as shown in Figure 29(5). The disk and waveguide regions are aligned with a second pattern that consists of circle-shaped openings to the disk area only. The waveguide region is covered. This pattern is then exposed using EBL creating the result shown in Figure 29(6). Next comes the undercutting process. The structure is wet etched in buffered oxide etchant (BOE). It is immersed in it until the sandwiched silicon oxide layer of the disk is etched 2-3  $\mu\text{m}$  inwards from the periphery of the disk as shown in Figure 29(7). Lastly, the PMMA resist is removed using acetone, rinsed, and dried to be ready for testing and characterization as shown in Figure 29(8). The subsequent parts will provide more details on the fabrication process and the recipes used to reach a successful final device.

### 3.4 Sample Preparation

The material stack used for fabricating the sensor device is illustrated in Figure 30. Above the BOX layer, the bottom silicon nitride layer is approximately 220 nm thick. The silicon oxide slot layer has a thickness ranging from 230 to 250 nm, while the top silicon nitride layer is approximately 220 nm thick. Small variations in thickness are expected due to the deposition processes of ALD and LPCVD.

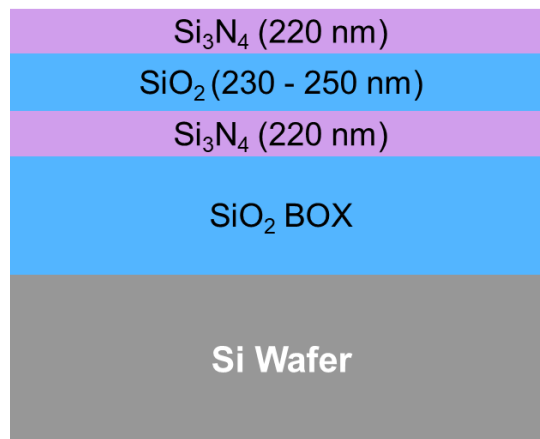


**Figure 30 – Material stack used for device fabrication.**

A grating coupler was designed to provide efficient fiber-to-chip coupling, optimized for TM polarization at a fiber tilt angle of  $-2^\circ$ . The structure incorporates a duty cycle of 0.675 and a grating pitch of 874 nm, with an etch depth of 680 nm. Maximum coupling occurs at a wavelength of 1304 nm, where the simulated efficiency reaches 14.7% (corresponding to  $-8.33$  dB). This design achieves a practical compromise between fiber-mode overlap, grating strength, and fabrication constraints, supporting robust integration into the photonic platform.

### *3.4.1 Wafer Cleaving*

The material stack is initially grown and deposited on a four-inch wafer, which must be cleaved into 2 cm by 2 cm samples to facilitate handling and compatibility with various fabrication tools. A diamond scribe is used to create a precise notch along the edge of the wafer. Gentle pressure is then applied near the scribed notch using two fingers, causing the wafer to cleave cleanly along its crystal planes due to its brittle nature.

### *3.4.2 Sample Cleaning*

The standard cleaning process typically involves several rounds of AMI acetone, methanol, and isopropanol cleaning, followed by a DI water rinse, blow-drying with a nitrogen gun, and a dehydration bake at 100°C for a few minutes to eliminate residual moisture and contamination. For samples requiring deeper cleaning, a piranha solution composed of three parts sulfuric acid and one part hydrogen peroxide heated to 140°C is used to remove more stubborn contaminants. After piranha cleaning, the samples are rinsed thoroughly with DI water, dried using a nitrogen gun, and subjected to a final dehydration bake at 100°C to ensure cleanliness.

## **3.5 First Patterning**

Patterning is the process of transferring a design pattern onto a material, which is a critical step in nanofabrication. This process typically begins with spin coating, where a thin layer of photoresist or electron-beam resist is uniformly applied to the surface of the sample using a high-speed spinning motion. The coated sample is then exposed to a

lithography process, such as photolithography or electron-beam lithography, depending on the required resolution. During this step, the resist is selectively exposed to light or an electron beam through a photomask or direct-write technique, respectively, to define the desired pattern. Finally, the exposed sample undergoes development in an appropriate chemical developer, which removes either the exposed or unexposed resist (depending on whether positive or negative resist is used), revealing the underlying material in the patterned regions.

### 3.5.1 Negative Resist Spin Coating

The resist used in the first patterning step is FOX-16, a hydrogen silsesquioxane (HSQ)-based negative-tone electron beam resist provided by DisChem. Negative-tone resists like FOX-16 harden upon exposure to electron beam lithography, making the exposed areas insoluble during development.

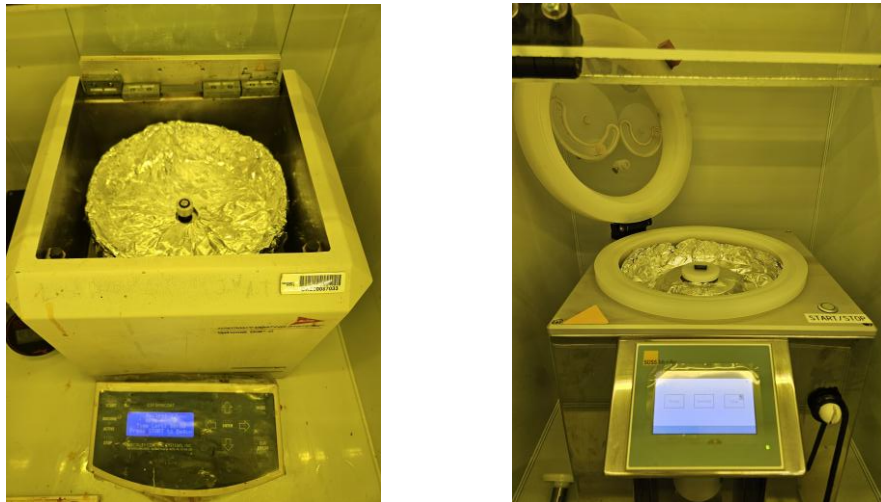


**Figure 31 – Spin coaters with the bowl lined with aluminum foil, a small chuck loaded, and the recipe set for operation.**

FOX-16 is highly valued for its high resolution, excellent etch resistance, and suitability for nanoscale patterning, making it ideal for applications requiring precise pattern transfer. In this process, FOX-16 is used to define the disk, waveguide, and grating areas of the sensor device. A uniform layer of FOX-16 with a thickness of approximately 750 nm is applied to protect these areas during the etching process, while unprotected regions will be etched down by 650 nm to achieve the desired structure.

FOX-16 is stored in a refrigerator to maintain its stability and must be allowed to reach room temperature before application to ensure proper consistency and uniform coating. A clean pipette is used to carefully transfer the resist onto the sample to avoid contamination. The spin-coating process is carried out using the Spin Coating Systems SUSS Microtech Labspin 8 located in the Marcus cleanroom. The specific spin-coating recipe, outlined in Table 3, ensures the formation of a uniform resist layer. After spin coating, the sample is baked on a hotplate at 100°C for 5 minutes.

**Table 3 – Fox16 spin coating around 750 nm.**

Step	Time	Speed	Acceleration
1	10	500	250
2	30	3000	833

After applying FOX-16, a chemical called (discharge) is spin-coated onto the sample to prevent charge buildup during electron beam exposure, which could otherwise introduce artifacts in the pattern. The recipe for applying the discharge layer is detailed in Table 4, and no baking is required after this step. This additional layer ensures a reliable and precise lithographic pattern transfer.

**Table 4 – Spin Coat Discharge (from Dischem).**

Step	Time	Speed	Acceleration
1	5	500	250
2	30	3000	250

To confirm that the FOX-16 layer achieves the target thickness of 750 nm, a bare silicon sample can be spin-coated and baked under the same conditions. The thickness of the resist layer is measured using an ellipsometer, such as the Woollam Ellipsometer, or the Nanospec to verify uniformity and consistency. This verification step ensures the reliability of the resist layer, which is crucial for the success of subsequent fabrication processes.

### 3.5.2 Exposure Using Electron Beam Lithography

The fabrication process utilizes electron beam lithography (EBL), a high-resolution patterning technique essential for creating nanoscale features. Unlike photolithography, which relies on masks to transfer patterns using UV light, EBL employs a focused electron beam to directly write patterns onto an electron-sensitive resist. This eliminates the need for physical masks, offering unparalleled flexibility in designing and modifying patterns. Additionally, EBL achieves much higher resolution than photolithography, making it ideal for applications requiring feature sizes below 100 nm, such as in the fabrication of disk, waveguide, and grating structures in sensor devices. While EBL offers precision and adaptability, its primary trade-offs include longer processing times and higher operational costs compared to mask-based lithography.

For this process, the Elionix EBL system in the Marcus cleanroom is used to expose the resist. The system is operated with a beam current of 1 nA and area doses ranging from 2500 to 2700  $\mu\text{C}/\text{cm}^2$ , which are optimized to ensure proper resist exposure

and pattern fidelity. The exposure field size is set to 1000  $\mu\text{m}$  x 1000  $\mu\text{m}$ , with a field dot density of 1,000,000 dots per field, corresponding to a resolution of 1000 nm. The pitch size, scan pitch, and feed pitch are all configured at 2 nm to ensure uniform exposure and high pattern quality. These parameters are carefully tuned to balance resolution, throughput, and pattern uniformity.

EBL's ability to directly write patterns with high precision enables the accurate definition of critical features on the resist, such as the disk, waveguide, and grating structures, which are essential for the sensor's functionality. This high level of control is particularly advantageous in research and development environments where rapid prototyping of novel designs is required. By utilizing the advanced capabilities of the Elionix EBL system, this fabrication step ensures the creation of intricate and highly accurate patterns essential for the device's performance.

### *3.5.3 Development*

After exposure, the first step is to remove the discharge layer from the sample. This is done at the wet chemistry fume hood by rinsing the sample under running DI water for 30 seconds, followed by blow-drying with a nitrogen gun to ensure the surface is clean and dry. The sample is then immersed in a tetramethylammonium hydroxide (TMAH) developer, which has been poured into a beaker and pre-heated on a hotplate to 45°C. A beaker of DI water is prepared in advance, and once the sample has been in the developer for 1 minute, it is immediately immersed in the DI water to stop the development process. The sample is held in the water for 1 minute, then gently rinsed under running DI water to ensure all developer residues are removed. Afterward, the sample is blow-dried with a

nitrogen gun and inspected to verify the development process and pattern integrity. The TMAH serves to dissolve the unexposed regions of the resist, revealing the underlying pattern transferred during the exposure process.

Once the development is complete, the sample is inspected under an optical microscope to verify that the transferred pattern is clearly visible and properly developed. This step allows for a preliminary check of the pattern's integrity and uniformity. For more detailed analysis, the sample is examined under a scanning electron microscope (SEM) to assess the fine features of the pattern, particularly the sharpness and definition of the edges, which are critical for high-resolution fabrication.

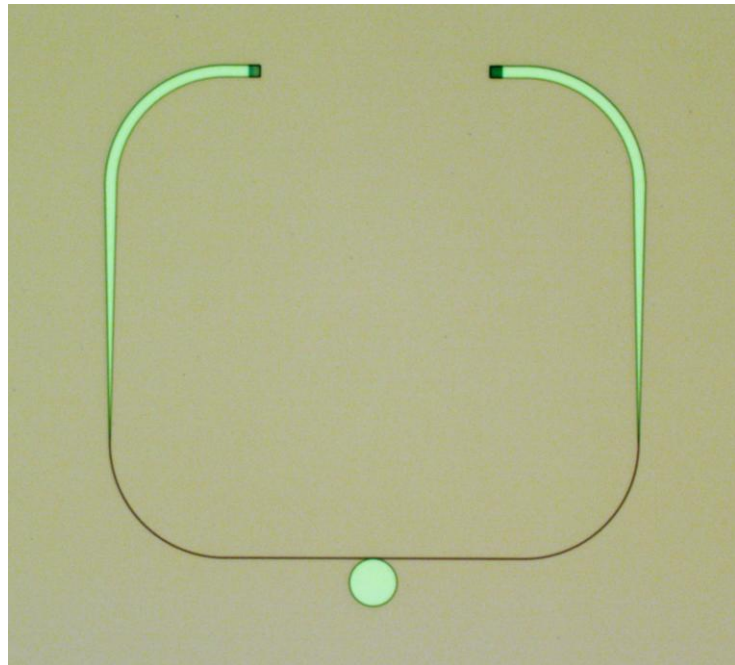


**Figure 32 – Optical microscope image of the device after first layer patterning.**

To ensure that the resist layer has been developed to the specified thickness of approximately 750 nm, a Tencor profilometer is used to measure the resist thickness. This measurement confirms whether the development process has successfully retained

the intended resist profile. Any deviations from the specified thickness can indicate issues with the exposure or development process, which can then be addressed before proceeding to the next fabrication steps. These inspections and measurements are essential to ensure the quality and accuracy of the patterning process, which directly impacts the functionality of the final device.

## **3.6 Dry Anisotropic Etching**

### *3.6.1 Inductively Coupled Plasma Etching*

Inductively Coupled Plasma (ICP) etching is a high-precision dry etching process widely used in nanofabrication for creating smooth, vertical sidewalls. This process relies on high-density plasma generated by inductively coupling RF power into a chamber filled with reactive gases. ICP etching offers several advantages, including superior etch rate control, excellent uniformity, and the ability to create well-defined vertical profiles, making it ideal for dielectric etching and nanoscale fabrication. Unlike other etching methods, ICP etching provides the precision required for intricate designs, such as those found in advanced MEMS and sensor devices.

At Georgia Tech, ICP etching is performed using the Plasma Therm Versaline ICP in the Marcus Cleanroom or the Plasma Therm ICP in the Pettit Microelectronics Building. The Plasma Therm Versaline ICP in Marcus is specifically designed for etching dielectric materials, such as SiO and SiN, while ensuring smooth and vertical sidewalls. This system is configured to handle 100 mm wafers but can also accommodate 200 mm wafers or smaller samples mounted on a carrier wafer. Samples are held in place using a ceramic mechanical clamp, and helium backside cooling is employed to maintain thermal

stability. The substrate holder temperature is controlled via a heat exchanger, with a temperature range of 10°C to 60°C, to optimize etching conditions. The tool supports various processing gases, including CF<sub>4</sub>, CHF<sub>3</sub>, SF<sub>6</sub>, O<sub>2</sub>, and Ar, allowing versatility in etching applications.

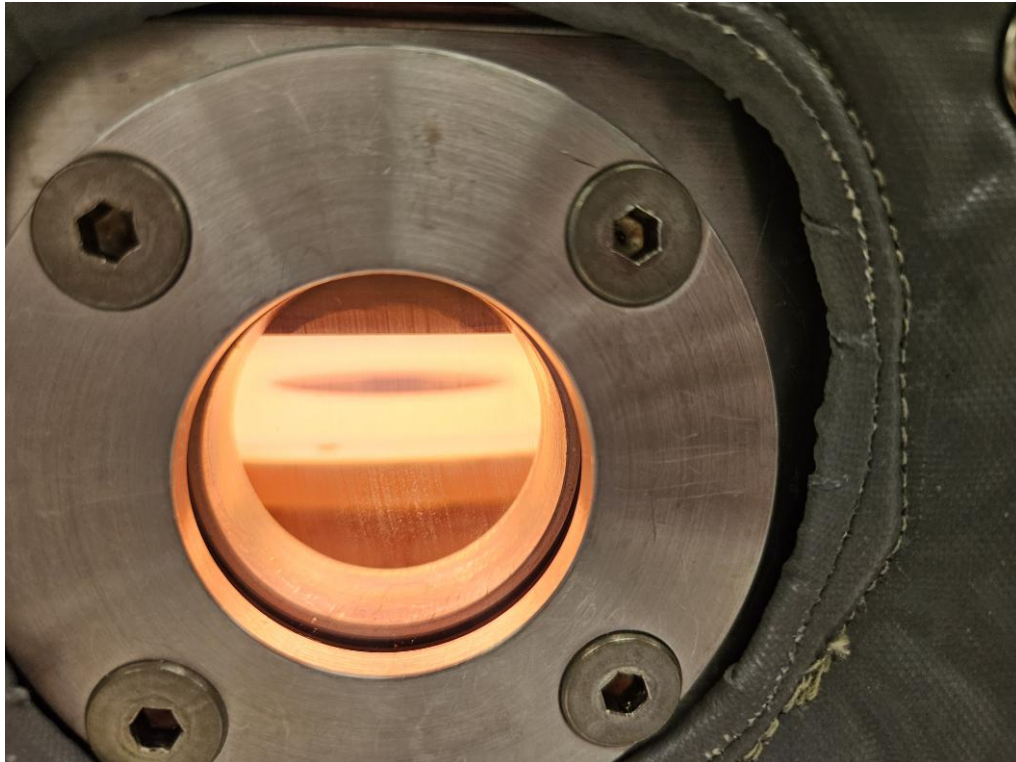


**Figure 33 – Plasma during dry etching using the Plasma Therm ICP in the Pettit Microelectronics Building.**

The specific recipe used for this process includes 10 sccm of Argon (Ar), 10 sccm of Oxygen (O<sub>2</sub>), and 50 sccm of CF<sub>4</sub>, with an RF power of 250 W. To prepare the sample, a thin, uniform layer of cool grease is applied to the backside of the sample using a cleanroom swab. The sample is then gently pressed from the sides onto the carrier wafer to ensure secure attachment.

Before etching the actual sample, the etch rate of the machine is determined using test samples of LPCVD silicon nitride and ALD silicon oxide, both deposited on bare silicon. The initial thickness of these test samples is measured using optical methods, such as the NanoSpec or ellipsometer, as there is no step or pattern suitable for profilometer measurements. The test samples are then etched for one minute, and their thickness is re-measured to determine the etch rate for that day or run. Based on the etch rate, the total time required to etch the actual sample by 650 nm is calculated. This includes etching the top silicon nitride layer, the silicon oxide layer, and most of the bottom silicon nitride layer, leaving a small pedestal.

Once the etch time is determined, the actual sample is adhered to the carrier wafer and placed into the Plasma Therm ICP for etching. After the etch process is complete, the sample is removed by using acetone to release it from the carrier wafer. The sample is then cleaned using acetone, isopropanol, and DI water, followed by blow-drying.

The etch rate of FOX-16 is close to that of silicon oxide, and it is generally assumed to have a 1:1 etch ratio. For this reason, the FOX-16 resist is applied with an initial thickness of 750 nm, as the process is designed to etch 650 nm of material, leaving a small protective layer of resist. This remaining layer can later be measured using a profilometer to verify the etch rate of FOX-16 and ensure the process was performed accurately. This approach provides a simple yet effective method to confirm the consistency and reliability of the etching process while maintaining the integrity of the underlying material.

### *3.6.2 Resist Removal*

The removal of the remaining FOX-16 resist was carried out using Buffered Oxide Etch (BOE). The BOE solution was poured into a Teflon beaker, and appropriate personal protective equipment, including gloves, an apron, and safety goggles, was worn. A beaker of DI water was prepared in advance for rinsing. The sample was immersed in the BOE solution for 4–5 seconds and then immediately transferred to the DI water beaker to stop the etching process. Afterward, the sample was rinsed thoroughly under running DI water and blow-dried with a nitrogen gun.

Before removing the resist, the sample was inspected, and a Tencor profilometer was used to measure the thickness of the remaining FOX-16 resist and the unetched areas beneath it. This provided a baseline measurement of the resist layer and any remaining material. After the FOX-16 resist was removed with BOE, the sample was measured again using the profilometer to confirm that all residual resist had been eliminated. By comparing these measurements with the known initial thickness of the resist, the etch rate of FOX-16 was calculated, ensuring that the removal process was effective and consistent.

The total etch depth was also measured to ensure it aligned with the target 650 nm, corresponding to the removal of the top silicon nitride layer, the silicon oxide layer, and part of the bottom silicon nitride layer. This confirmed that the etching process achieved the intended results, leaving a pedestal.

### **3.7 Second Patterning and Alignment**

The second part of the fabrication process involves undercutting or slot creation in the silicon oxide ALD layer of the disk. This step is critical for defining the slot

geometry, which impacts the optical and structural properties of the device. The process begins by coating the entire sample with a positive tone resist and patterning openings only above the disk areas using electron beam lithography (EBL). These openings expose the silicon oxide layer in the slot area, allowing the wet etchant, BOE (Buffered Oxide Etch), to penetrate and selectively etch 2–3  $\mu\text{m}$  inward into the disk. The etching is carefully controlled to ensure uniformity and prevent over-etching. All other regions, including the waveguide and grating, are protected by the resist layer to maintain their structural integrity.

Since this is the second layer to be patterned, precise alignment is required. This is achieved using the EBL machine, where an alignment mark in the shape of a cross, measuring 5  $\mu\text{m}$  in width and 400  $\mu\text{m}$  in length, is utilized. The alignment mark ensures accurate overlay of the new pattern with the existing features, which is essential for maintaining the device's functionality and minimizing fabrication errors.

### 3.7.1 Positive Resist Spin Coating

To create openings on top of the disk areas while covering everything else, a positive-tone resist is required. A circular pattern slightly larger than the disk is exposed on top of the disk area. Upon development, the exposed resist is removed, while the unexposed regions remain intact.

**Table 5 – 950 PMMA A6 Positive Resist target thickness 1000 nm.**

Step	Time	Speed	Acceleration
1	5	500	450
2	45	1000	800

The positive-tone resist used in this process is PMMA A6, with a target thickness of 1000 nm. Table 5 presents the spin-coating recipe used to achieve this thickness. After spin coating, the sample is baked on a hot plate for 1 minute and 30 seconds at a temperature of 180 °C.

To verify the thickness of the resist produced by the recipe, a bare silicon sample can be spin-coated and baked using the same procedure. The thickness can then be characterized using a NanoSpec or Woollam ellipsometer, ensuring the target thickness of 1000 nm is met consistently.

After applying PMMA, a discharge layer is spin-coated onto the sample to prevent charge buildup during electron beam exposure using the recipe detailed in Table 4, and no baking is required after this step.

### *3.7.2 Alignment and EBL Exposure*

The PMMA A6 resist is exposed using the electron beam lithography (EBL) system in the Marcus cleanroom. The resist, with a thickness of 1000 nm, is patterned under the same operational parameters as before. The electron beam operates with a current of 1 nA, while the exposure dose is adjusted to a range of 700  $\mu\text{C}/\text{cm}^2$ . This dose ensures adequate energy delivery to the resist, enabling clean removal of the exposed regions during development without damaging the unexposed areas. Since this is the second layer of the fabrication process, alignment is performed before exposure to ensure precise overlay with the previously patterned features. These carefully chosen parameters, combined with accurate alignment, enable the precise definition of high-resolution patterns necessary for the fabrication of nanoscale structures.

### 3.7.3 PMMA Development

After exposure, the first step is to remove the discharge layer from the sample. This is done at the wet chemistry fume hood by rinsing the sample under running DI water for 30 seconds, followed by blow-drying with a nitrogen gun to ensure the surface is clean and dry. The sample is then developed to remove the exposed regions of the PMMA A6 resist. A solution of 3:1 IPA:DI water is prepared in a quartz beaker in the chemical fume hood. The sample is immersed in this solution for 1 minute, followed by immersion in IPA for 30 seconds.

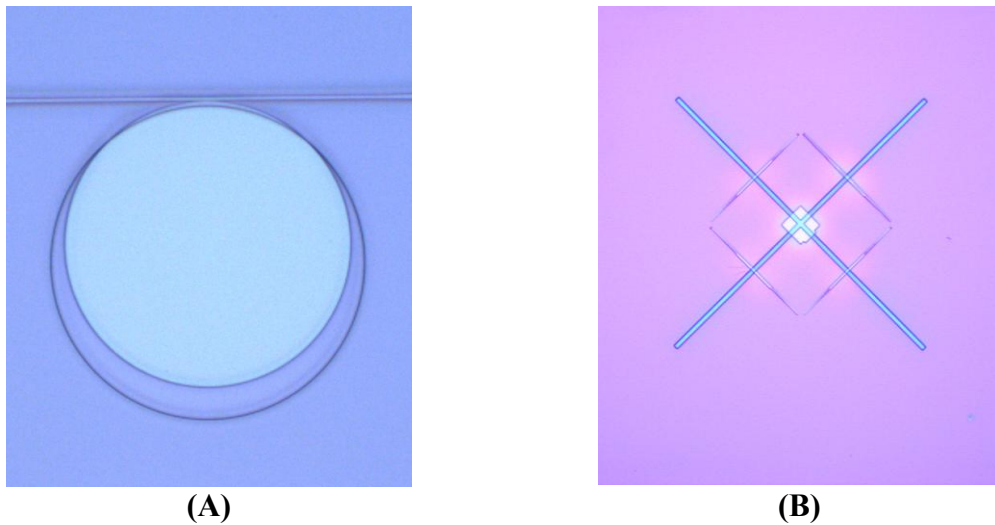


**Figure 34 – (A) Optical microscope image of the second patterning step, showing PMMA covering the sample except for a circular opening around the disk. (B) Alignment mark after being scanned by the EBL machine.**

Afterward, the sample is blow-dried with a nitrogen gun. The developed pattern is then inspected following standard development procedures previously described, ensuring that the resist is properly developed, and the desired features are accurately

transferred. After development, a post bake for 5 min at 150°C can be done to further harden the PMMA before using BOE.

### **3.8 Undercutting of Horizontal Slot**

#### *3.8.1 Slot Undercutting by Wet Etching With BOE*

At this stage, openings to the disk area are created, and a protective silicon nitride pedestal is present on top of the lower BOX silicon oxide layer to safeguard it during the BOE wet etching process. The etched layer is the sandwiched ALD silicon oxide slot layer. The sample is immersed in BOE, which is poured into a Teflon beaker, with appropriate personal protective equipment (PPE) worn during handling. The time required to etch inward by 3  $\mu\text{m}$  was approximately 20 minutes. The etch depth is monitored using SEM top-view imaging of the disk. During etching, the sample is gently agitated to ensure the BOE solution reaches all exposed areas uniformly. After etching, the sample is immersed in DI water, thoroughly rinsed, and blow-dried with a nitrogen gun.

#### *3.8.2 Resist Removal*

PMMA resist is typically cleaned off by immersing the sample in acetone, which effectively dissolves the resist. For enhanced results, the acetone can be heated to 50–70 °C to accelerate the removal process.

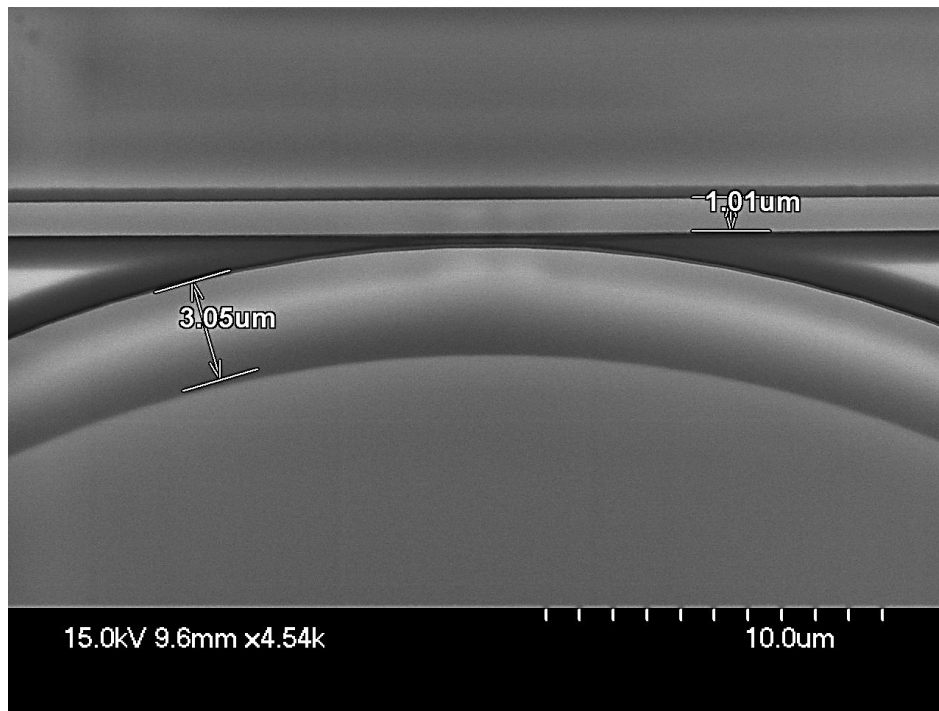
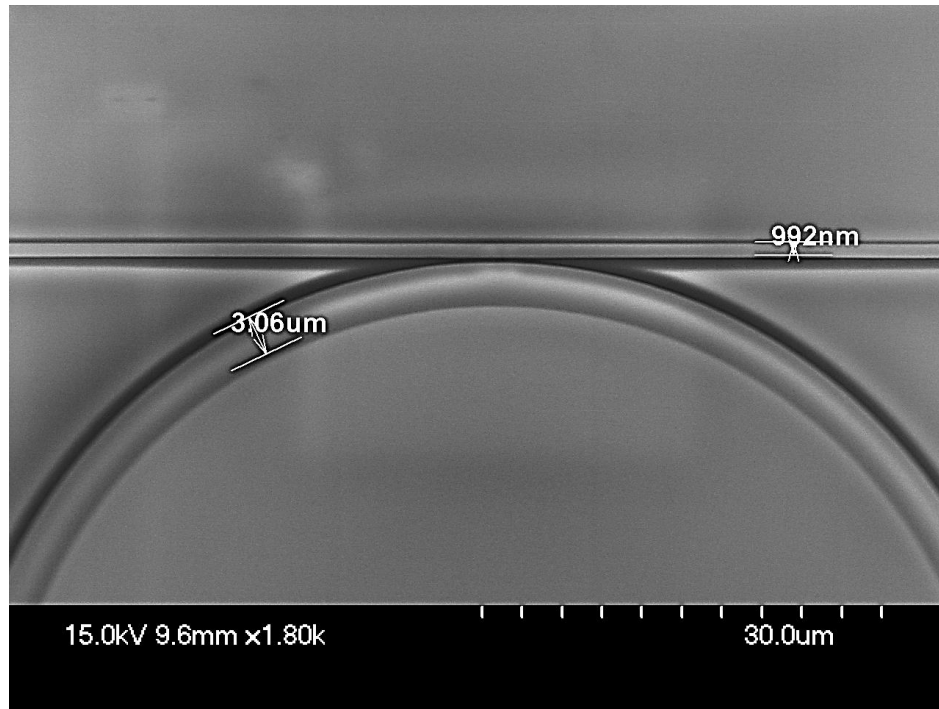


**Figure 35 – Scanning electron microscope (SEM) images showing the waveguide and undercut disk, representing the final device features. The slot depth is 3 μm, waveguide width is 1 μm. No gold layer was evaporated on the sample to enhance SEM imaging, resulting in slight charging effects.**

The sample is usually left in the acetone bath for 5–10 minutes to ensure complete removal. In cases where the resist is more stubborn, gentle ultrasonic agitation in the acetone bath may be applied to assist in removing residual resist. Also, soaking the sample in room temperature acetone overnight, can be used to remove the resist. After soaking in acetone, the sample is thoroughly rinsed with isopropanol (IPA) to eliminate any remaining traces of resist and acetone. Finally, the sample is dried using a nitrogen gun to prevent streaks or contamination, ensuring a clean surface. If any residual resist or organic contamination remains, the sample can undergo oxygen plasma cleaning, which oxidizes and removes the remaining material, leaving the surface pristine.

## CHAPTER 4. CHARECTERIZATION OF DEVICE

In this chapter, the characterization and experimental evaluation of the WGM horizontal slot micro-disk sensor are presented. A tunable laser source operating in the infrared range (1260–1360 nm) was employed for optical characterization. The sensor performance was investigated for both bulk chemical sensing and bio-molecular surface layer sensing. High quality factors were observed, providing the experimental foundation for assessing the sensor's performance and validating the design and simulation work described in the previous chapters.

### 4.1 Qualify Factor Analysis

The quality factor of the device was measured in air before and after the annealing process, as well as before the undercutting step, to evaluate the effect of thermal treatment on optical performance. The quality factor was then measured again in water after undercutting, allowing for a direct comparison between the device's performance in air and in its final sensing environment. This comparison provides insight into fabrication process impacts and the influence of the surrounding medium on the resonator's optical properties.

#### 4.1.1 *Qualify Factor Before Annealing*

The device exhibited a loaded quality factor of approximately 219,000, and an intrinsic quality factor of around 434,000 was extracted using the equation [54, 55]. Such a high-quality factor indicates low optical losses and strong confinement of light within the resonator, which are essential for achieving high sensitivity in sensing applications.

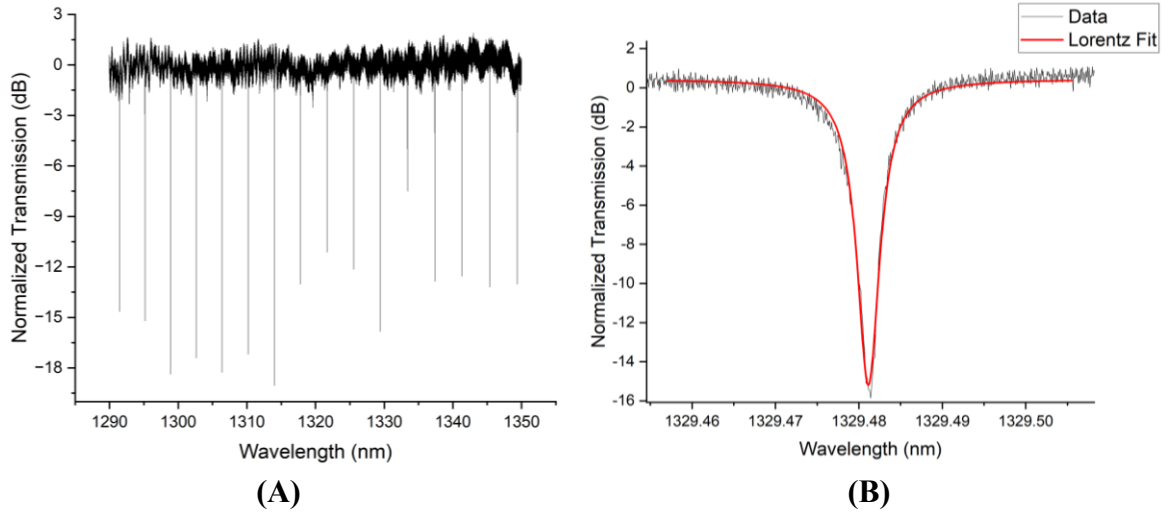


**Figure 36 – (A) Transmission spectrum of the device before annealing in air, showing mode peaks separated by FSR of 3.8 nm. (B) Resonance peak with Lorentzian fitting for the highest quality factor before annealing in air.**

This performance can be attributed to the high fabrication quality, including smooth sidewalls from optimized etching, low material absorption in the silicon nitride layers, and well-controlled coupling conditions. The free spectral range (FSR) was measured to be 3.8 nm. Figure 36(B) shows the resonance peak corresponding to the highest quality factor, where Lorentzian fitting was used to estimate its value.

#### 4.1.2 *Quality Factor After Annealing*

After annealing at 1100 °C for 12 hours, the device exhibited a loaded quality factor of approximately 502,000, and an intrinsic quality factor of about 1,003,000 at a resonance wavelength of 1329.4167 nm. This represents roughly a 2.3-fold increase compared to the pre-annealing measurement. The improvement is attributed to several mechanisms that occur during high temperature annealing of silicon nitride micro-resonators. First, annealing removes hydrogen-related impurities such as N–H and Si–H bonds from the structure, which reduces absorption losses in the near-infrared range [58,

59]. Second, thermal treatment promotes crystal rearrangement and atomic relaxation, resulting in a more ordered material network with reduced scattering [56]. Third, the process releases internal film stress, which minimizes stress-induced defects and stabilizes the refractive index [57]. Finally, annealing helps eliminate dangling bonds at the surface and within the bulk material, further lowering optical absorption and scattering losses [61].

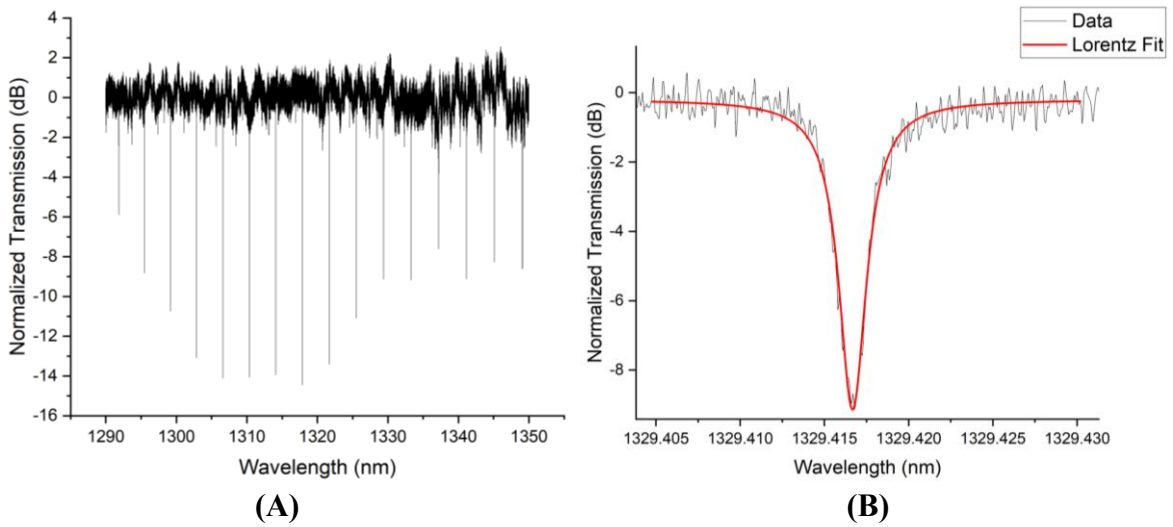


**Figure 37 – (A) Transmission spectrum of the device after annealing, showing the same FSR of 3.8 nm and higher quality factors. (B) Resonance peak with Lorentzian fitting for the highest quality factor after annealing.**

The free spectral range (FSR) remained at 3.8 nm. Figure 37(B) shows the resonance peak corresponding to the highest quality factor, where Lorentzian fitting was used to estimate its value.

#### 4.1.3 *Quality Factor with Water Cladding*

After annealing and undercutting, the device was characterized in deionized (DI) water at room temperature. A small droplet of water was placed over the disk area,

ensuring complete coverage of the sensing region. The loaded quality factor was approximately 161,000, and the intrinsic quality factor was about 321,000. The corresponding resonance exhibited a full width at half maximum (FWHM) of 0.00805 nm, with a standard deviation of 0.00031 nm calculated from several sequential measurements of the device with a water cladding.

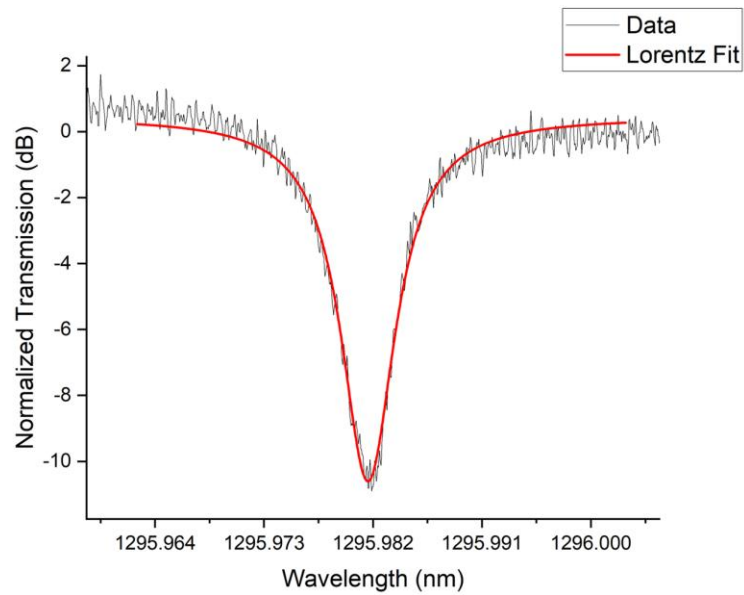


**Figure 38 – Resonance peak with Lorentzian fitting corresponding to the highest quality factor for the device measured with water cladding.**

Compared to the intrinsic quality factor measured in air after annealing, this represents a decrease by a factor of approximately 3.1. The reduction in quality factor is primarily attributed to three factors. First, absorption losses from water in the near-infrared wavelength range increase attenuation of the circulating optical field [59]. Second, the lower refractive index contrast between the resonator and the water cladding increases coupling to radiation modes, thereby enhancing scattering losses [60]. Third, possible perturbations to the optical mode from surface interactions with the liquid cladding can introduce additional loss pathways [61].

## 4.2 Bulk Chemical Sensing Results

The performance of the WGM horizontal slot micro-disk sensor for bulk chemical sensing was evaluated using sodium chloride (NaCl) solutions of different concentrations. Small droplets were placed over the disk area to serve as the sensing medium, and all measurements were performed at room temperature. The refractive index values corresponding to each NaCl concentration were obtained from sources [48, 53]. The transmission spectra were recorded for each concentration to monitor the resonance response.

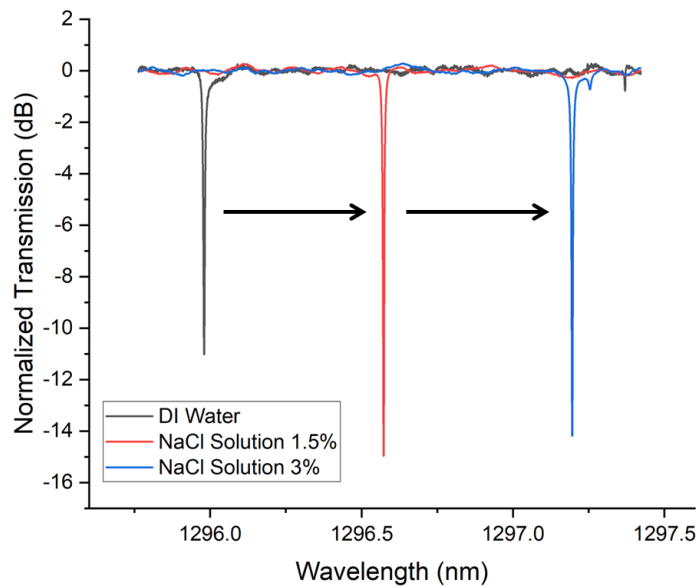


**Figure 39 – Single azimuthal mode resonance peaks showing a redshift with increasing NaCl solution concentration.**

Figure 39 shows a single azimuthal mode shifting in resonance wavelength as the NaCl concentration increases, indicating effective bulk refractive index sensing. The resonance shift consistently moves toward longer wavelengths with increasing concentration, reflecting the higher refractive index of the surrounding medium.

The bulk refractive index sensitivity was determined from the linear fit of the resonance wavelength shift versus the refractive index of the NaCl solutions, using the equation [1]. A sensitivity of 265 nm/RIU was obtained, indicating a strong response of the sensor to changes in the surrounding refractive index.

The limit of detection was calculated using the standard deviation of the measured resonance peak positions and the bulk sensitivity value, following the equation [3]. The LOD was found to be  $3.5 \times 10^{-6}$  RIU, demonstrating the capability of the device to detect extremely small changes in the refractive index of the surrounding medium.

The performance of the device was further evaluated using the sensitivity-to-FWHM ratio (S/FWHM), a metric that reflects the sensor's ability to detect small refractive index changes (sensitivity) while also accounting for the sharpness of the resonance peak (spectral resolution) [20]. For the WGM horizontal slot micro-disk sensor, the obtained value was  $3.3 \times 10^4$  RIU<sup>-1</sup>. This result surpasses the performance of the single-layer nitride spiral-based resonator reported in [10], which has previously been considered the highest value for this figure of merit. These findings demonstrate the strong sensing efficiency of the slot micro-disk geometry, highlighting its advantage for high-performance refractive index sensing applications.

### **4.3 Bio-molecular Layer Sensing Results**

#### *4.3.1 Troponin Detection and Its Significance in Photonic Sensing*

Cardiac troponin is a critical biomarker for diagnosing acute myocardial infarction (AMI), commonly known as a heart attack. It is released into the bloodstream when the

heart muscle is damaged, making its presence and concentration in blood a direct indicator of cardiac injury. Among the various isoforms, Troponin I (cTnI) is highly specific to cardiac tissue and has become the gold standard for early detection of cardiac events. Traditional immunoassays used in clinical settings typically require time-consuming procedures and bulky equipment. In contrast, integrated photonic sensors offer a rapid, label-free, and highly sensitive alternative for detecting troponin directly in small fluid volumes. In this work, we utilize a silicon nitride-based whispering gallery mode (WGM) micro-disk sensor, functionalized to selectively capture Troponin I, enabling real-time monitoring of antigen-antibody binding events through measurable resonance wavelength shifts.

#### 4.3.2 *Surface Functionalization Procedure*

The first step in the functionalization process is surface cleaning and activation. The silicon nitride sensor surface is cleaned to remove contaminants and activate it with hydroxyl ( $-OH$ ) groups, which are essential for chemical bonding in the next steps. The chip is first immersed in a freshly prepared piranha solution ( $H_2SO_4:H_2O_2 = 3:1$ ) at  $50\text{ }^\circ\text{C}$  for 30 minutes. This process oxidizes and removes organic residues, leaving a hydroxyl-rich surface. After this step, the chip is thoroughly rinsed with deionized (DI) water and dried using a nitrogen flow. To further enhance surface reactivity, the chip is then exposed to UV-ozone for 15 minutes, which removes residual carbon and increases the density of  $-OH$  groups. After UV-ozone treatment, the chip is again rinsed with DI water and dried using nitrogen flow. Finally, the chip is baked on a hotplate at  $110\text{ }^\circ\text{C}$  for 5 minutes to fully dehydrate the surface. The result is a clean, hydroxyl-terminated ( $-OH$ ),

hydrophilic surface ready for silanization. A representative image showing a water droplet on the cleaned chip with a low contact angle is provided in Figure 40.

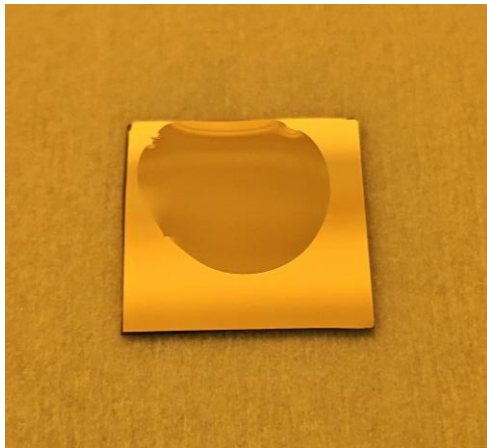


**Figure 40 – Water droplet on a chip following step one surface cleaning. The low contact angle ( $\sim 10^\circ$ ) provides clear evidence of successful surface hydroxylation and high hydrophilicity.**

In the second step, the hydroxylated silicon nitride surface is functionalized with (3-Aminopropyl)triethoxysilane (APTES) to introduce terminal amine ( $-\text{NH}_2$ ) groups, which are necessary for subsequent attachment of biomolecules. A 2% (v/v) solution of APTES in 2-propanol is prepared, and the chip is immersed in this solution for 1 hour at room temperature. After incubation, the chip is rinsed thoroughly, first with 2-propanol to remove excess silane, then with DI water, and dried using a nitrogen gun. The chip is then baked in two stages: 10 minutes at  $110^\circ\text{C}$  followed by 20 minutes at  $120^\circ\text{C}$  to cure and stabilize the silane layer. The result is a surface covalently functionalized with a uniform APTES layer exposing terminal amine ( $-\text{NH}_2$ ) groups for further coupling. The effectiveness of the second step can be evaluated through water contact angle measurements, which typically increase to between  $60^\circ$  and  $80^\circ$ , indicating the presence

of a more hydrophobic, organic amine-terminated surface. A representative image showing a water droplet on the APTES-treated chip is provided in Figure 41.

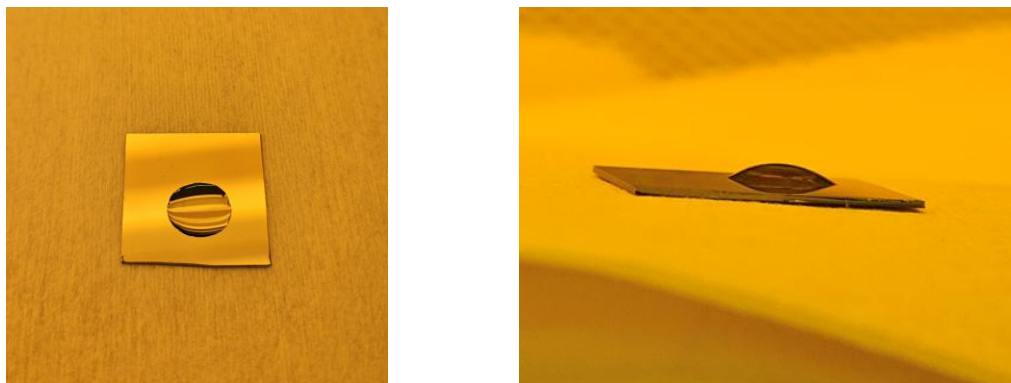


**Figure 41 – Water droplet on a chip after the second step (APTES silanization). The increased contact angle ( $\sim 60^\circ$ ) confirms successful formation of a hydrophobic amine-functionalized surface.**

In the third step, the amine-functionalized surface is treated with glutaraldehyde to introduce reactive aldehyde (CHO) groups. A 2.5% (v/v) glutaraldehyde solution is prepared in phosphate-buffered saline (PBS), and the chip is immersed in the solution for 1 hour at room temperature. After incubation, the chip is gently rinsed with PBS to remove unbound glutaraldehyde. The result is a surface functionalized with aldehyde (CHO) groups, ready for attachment of proteins or other amine-containing biomolecules.

In the fourth step, Troponin I antibodies are immobilized on the aldehyde-functionalized surface. A solution of Troponin I antibody is prepared at a concentration of 50 - 100  $\mu\text{g}/\text{mL}$  in phosphate-buffered saline (PBS), and the chip is incubated in this solution for 1 hour at room temperature. After incubation, the chip is gently rinsed with PBS to remove any unbound or loosely attached antibodies. The result is a surface with antibodies securely anchored to the chip, enabling specific binding to the target Troponin

I antigen. The chip should proceed directly to the blocking step to prevent nonspecific binding.

In the fifth step, remaining reactive aldehyde (CHO) groups on the surface are blocked to prevent nonspecific binding. The chip is first incubated in 100 mM ethanolamine prepared in phosphate-buffered saline (PBS) for 1 hour at room temperature. After that, the chip is incubated in 0.1% casein solution prepared in PBS for 30 minutes at room temperature. Following incubation, the chip is rinsed thoroughly with PBS. The result is a fully passivated surface that minimizes nonspecific interactions during sensing.

In the sixth step, the functionalized sensor surface is exposed to the target analyte, Troponin I antigen. The antigen is prepared in phosphate-buffered saline (PBS) at the desired concentration, and the chip is incubated in this solution for 1 hour at room temperature. After incubation, the chip is gently rinsed with PBS to remove any unbound antigen. The result is specific binding of Troponin I antigen to the immobilized antibodies, producing a measurable change in the sensor's optical signal, typically observed as a resonance wavelength shift, which confirms the presence of bound Troponin I.

#### *4.3.3 Surface Sensitivity Measurement Using Troponin*

To evaluate the surface sensing performance of the WGM horizontal slot micro-disk sensor, the device was functionalized for Troponin I detection. At the high concentration used, the protein layer reached saturation, fully covering the functionalized surface. Troponin I, as a globular protein, is known to form layers of approximately 3–5

nm thickness in biosensing applications; for consistency with literature, a saturated layer thickness of  $\sim 4$  nm is assumed [20]. When exposed to Troponin I, the resonance peak redshifted by 1.11 nm. Based on this shift and the assumed molecular layer thickness, the surface sensitivity  $S_{\text{surface}}$  is approximately 278 pm/nm. This high value highlights the strong overlap between the evanescent field and the biomolecular layer, emphasizing the effectiveness of the horizontal slot design for biosensing applications.

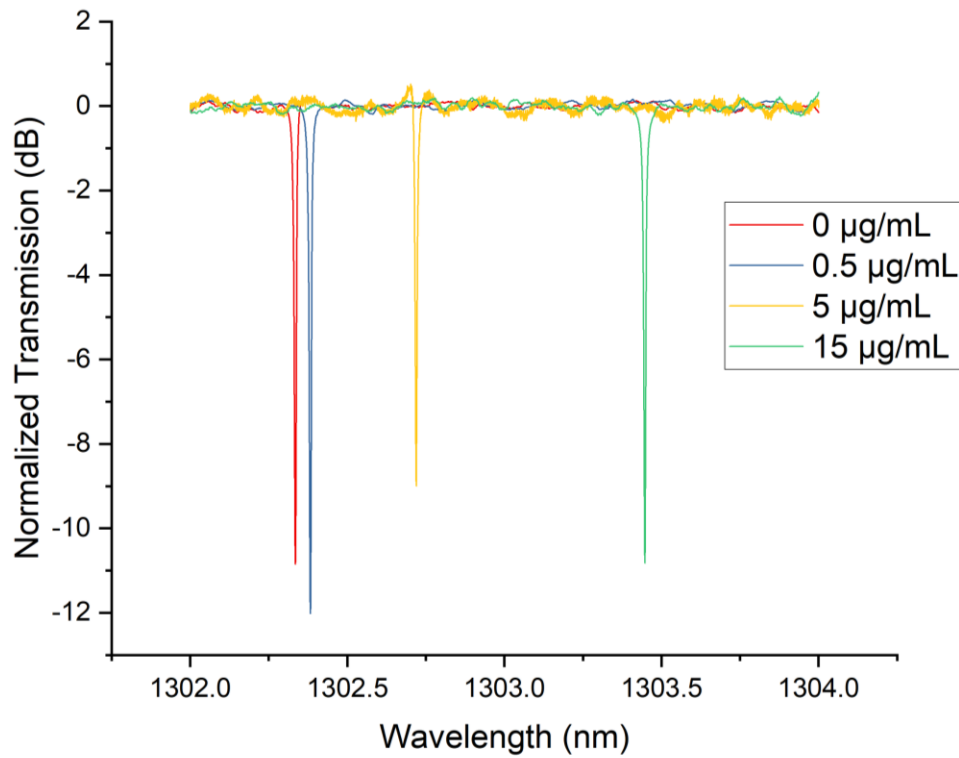


**Figure 42 – Shifts in resonance frequency due to different concentrations of Troponin.**

## CHAPTER 5. CONCLUSION AND FUTURE WORK

This work presented the design, fabrication, characterization, and application of a high-quality horizontal slot micro-disk resonator for integrated photonic sensing. The research addressed key limitations in whispering gallery mode (WGM) sensors by introducing a structure that enhances light-analyte interaction while maintaining high optical quality factors, enabling both chemical and biomolecular detection with high sensitivity and low limits of detection (LOD). The major technical contributions of this work are summarized below.

### 5.1 Summary of Technical Contributions

A significant contribution of this work is the introduction and optimization of a horizontal slot disk resonator design. Unlike conventional planar or vertical slot resonators, the horizontal slot geometry enables the optical field to extend strongly into the low-index slot region, which is in direct contact with the analyte. Numerical simulations demonstrated that this design yields stronger confinement of the optical mode at the sensing interface, thereby improving bulk and surface sensitivity. Comparative analysis of planar, vertical, and horizontal slot configurations confirmed the superiority of the horizontal slot design in terms of mode overlap and refractive index response, particularly at wavelengths of 780 nm and 1300 nm. Simulations predicted bulk sensitivities of  $\sim 392$  nm/RIU, a significant improvement over earlier nitride-based resonators.

Another central contribution lies in the development of a complete nanofabrication process to realize the proposed device. The process combined thermal wet oxidation, low-pressure chemical vapor deposition (LPCVD), and atomic layer deposition (ALD) for multilayer stack formation. Electron-beam lithography (EBL) using both negative (HSQ) and positive (PMMA) resists enabled nanoscale slot patterning, followed by inductively coupled plasma (ICP) etching for precise definition of the disk geometry. Buffered oxide etching (BOE) was employed for undercutting to suspend the structure, enhancing interaction with the analyte. This process sequence, refined through extensive experimentation, successfully produced smooth sidewalls and minimized slot collapse, leading to devices with low scattering loss and high reproducibility. The optimized fabrication methodology represents a scalable path toward CMOS-compatible integration of slot micro-disk sensors.

Systematic optical characterization of the fabricated resonators confirmed the high-performance potential of the horizontal slot design. Using a tunable infrared laser (1260–1360 nm), loaded and intrinsic quality factors were measured in air, after annealing, and in DI water. Prior to annealing, the devices exhibited loaded Q factors around 219,000, with intrinsic values near 434,000. After annealing at 1100 °C for 12 hours, the Q factor improved dramatically, reaching ~502,000 loaded and ~1,003,000 intrinsic. This ~2.3-fold enhancement was attributed to the removal of hydrogen-related impurities (N–H and Si–H bonds), atomic rearrangement, stress relaxation, and elimination of dangling bonds during thermal treatment. In DI water, the intrinsic Q decreased to ~321,000 due to absorption losses, reduced index contrast, and perturbations from the liquid interface. Nevertheless, this still represented robust performance in a realistic sensing environment.

Achieving an intrinsic Q above one million stands as a key milestone of this work, demonstrating the ability of the horizontal slot micro-disk to combine strong analyte interaction with exceptionally low optical loss.

The sensor's chemical sensing performance was experimentally validated using NaCl solutions of varying concentrations at room temperature. Resonance shifts were observed as droplets of different solutions were placed on the disk surface, producing a clear redshift with increasing concentration. From these measurements, the bulk refractive index sensitivity was determined to be 265 nm/RIU. The limit of detection (LOD), derived from the resonance peak variation and sensitivity, was calculated as  $3.5 \times 10^{-6}$  RIU. In addition to these conventional metrics, the performance was further evaluated using the sensitivity-to-FWHM ratio (S/FWHM). For the horizontal slot disk, this value was found to be  $3.3 \times 10^4$  RIU<sup>-1</sup>, which surpasses the reported performance of single-layer nitride spiral resonators previously considered state-of-the-art. The combination of high sensitivity, low LOD, and a record-high S/FWHM figure of merit underscores the device's ability to detect minute refractive index changes with high precision and efficiency.

Beyond bulk sensing, the sensor was applied to biomolecular surface detection using Troponin I, a clinically relevant cardiac biomarker. The functionalized device was incubated with a high concentration of Troponin I to achieve saturation coverage, corresponding to an estimated layer thickness of ~4 nm. Upon binding, the resonance redshifted by 1.11 nm, yielding a calculated surface sensitivity of approximately 278 pm/nm. This result demonstrates the strong overlap of the evanescent field with the biomolecular layer, confirming the slot design's advantage for label-free biosensing.

Importantly, this work establishes a foundation for detecting clinically meaningful biomarkers with high precision using integrated photonic devices.

## 5.2 Future Work

While this dissertation establishes the potential of horizontal slot micro-disk resonators, several important avenues remain open for exploration and advancement.

Future work should prioritize integrating the slot micro-disk with waveguides, grating couplers, and other photonic components. On-chip integration will reduce losses, improve robustness, and enable scalable multiplexed systems. Suspended or tapered waveguides may be required to address challenges posed by undercut geometries. Incorporating on-chip detectors and sources would pave the way toward fully self-contained photonic sensing platforms.

The biosensing results relied on standard APTES/glutaraldehyde chemistry, which, while effective, introduces variability in orientation and nonspecific adsorption. Future efforts should explore silane-PEG linkers for antifouling properties, click-chemistry for controlled biomolecule orientation, and aptamer- or peptide-based functionalization for selective recognition. Optimized surface chemistry will improve specificity, lower detection limits, and allow reliable operation in real biological fluids.

Beyond NaCl and Troponin I, the sensor can be adapted for a wide range of analytes. Environmental sensing applications include detection of toxic heavy metals such as  $\text{Cu}^{2+}$ ,  $\text{Pb}^{2+}$ , and  $\text{Hg}^{2+}$ . Biomedical applications could extend to protein biomarkers (e.g., Troponin T, PSA), nucleic acids, or even viruses. This requires both surface

chemistry optimization and calibration of optical response to different analyte sizes and binding mechanisms.

Scaling the platform to multiplexed sensor arrays offers opportunities for simultaneous detection of multiple analytes. Coupled with microfluidics, such arrays could provide real-time, label-free detection using only microliter volumes of sample. Challenges include maintaining uniform optical coupling and avoiding crosstalk, but these can be mitigated through careful array design. This approach is particularly promising for clinical diagnostics and environmental monitoring.

Exploring alternative materials could further enhance the versatility of slot resonators. Chalcogenide glasses could enable mid-IR operation for molecular fingerprinting, while hybrid integration with 2D materials (e.g., graphene, MoS<sub>2</sub>) could provide tunability and enhanced surface sensitivity. Such material innovations would extend the device's application space to areas like gas sensing or tunable optoelectronics.

Finally, efforts should focus on translating the device into real-world applications. This includes developing packaging strategies for fragile undercut structures, testing stability in physiological and environmental samples, and integrating with electronic readout systems. Combining photonic sensing with wireless electronics could yield portable diagnostic platforms or autonomous IoT nodes for water quality monitoring. Addressing these engineering challenges is critical for moving from laboratory demonstrations to impactful technologies.

## REFERENCES

- [1] V. Passaro, C. De Tullio, B. Troia, M. La Notte, G. Giannoccaro, and F. De Leonardis, "Recent Advances in Integrated Photonic Sensors," *Sensors*, vol. 12, no. 11, pp.15558-15598, Nov. 2012.
- [2] E. Krioukov, D. Klunder, A. Driessen, J. Greve, and C. Otto, "Sensor based on an integrated optical microcavity," *Opt. Lett.*, vol. 27, no. 7, pp. 512-514, Apr. 2002.
- [3] F. Vollmer, D. Braun, A. Libchaber, M. Khoshshima, I. Teraoka, and S. Arnold, "Protein detection by optical shift of a resonant microcavity," *Appl. Phys. Lett.*, vol. 80, no. 21, pp. 4057- 4059, May 2002.
- [4] F. Vollmer, S. Arnold, D. Keng, "Single virus detection from the reactive shift of a whispering-gallery mode," *Proc. Natl. Acad. Sci.*, vol. 105, no. 52, pp. 20701-20704, Dec. 2008.
- [5] C. F. Carlborg et al., "A packaged optical slot-waveguide ring resonator sensor array for multiplex label-free assays in labs-on-chips," *Lab Chip*, vol. 10, no. 3, pp. 281-290, Nov. 2009.
- [6] C. A. Barrios, "Optical Slot-Waveguide Based Biochemical Sensors," *Sensors*, vol. 9, no. 6, Jun. 2009.
- [7] E. Hosseini, S. Yegnanarayanan, A. Atabaki, M. Soltani, and Ali Adibi, "High Quality Planar Silicon Nitride Microdisk Resonators for Integrated Photonics in the Visible Wavelength Range," *Opt. Express.*, vol. 17, no. 17, pp. 14543-14551, Aug. 2009.
- [8] F. Ghasemi et al., "Self-referenced silicon nitride array microring biosensor for toxin detection using glycans at visible wavelength," *Nanoscale Imaging, Sensing, and Actuation for Biomedical Applications X*, vol. 8594, pp. 53-61, Feb. 2013.
- [9] J. Wang, Z. Yao, and A. W. Poon, "Silicon-nitride-based integrated optofluidic biochemical sensors using a coupled-resonator optical waveguide," *Front. Mater.*, vol. 2, no. 34, Apr. 2015.
- [10] X. Wu, T. Fan, A. Eftekhar, A. Hosseinnia, and A. Adibi, "High-Q spiral-based coupled-resonator device on a Si<sub>3</sub>N<sub>4</sub> platform for ultrasensitive sensing applications," *OSA Continuum*, vol. 3, no. 12, pp. 3390-3398, Dec. 2020.
- [11] X. Wu, T. Fan, A. Eftekhar, A. Hosseinnia, and A. Adibi, "High-Q ultrasensitive integrated photonic sensors based on slot-ring resonator on a 3C-SiC-on-insulator platform," *Opt. Lett.*, vol. 46, no. 17, pp. 4316-4319, Aug. 2021.

- [12] F. Khozeymeh, and M. Razaghi, “Sensitivity and intrinsic limit of detection improvement in a photonic refractive-index sensor,” *Optik*, vol. 247, p. 167844, Aug. 2021.
- [13] J. Su, “Label-Free Biological and Chemical Sensing Using Whispering Gallery Mode Optical Resonators: Past, Present, and Future,” *Sensors*, vol. 17, no. 3, p. 540, Mar. 2017.
- [14] E. Kim, M. D. Baaske, and F. Vollmer, “Towards next-generation label-free biosensors: recent advances in whispering gallery mode sensors”, *Lab Chip*, vol. 17, no. 7, pp. 1190-1205, Feb. 2017.
- [15] E. Luan, H. Shoman, D. M. Ratner, K. C. Cheung, and L. Chrostowski, “Silicon Photonic Biosensors Using Label-Free Detection,” *Sensors*, vol. 18, no. 10, p. 3519, Oct. 2018.
- [16] S. Lee, S. Eom, J. Chang, C. Huh, G. Sung, and J. Shin, “A silicon nitride microdisk resonator with a 40-nm-thin horizontal air slot,” *Opt. Express*, vol. 18, no. 11, pp.11209-11215, May 2010.
- [17] S. Lee, S. Eom, J. Chang, C. Huh, G. Sung, and J. Shin, “Label-free optical biosensing using a horizontal air-slot SiNx microdisk resonator,” *Opt. Express*, vol. 18, no. 20, pp. 20638-20644, Sep. 2010.
- [18] S. C. Eom and J. H. Shin, “Design and Optimization of Horizontal Slot Microdisk Sensors,” *IEEE Photon. Technol. Lett.*, vol. 25, no. 19, pp. 1859-1862, Oct. 2013.
- [19] Y. Lin, Z. Yong, X. Luo et al., “Monolithically integrated, broadband, high-efficiency silicon nitride-on-silicon waveguide photodetectors in a visible-light integrated photonics platform,” *Nat. Commun.* vol.13, p. 6362, Oct. 2022.
- [20] X. Wu, “Ultrasensitive CMOS-compatible Lab-on-a-chip Integrated Photonic Sensors with Wideband Operation,” Ph.D. dissertation, Department of Elect. and Comp. Eng., Georgia Tech, Atlanta, 2022.
- [21] K. J. Vahala, “Optical microcavities,” *Nature*, vol. 424, pp. 839-846, Aug. 2003.
- [22] X. Zhao, Z. Guo, Y. Zhou, J. Guo, Z. Liu, Y. Li, M. Luo, and X. Wu, “Optical Whispering-Gallery-Mode Microbubble Sensors,” *Micromachines*, vol. 13, no. 4, p. 592, Apr. 2022.
- [23] L. Rayleigh, “The Problem of the whispering gallery,” *Philos. Mag.*, vol. 20, no. 120, pp. 1001-1004, Dec. 1910.
- [24] M. Foreman, J. Swaim, and F. Vollmer, “Whispering gallery mode sensors,” *Adv. Opt. Photon.*, vol. 7, no.2, pp. 168-240, May. 2015.

- [25] S. Yang, Y. Wang, H. Sun, “Advances and Prospects for Whispering Gallery Mode Microcavities,” *Adv. Opt. Mater.*, vol. 3, no. 9, pp. 1136–1162, Aug. 2015.
- [26] X. Jiang, A. J. Qavi, S. H. Huang, and L. Yang, “Whispering-Gallery Sensors,” *Matter*, vol. 3, no. 2, pp. 371-392, Aug. 2020.
- [27] F. Ghasemi, “Multiplexed Label-free Integrated Photonic Biosensors,” Ph.D. dissertation, Department of Elect. and Comp. Eng., Georgia Tech, Atlanta, 2015.
- [28] L. Cai, J. Pan, Y. Zhao, J. Wang, and S. Xiao, “Whispering Gallery Mode Optical Microresonators: Structures and Sensing Applications,” *Phys. Status. Solidi. A*, vol. 217, no. 6, p. 1900825, Mar. 2020.
- [29] M. Soltani, “Novel Integrated Silicon Nanophotonic Structures Using Ultra-High Q Resonators,” Ph.D. dissertation, Department of Elect. and Comp. Eng., Georgia Tech, Atlanta, 2009.
- [30] Y. Wang, S. Zeng, G. Humbert, and H.-P. Ho, “Microfluidic Whispering Gallery Mode Optical Sensors for Biological Applications,” *Laser Photonics Rev.*, vol. 14, no. 12, p. 2000135, Nov. 2020.
- [31] Y. Zhang, T. Zhou, B. Han, A. Zhang, and Y. Zhao, “Optical bio-chemical sensors based on whispering gallery mode resonators,” *Nanoscale*, vol. 10, no. 29, pp. 13832-13856, Jul. 2018.
- [32] A. Dorche, “Novel framework for integrated nonlinear and quantum photonic signal processing,” Ph.D. dissertation, Department of Elect. and Comp. Eng., Georgia Tech, Atlanta, 2021.
- [33] E. Hosseini, “High quality integrated silicon nitride nanophotonic structures for visible light applications,” Ph.D. dissertation, Department of Elect. and Comp. Eng., Georgia Tech, Atlanta, 2011.
- [34] D. J. Blumenthal, R. Heideman, D. Geuzebroek, A. Leinse, and C. Roeloffzen, “Silicon Nitride in Silicon Photonics,” *Proceedings of the IEEE*, vol. 106, no. 12, pp. 2209-2231, Dec. 2018.
- [35] G. M. Hale and M. R. Querry, “Optical Constants of Water in the 200-nm to 200-microm Wavelength Region,” *Appl. Opt.*, vol. 12, no. 3, pp. 555-563, Mar. 1973.
- [36] V. Almeida, Q. Xu, C. Barrios, M. Lipson, “Guiding and confining light in void nanostructure,” *Opt. Lett.*, vol. 29, no. 11, pp. 1209-1211, Jun. 2004.
- [37] Q. Xu, V. Almeida, R. Panepucci, and M. Lipson, “Experimental demonstration of guiding and confining light in nanometer-size low-refractive-index material,” *Opt. Lett.*, vol. 29, no. 14, pp. 1626-1628, Jul. 2004.

- [38] M. Bryan, J. Butt, J. Bucukovski, and B. Miller, "Biosensing with Silicon Nitride Microring Resonators Integrated with an On-Chip Filter Bank Spectrometer," *ACS Sens.*, vol. 8, no.2, pp.739-747, Feb. 2023.
- [39] L. Castelló-Pedrero, M. Gómez-Gómez, J. García-Rupérez, A. Griol, and A. Martínez, "Performance improvement of a silicon nitride ring resonator biosensor operated in the TM mode at 1310 nm," *Biomed. Opt. Express*, vol. 12, no. 11, pp. 7244-7260, Nov. 2021.
- [40] Y. Hong, H. Ge, and J. Hong, "Compact biosensors based on thin film silicon nitride microring resonators," *J. Phys.: Conf. Ser.*, vol. 2012, p. 012037, Jul. 2021.
- [41] I. Goykhman, B. Desiatov, and U. Levy, "Ultrathin silicon nitride microring resonator for biophotonic applications at 970 nm wavelength," *Appl. Phys. Lett.*, vol. 97, no. 8, p. 081108, Aug. 2010.
- [42] J. Feng and R. Akimoto, "T-Shape Suspended Silicon Nitride Ring Resonator for Optical Sensing Applications," *IEEE Photo. Tech. Lett.*, vol. 27, no. 15, pp. 1601-1604, Aug. 2015.
- [43] C. Doolin, P. Doolin, B. Lewis, and J. Davis, "Refractometric sensing of Li salt with visible-light Si<sub>3</sub>N<sub>4</sub> microdisk resonators," *Appl. Phys. Lett.*, vol. 106, no. 8, p. 081104, Apr. 2015.
- [44] J. Feng, C. Gu, L. Zhong, R. Akimoto and H. Zeng, "Vertically Coupled Suspended Silicon Nitride Microdisk-Based Optical Sensor," *IEEE Photon. Tech. Lett.*, vol. 30, no. 17, pp. 1507-1510, Sep. 2018.
- [45] T. Taniguchi, A. Hirowatari, T. Ikeda, M. Fukuyama, Y. Amemiya, A. Kuroda, S. Yokoyama, "Detection of antibody-antigen reaction by silicon nitride slot-ring biosensors using protein G," *Opt. Commun.*, vol. 365, pp. 16-23, Apr. 2016.
- [46] C. Barrios, K. Gylfason, B. Sánchez, A. Griol, H. Sohlström, M. Holgado, and R. Casquel, "Slot-waveguide biochemical sensor," *Opt. Lett.* vol. 32, no. 21, pp. 3080-3082, Nov. 2007.
- [47] K. B. Gylfason et al., "On-chip temperature compensation in an integrated slot-waveguide ring resonator refractive index sensor array," *Opt. Express*, vol.18, no. 4, pp. 3226-3237, Feb. 2010.
- [48] X. Li, L. Liu, J. Zhao, and J. Tan, "Optical Properties of Sodium Chloride Solution within the Spectral Range from 300 to 2500 nm at Room Temperature," *Applied Spectroscopy*, vol. 69, no. 5, pp. 635-640, May 2015.
- [49] I. White and X. Fan, "On the performance quantification of resonant refractive index sensors," *Opt. Express*, vol. 16, no. 2, pp. 1020-1028, Jan. 2008.

- [50] A. Yakuhina, A. Kadochkin, D. Gorelov, V. Svetukhin, S. Generalov, and V. Amelichev, "Influence of the Surface Roughness of a Silicon Disk Resonator on Its Q-Factor," *Photonics*, vol. 8, no. 6, p. 225, Jun. 2021.
- [51] G. Lin et al., "Dependence of quality factor on surface roughness in crystalline whispering-gallery mode resonators," *Opt. Lett.*, vol. 43, no. 3, pp. 495-498, Jan. 2018.
- [52] X. Ji, S. Roberts, M. Corato-Zanarella, and M. Lipson, "Methods to achieve ultra-high quality factor silicon nitride resonators," *APL Photonics*, vol. 6, no.7, p. 071101, Jul. 2021.
- [53] D. Z. Stupar *et al.*, "Remote monitoring of water salinity by using side-polished fiber-optic U-shaped sensor," *2012 15th International Power Electronics and Motion Control Conference (EPE/PEMC)*, pp. LS4c.4-1-LS4c.4-5, 2012.
- [54] P. E. Barclay, K. Srinivasan, and O. Painter, "Nonlinear response of silicon photonic crystal microresonators excited via an integrated waveguide and fiber taper," *Optics express*, vol. 13, no. 3, pp. 801-820, Feb. 2005.
- [55] Z. Yang, R. Zhang, Z. Wang, P. Xu, W. Zhang, Z. Kang, J. Zheng, S. Dai, R. Wang, and A. Majumdar, "High-Q, submicron-confined chalcogenide microring resonators," *Opt. Express*, vol. 29, no. 21, pp. 33225–33233, Oct. 2021.
- [56] G. Borselli, T. J. Johnson, and O. Painter, "Beyond the Rayleigh scattering limit in high-Q silicon microdisks: Theory and experiment," *Opt. Express*, vol. 13, no. 5, pp. 1515–1530, Mar. 2005.
- [57] E. A. Gondarenko, J. S. Levy, and M. Lipson, "High-confinement micron-scale silicon nitride high Q ring resonator," *Opt. Express*, vol. 17, no. 14, pp. 11366–11370, Jul. 2009.
- [58] K. Luke, Y. Okawachi, M. R. E. Lamont, A. L. Gaeta, and M. Lipson, "Broadband mid-infrared frequency comb generation in a Si<sub>3</sub>N<sub>4</sub> microresonator," *Opt. Lett.*, vol. 38, no. 22, pp. 4651–4654, Nov. 2013.
- [59] A. Lucianetti, J. Ertel, C. A. Baird, R. K. P. Bennington, D. A. Shay, and W. A. Clarkson, "Absorption of water at 1.3  $\mu\text{m}$  and 1.5  $\mu\text{m}$  and its effect on high power fiber lasers," *Opt. Express*, vol. 17, no. 2, pp. 662–671, Jan. 2009.
- [60] M. C. Shin, H. C. Park, K. S. Lee, and S. S. Lee, "Effect of surrounding refractive index on quality factor of optical microresonators," *Opt. Commun.*, vol. 281, no. 18, pp. 4644–4647, Sep. 2008.
- [61] F. Vollmer and L. Yang, "Label-free detection with high-Q microcavities: A review of biosensing mechanisms for integrated devices," *Nanophotonics*, vol. 1, no. 3–4, pp. 267–291, Dec. 2012.

- [62] X. Wu, T. Fan, A. A. Eftekhari, A. H. Hosseinnia, and A. Adibi, "High-Q ultrasensitive spiral-based coupled-resonator device on a Si<sub>3</sub>N<sub>4</sub> platform for sensing applications," in *Proc. Frontiers in Optics (FiO)*, Optical Society of America, 2020, p. FW4D.6.
- [63] H. Mirzajani, P. Zolfaghari, B. Y. Koca, and H. Urey, "Minimally invasive and in situ capacitive sensing of cardiac troponin I from interstitial fluid," *ACS Sens.*, vol. 1, no. 12, pp. 1403–1410, 2016.
- [64] M. Terracciano, I. Rea, J. Politi, and L. De Stefano, "Optical characterization of aminosilane-modified silicon dioxide surface for biosensing," *J. Eur. Opt. Soc. Rapid Publ.*, vol. 8, 2013.
- [65] K. De Vos, I. Bartolozzi, E. Schacht, P. Bienstman, and R. Baets, "Silicon-on-insulator microring resonator for sensitive and label-free biosensing," *Opt. Express*, vol. 15, no. 12, pp. 7610–7615, 2007.
- [66] N. S. K. Gunda, M. Singh, L. Norman, K. Kaur, and S. K. Mitra, "Optimization and characterization of biomolecule immobilization on silicon substrates using (3-aminopropyl) triethoxysilane (APTES) and glutaraldehyde linker," *Appl. Surf. Sci.*, vol. 305, pp. 522–530, 2014.
- [67] N. Majoul, S. Aouida, and B. Bessaïs, "Progress of porous silicon APTES-functionalization by FTIR investigations," *Appl. Surf. Sci.*, vol. 331, pp. 388–391, 2015.
- [68] M. Hiraoui, M. Guendouz, N. Lorrain, A. Moadhen, L. Haji, and M. Oueslati, "Spectroscopy studies of functionalized oxidized porous silicon surface for biosensing applications," *Mater. Chem. Phys.*, vol. 128, no. 1–2, pp. 151–156, 2011.
- [69] Y. Jiao and S. M. Weiss, "Design parameters and sensitivity analysis of polymer-cladded porous silicon waveguides for small molecule detection," *Biosens. Bioelectron.*, vol. 25, no. 6, pp. 1535–1538, 2010.
- [70] H. Ouyang, C. C. Striemer, and P. M. Fauchet, "Quantitative analysis of the sensitivity of porous silicon optical biosensors," *Appl. Phys. Lett.*, vol. 88, no. 16, p. 163108, 2006.
- [71] S.-H. Shen, I.-S. Wang, H. Cheng, and C.-T. Lin, "An enhancement of high-k/oxide stacked dielectric structure for silicon-based multi-nanowire biosensor in cardiac troponin I detection," *Sens. Actuators B Chem.*, vol. 218, pp. 303–309, 2015.
- [72] J. H. Chua, R.-E. Chee, A. Agarwal, S. M. Wong, and G.-J. Zhang, "Label-free electrical detection of cardiac biomarker with complementary metal-oxide semiconductor-compatible silicon nanowire sensor arrays," *Anal. Chem.*, vol. 81, no. 15, pp. 6266–6271, 2009.

- [73] G.-J. Zhang *et al.*, “Multiplexed detection of cardiac biomarkers in serum with nanowire arrays using readout ASIC,” *Biosens. Bioelectron.*, vol. 35, no. 1, pp. 218–223, 2012.
- [74] Z. Xia *et al.*, “Magnesiothermally formed porous silicon thin films on silicon-on-insulator optical microresonators for high-sensitivity detection,” *Adv. Opt. Mater.*, vol. 2, no. 3, pp. 235–239, 2014.
- [75] J. N. Anker, W. P. Hall, O. Lyandres, N. C. Shah, J. Zhao, and R. P. Van Duyne, “Biosensing with plasmonic nanosensors,” *Nature Materials*, vol. 7, no. 6, pp. 442–453, 2008.
- [76] F. Patolsky, G. Zheng, O. Hayden, M. Lakadamyali, X. Zhuang, and C. M. Lieber, “Electrical detection of single viruses,” *Proc. Natl. Acad. Sci. USA*, vol. 101, no. 39, pp. 14017–14022, 2004.
- [77] A. K. Naik, M. S. Hanay, W. K. Hiebert, X. L. Feng, and M. L. Roukes, “Towards single-molecule nanomechanical mass spectrometry,” *Nature Nanotechnology*, vol. 4, no. 7, pp. 445–450, 2009.
- [78] H. Lee, M.-G. Suh, T. Chen, J. Li, S. A. Diddams, and K. J. Vahala, “Spiral resonators for on-chip laser frequency stabilization,” *Nature Communications*, vol. 4, no. 2468, 2013.
- [79] H. Lee, T. Chen, J. Li, O. Painter, and K. J. Vahala, “Ultra-low-loss optical delay line on a silicon chip,” *Nature Communications*, vol. 3, no. 867, 2012.
- [80] Q. Li, A. A. Eftekhari, M. Sodagar, Z. Xia, A. H. Atabaki, and A. Adibi, “Vertical integration of high-Q silicon nitride microresonators into silicon-on-insulator platform,” *Optics Express*, vol. 21, no. 15, pp. 18236–18248, 2013.
- [81] Y. Chen, A. Ryou, M. R. Friedfeld, T. Fryett, J. Whitehead, B. M. Cossairt, and A. Majumdar, “Deterministic positioning of colloidal quantum dots on silicon nitride nanobeam cavities,” *Nano Letters*, vol. 18, no. 10, pp. 6404–6410, 2018.
- [82] A. Arbabi and L. L. Goddard, “Measurements of the refractive indices and thermo-optic coefficients of Si<sub>3</sub>N<sub>4</sub> and SiO<sub>x</sub> using microring resonances,” *Optics Letters*, vol. 38, no. 19, pp. 3878–3881, 2013.
- [83] A. H. Atabaki, E. S. Hosseini, A. A. Eftekhari, S. Yegnanarayanan, and A. Adibi, “Optimization of metallic microheaters for high-speed reconfigurable silicon photonics,” *Optics Express*, vol. 18, no. 17, pp. 18312–18323, 2010.
- [84] K. F. Palmer and D. Williams, “Optical properties of water in the near infrared,” *J. Opt. Soc. Am.*, vol. 64, no. 8, pp. 1107–1110, 1974.
- [85] F. Dell’Olio and V. M. N. Passaro, “Optical sensing by optimized silicon slot waveguides,” *Optics Express*, vol. 15, no. 8, pp. 4977–4993, 2007.

- [86] C. A. Barrios, M. J. Bañuls, V. González-Pedro, K. B. Gylfason, B. Sánchez, A. Griol, A. Maquieira, H. Sohlström, M. Holgado, and R. Casquel, “Label-free optical biosensing with slot-waveguides,” *Optics Letters*, vol. 33, no. 7, pp. 708–710, 2008.
- [87] T. Claes, J. G. Molera, K. De Vos, E. Schacht, R. Baets, and P. Bienstman, “Label-free biosensing with a slot-waveguide-based ring resonator in silicon-on-insulator,” *IEEE Photonics Journal*, vol. 1, no. 3, pp. 197–204, 2009.
- [88] H. Gu, H. Gong, C. Wang, X. Sun, X. Wang, Y. Yi, C. Chen, F. Wang, and D. Zhang, “Slot-ring resonator biochemical sensor on silicon,” *Sensors*, vol. 19, no. 22, p. 5038, 2019.
- [89] J. T. Robinson, L. Chen, and M. Lipson, “On-chip gas detection in silicon optical microcavities,” *Optics Express*, vol. 16, no. 6, pp. 4296–4301, 2008.
- [90] R. R. Singh, S. Kumari, A. Gautam, and V. Priye, “Photonic crystal cavity slot-ring sensors,” *IEEE J. Sel. Top. Quantum Electron.*, vol. 25, no. 2, pp. 7300608, 2019.
- [91] V. Mere, H. Muthuganesan, Y. Kar, C. V. Kruijsdijk, and S. K. Selvaraja, “Slot-ring resonators for refractive index sensing,” *IEEE Sensors Journal*, vol. 20, no. 11, pp. 5970–5978, 2020.
- [92] G. L. Knaack, D. G. McHail, G. Borda, B. Koo, N. Peixoto, S. F. Cogan, T. C. Dumas, and J. J. Pancrazio, “Neural interfaces using biocompatible materials,” *Frontiers in Neuroscience*, vol. 10, p. 301, 2016.
- [93] H. Morkoc, S. Strite, G. Gao, M. E. Lin, B. Sverdlov, and M. Burns, “Large-bandgap semiconductors,” *J. Appl. Phys.*, vol. 76, no. 3, pp. 1363–1398, 1994.
- [94] B.-S. Song, S. Yamada, T. Asano, and S. Noda, “Photonic crystal resonators with high-Q,” *Optics Express*, vol. 19, no. 11, pp. 11084–11089, 2011.
- [95] S. Yamada, B.-S. Song, J. Upham, T. Asano, Y. Tanaka, and S. Noda, “Photonic crystal nanocavities,” *Optics Express*, vol. 20, no. 14, pp. 14789–14798, 2012.
- [96] X. Wu, T. Fan, A. A. Eftekhari, and A. Adibi, “High-Q SiC slot-ring resonators,” *Optics Letters*, vol. 44, no. 19, pp. 4941–4944, 2019.
- [97] J. Jia, W. Sun, R. C. Hoogeveen, V. Nambi, K. Matsushita, A. R. Folsom, G. Heiss, D. J. Couper, S. D. Solomon, E. Boerwinkle, *et al.*, “High-sensitivity troponin I and incident coronary events, stroke, heart failure hospitalization, and mortality in the ARIC study,” *Circulation*, vol. 139, no. 23, pp. 2642–2653, 2019.
- [98] T. Keller, T. Zeller, D. Peetz, S. Tzikas, A. Roth, E. Czyz, C. Bickel, S. Baldus, A. Warnholtz, M. Fröhlich, *et al.*, “Sensitive troponin I assay in early diagnosis of acute myocardial infarction,” *N. Engl. J. Med.*, vol. 361, no. 9, pp. 868–877, 2009.

- [99] Z. Wang, Z. Hao, C. Yang, H. Wang, C. Huang, X. Zhao, and Y. Pan, “Ultra-sensitive and rapid screening of acute myocardial infarction using 3D-affinity graphene biosensor,” *Cell Rep. Phys. Sci.*, vol. 3, no. 5, p. 100855, 2022.
- [100] S. Singal, A. K. Srivastava, S. Dhakate, A. M. Biradar, and R. Rajesh, “Electroactive graphene-multi-walled carbon nanotube hybrid supported impedimetric immunosensor for the detection of human cardiac troponin-I,” *RSC Adv.*, vol. 5, no. 92, pp. 74994–75003, 2015.
- [101] S. E. Paramasivam, D. K. Challa, J. F. Njoroge, and R. E. Wysocki, “Nanophotonic biosensor for the detection of cardiac troponin I,” *ACS Omega*, vol. 3, no. 1, pp. 130–138, 2018.
- [102] C. K. Dixit, R. Kadimisetty, R. Rusling, and S. Shad, “Electrochemical detection of cardiac troponin I at picogram levels with a disposable immunosensor,” *Biosens. Bioelectron.*, vol. 77, pp. 845–852, 2016.
- [103] Y. Wu, J. Xu, H. Huang, and H. He, “Label-free detection of cardiac troponin I based on an optical fiber Mach–Zehnder interferometer,” *Opt. Lett.*, vol. 37, no. 21, pp. 4343–4345, 2012.
- [104] X. Liu, X. Li, Y. Xu, J. Shen, and Y. Deng, “A novel aptamer-based electrochemical biosensor for highly sensitive detection of cardiac troponin I,” *Biosens. Bioelectron.*, vol. 79, pp. 187–193, 2016.
- [105] J. L. Tang, Y. Wu, H. Zhao, and H. He, “An ultrasensitive cardiac troponin I biosensor based on surface plasmon resonance,” *Anal. Chem.*, vol. 83, no. 21, pp. 8608–8614, 2011.
- [106] H. Y. Xu, L. Zhang, Y. Wu, and H. He, “Porous silicon microcavity biosensor for detection of cardiac troponin I,” *Sens. Actuators B: Chem.*, vol. 160, no. 1, pp. 1070–1075, 2011.
- [107] F. Ghasemi *et al.*, “Multiplexed detection of lectins using integrated glycan-coated microring resonators,” *Biosens. Bioelectron.*, vol. 80, pp. 682–690, 2016.
- [108] A. L. Washburn, M. S. Luchansky, A. L. Bowman, and R. C. Bailey, “Quantitative, label-free detection of five protein biomarkers using multiplexed arrays of silicon photonic microring resonators,” *Anal. Chem.*, vol. 82, no. 1, pp. 69–72, 2010.
- [109] A. J. Qavi and R. C. Bailey, “Multiplexed detection and label-free quantitation of microRNAs using arrays of silicon photonic microring resonators,” *Angew. Chem. Int. Ed.*, vol. 49, no. 27, pp. 4608–4611, 2010.
- [110] O. Scheler *et al.*, “Label-free, multiplexed detection of bacterial tmRNA using silicon photonic microring resonators,” *Biosens. Bioelectron.*, vol. 36, no. 1, pp. 56–61, 2012.

- [111] A. J. Qavi, J. T. Kindt, M. A. Gleeson, and R. C. Bailey, “Anti-DNA:RNA antibodies and silicon photonic microring resonators: increased sensitivity for multiplexed microRNA detection,” *Anal. Chem.*, vol. 83, no. 15, pp. 5949–5956, 2011.
- [112] A. J. Qavi, T. M. Mysz, and R. C. Bailey, “Isothermal discrimination of single-nucleotide polymorphisms via real-time kinetic desorption and label-free detection of DNA using silicon photonic microring resonator arrays,” *Anal. Chem.*, vol. 83, no. 17, pp. 6827–6833, 2011.
- [113] F. Vollmer, S. Arnold, D. Braun, I. Teraoka, and A. Libchaber, “Multiplexed DNA quantification by spectroscopic shift of two microsphere cavities,” *Biophys. J.*, vol. 85, no. 3, pp. 1974–1979, 2003.
- [114] X. Sun, D. Dai, L. Thylén, and L. Wosinski, “Double-slot hybrid plasmonic ring resonator used for optical sensors and modulators,” *Photonics*, vol. 2, no. 4, pp. 1116–1130, 2015.
- [115] J. T. Kirk, G. E. Fridley, J. W. Chamberlain, E. D. Christensen, M. Hochberg, and D. M. Ratner, “Multiplexed inkjet functionalization of silicon photonic biosensors,” *Lab Chip*, vol. 11, no. 7, pp. 1372–1377, 2011.
- [116] J. T. Kindt and R. C. Bailey, “Biomolecular analysis with microring resonators: applications in multiplexed diagnostics and interaction screening,” *Curr. Opin. Chem. Biol.*, vol. 17, no. 5, pp. 818–826, 2013.
- [117] L. Zhou, X. Sun, X. Li, and J. Chen, “Miniature microring resonator sensor based on a hybrid plasmonic waveguide,” *Sensors*, vol. 11, no. 7, pp. 6856–6867, 2011.
- [118] K. De Vos, I. Bartolozzi, E. Schacht, P. Bienstman, and R. Baets, “Multiplexed antibody detection with an array of silicon-on-insulator microring resonators,” *IEEE Photon. J.*, vol. 1, no. 4, pp. 225–235, 2009.
- [119] D. Urbonas *et al.*, “Ultra-wide free spectral range, enhanced sensitivity, and removed mode splitting SOI optical ring resonator with dispersive metal nanodisks,” *Opt. Lett.*, vol. 40, no. 13, pp. 2977–2980, 2015.
- [120] Y.-F. Xiao, Y.-C. Liu, B.-B. Li, Y.-L. Chen, Y. Li, and Q. Gong, “Strongly enhanced light–matter interaction in a hybrid photonic–plasmonic resonator,” *Phys. Rev. A*, vol. 85, no. 3, p. 031805, 2012.
- [121] M. Chamanzar, M. Soltani, B. Momeni, S. Yegnanarayanan, and A. Adibi, “Hybrid photonic surface-plasmon-polariton ring resonators for sensing applications,” *Appl. Phys. B*, vol. 101, no. 1, pp. 263–271, 2010.
- [122] A. L. Washburn, W. W. Shia, K. A. Lenkeit, S.-H. Lee, and R. C. Bailey, “Multiplexed cancer biomarker detection using chip-integrated silicon photonic sensor arrays,” *Analyst*, vol. 141, no. 18, pp. 5358–5365, 2016.

- [123] Y.-F. Xiao, B.-B. Li, X. Jiang, X. Hu, Y. Li, and Q. Gong, “High quality factor, small mode volume, ring-type plasmonic microresonator on a silver chip,” *J. Phys. B: At. Mol. Opt. Phys.*, vol. 43, no. 3, p. 035402, 2010.
- [124] A. Bozzola, S. Perotto, and F. De Angelis, “Hybrid plasmonic–photonic whispering gallery mode resonators for sensing: a critical review,” *Analyst*, vol. 142, no. 6, pp. 883–898, 2017.
- [125] H. Zhang, B. Huang, Z. Zhang, Z. Zhang, L. Bao, and Y. Xie, “Highly sensitive optical biosensors based on silicon nitride sandwich-slot microring resonators for refractive-index sensing,” *J. Opt.*, vol. 27, no. 7, Art. no. 075301, Jul. 2025.
- [126] P. Müllner, R. Hainberger, J. Kraft, and W. Jantsch, “CMOS-compatible Si<sub>3</sub>N<sub>4</sub> waveguides for optical biosensing,” *Procedia Eng.*, vol. 120, pp. 578–581, 2015.
- [127] X. Tu, J. Song, T. Y. Liow, M. K. Park, J. Q. Yiying, and G. Q. Lo, “Thermal independent silicon-nitride slot waveguide,” *Opt. Express*, vol. 20, no. 3, pp. 2640–2655, Jan. 2012.
- [128] X. Tu, J. Song, T. Y. Liow, M. K. Park, J. Q. Yiying, and G. Q. Lo, “Thermal independent silicon-nitride slot waveguide,” *Opt. Express*, vol. 20, no. 3, pp. 2640–2655, Jan. 2012.
- [129] D. Köhler, S. T. Schwaiger, J. Haase, C. Karnutsch, and C. Koos, “Optical biosensors combining Si<sub>3</sub>N<sub>4</sub> sensor circuits with hybrid on-chip organic lasers,” *Light: Sci. Appl.*, vol. 10, no. 63, pp. 1–11, 2021.
- [130] M. S. Islam, S. S. A. Zubair, and M. R. Islam, “Design and bulk sensitivity analysis of a silicon nitride MZI integrated biosensor,” *J. Sens.*, vol. 2022, pp. 1–10, 2022.
- [131] A. la Grasta, M. Pisco, L. Zeni, and A. Cusano, “Integrated silicon nitride microphotonic platform for highly sensitive virus detection,” *Photoacoustics*, vol. 28, p. 100443, 2025.
- [132] A. Dhakal, A. Raza, S. Clemmen, P. Wuytens, K. Komorowska, and R. Baets, “Nanophotonic waveguide enhanced Raman spectroscopy of biological sub-monolayers,” *Opt. Lett.*, vol. 41, no. 20, pp. 4683–4686, Oct. 2016.
- [133] C. M. Naraine, D. Duchesne, M. A. Ettabib, M. I. F. Chishtie, and P. Horak, “Subwavelength grating metamaterial waveguides and ring resonators on a silicon nitride platform,” *J. Lightw. Technol.*, vol. 40, no. 23, pp. 7464–7472, Dec. 2022.
- [134] F. Dell’Olio and C. A. Barrios, “On-chip biosensing and gas sensing by photonic slot waveguides: a review,” *Nanophotonics*, vol. 13, no. 1, pp. 13–38, Jan. 2024.

- [135] X. Jiang, Y. Chen, F. Yu, L. Tang, M. Li, and J.-J. He, “High-sensitivity optical biosensor based on cascaded Mach-Zehnder interferometer and ring resonator using Vernier effect,” *Opt. Lett.*, vol. 39, no. 22, pp. 6363–6366, Nov. 15, 2014.
- [136] M. S. Murib, D. Martens, and P. Bienstman, “Label-free real-time optical monitoring of DNA hybridization using SiN Mach-Zehnder interferometer-based integrated biosensing platform,” *J. Biomed. Opt.*, vol. 23, no. 12, pp. 1–7, Dec. 2018.
- [137] K. Qin, S. Hu, S. T. Retterer, I. I. Kravchenko, and S. M. Weiss, “Slow light Mach-Zehnder interferometer as label-free biosensor with scalable sensitivity,” *Opt. Lett.*, vol. 41, no. 4, pp. 753–756, Feb. 15, 2016.
- [138] P. Kozma, F. Kehl, E. Ehrentreich-Förster, C. Stamm, and F. F. Bier, “Integrated planar optical waveguide interferometer biosensors: a comparative review,” *Biosens. Bioelectron.*, vol. 58, pp. 287–307, Aug. 15, 2014.
- [139] M. Kashif, A. A. Bakar, N. Arsad, and S. Shaari, “Development of phase detection schemes based on surface plasmon resonance using interferometry,” *Sensors (Basel)*, vol. 14, no. 9, pp. 15914–15938, Aug. 28, 2014.
- [140] C. Zhao, L. Xu, and L. Liu, “Ultrahigh sensitivity Mach-Zehnder interferometer sensor based on a weak one-dimensional field confinement silica waveguide,” *Sensors (Basel)*, vol. 21, no. 19, p. 6600, Oct. 2, 2021.
- [141] Y. Ma, B. Dong, and C. Lee, “Progress of infrared guided-wave nanophotonic sensors and devices,” *Nano Converg.*, vol. 7, no. 1, p. 12, Apr. 2, 2020.
- [142] V. Zamora, P. Lützow, M. Weiland, and D. Pergande, “A highly sensitive refractometric sensor based on cascaded SiN microring resonators,” *Sensors (Basel)*, vol. 13, no. 11, pp. 14601–14610, Oct. 28, 2013.
- [143] B. Troia, A. Z. Khokhar, M. Nedeljkovic, S. A. Reynolds, Y. Hu, and G. Z. Mashanovich, “Design procedure and fabrication of reproducible silicon Vernier devices for high-performance refractive index sensing,” *Sensors (Basel)*, vol. 15, no. 6, pp. 13548–13567, Jun. 10, 2015.
- [144] A. V. R. Portes, A. J. L. Martins, J. A. Guerrero, M. M. Carvalho, F. O. Amaya-Fernandez, L. A. M. Saito, and J. C. Ramirez, “Electro-optical biosensor based on embedded double-monolayer of graphene capacitor in polymer technology,” *Polymers (Basel)*, vol. 13, no. 20, p. 3564, Oct. 15, 2021.
- [145] R. S. El Shamy, M. A. Swillam, and X. Li, “Optimization of silicon nitride waveguide platform for on-chip virus detection,” *Sensors*, vol. 22, no. 3, Art. no. 1152, Feb. 2022.